

**Emerging Materials and Membrane-Based Processes for Recycling Hydraulic Fracturing  
Wastewater**

Md. Shahidul Islam

A Thesis

In the Department

of

Building, Civil and Environmental Engineering

Presented in Partial Fulfillment of the Requirements

For the Degree of

Doctor of Philosophy (Civil Engineering) at

Concordia University

Montreal, Quebec, Canada

January 2018

© Md. Shahidul Islam, 2018

**CONCORDIA UNIVERSITY**

School of Graduate Studies

This is to certify that the thesis prepared

By: Md. Shahidul Islam

Entitled: Emerging Materials and Membrane-Based Processes for Recycling Hydraulic Fracturing Wastewater

and submitted in partial fulfillment of the requirements for the degree of

Doctor of Philosophy (Civil Engineering)

complies with the regulations of the University and meets the accepted standards with respect to originality and quality.

Signed by the final examining committee:

\_\_\_\_\_ Chair  
Dr. Rabin Raut

\_\_\_\_\_ External Examiner  
Dr. Benoit Barbeau

\_\_\_\_\_ External to Program  
Dr. A. K. Waizuddin Ahmed

\_\_\_\_\_ Examiner  
Dr. Catherine Mulligan

\_\_\_\_\_ Examiner  
Dr. Amruthur S. Ramamurthy

\_\_\_\_\_ Supervisor  
Dr. Saifur Rahaman

Approved by,

\_\_\_\_\_ Dr. Fariborz Haghighat, Graduate Program Director

28 February 2018

Date of Defence

\_\_\_\_\_ Dr. Amir Asif, Dean, Faculty of Engineering & Computer Science

## ABSTRACT

### **Emerging Materials and Membrane-Based Processes for Recycling Hydraulic Fracturing Wastewater**

**Md. Shahidul Islam, Ph.D.**

**Concordia University, 2018**

The management of highly saline wastewater released from hydraulic fracturing—also known as fracking—a hydrocarbon releasing process used in the rapidly growing shale gas industry, is a serious challenge for industry and regulators due to its adverse effects on public health and to the environment in general. As well, fracking wastewater also contains particularly concerning levels of suspended solids, mainly comprised of sand and oil. Pre-treatment of fracking wastewater through microfiltration (MF) can effectively remove these suspended solids and oily materials. Forward osmosis (FO), an emerging membrane-based technology, is a feasible method for the treatment of fracking wastewater. For the FO process to be successful, an effectively engineered draw solution, a robust FO membrane, and an efficient pre-treatment, such as MF are required. FO is particularly effective when combined with membrane distillation (MD) for the recycling of the FO draw solutions. Therefore, the goals of this research project were to a) identify an effective draw solution for FO and b) fabricate two types of advanced membrane materials: MF membranes with high water flux, high rejection, and antifouling properties, and a FO membrane for recycling fracking wastewater with high water flux, high rejection, and antifouling properties. In this research, a comprehensive study was conducted to identify novel, yet effective, organic draw solutions for the treatment of fracking wastewater by FO. A novel high water-flux polyvinyl acetate-coated electrospun nylon 6/silica (SiO<sub>2</sub>) composite MF membrane was fabricated and its performance was tested in regard to water flux, oil rejection, and antifouling properties. In the next stage of this research, a new FO membrane material with high water-flux with high rejection and antifouling properties was fabricated and characterized. Finally, real fracking wastewater was treated using MF and then FO—combined with MD as a downstream separator—using the fabricated membranes. In the pre-treatment stage, ~98.5% turbidity and ~52% of total organic carbon (TOC) were removed

from the fracking wastewater via the MF process. Finally, treated water with TDS 23-44 mg/L was obtained from the pre-treated wastewater via the combined FO/MD process. This produced water can effectively be reused for hydraulic fracking.

## **DEDICATION**

I dedicate this research to my family members for their support during my hard time.

## **ACKNOWLEDGEMENTS**

I extend all of my sincere gratitude, and I would like to acknowledge the contributions of my supervisor, Dr. Saifur Rahaman. For his wise guidance throughout my research and the Ph.D. program, his financial support, and for giving me the opportunity to be a member of his research group and to work on such an interesting project, I wholeheartedly thank him.

I express my sincere appreciation to my committee members, Dr. Catherine Mulligan, Dr. Amruthur S. Ramamurthy and Dr. A. K. Waizuddin Ahmed for their time, their dedication, and their constructive criticism, providing me with the valuable advice needed to complete this project.

My gratitude and genuine thanks go out to all of the members in our research group. Finally, I express my deep thanks to those who made this work possible financially, Concordia University for support through the Graduate Fellowship and the Graduate Student Support Program (GSSP) and, the Natural Science and Engineering Research Council of Canada (NSERC) and the Fonds de recherche du Québec – Nature et technologies (FRQNT).

## Table of Contents

List of Figures .....	xiii
List of Tables.....	xix
List of Equations .....	xx
List of Abbreviations.....	xxii
Chapter 1: Introduction .....	1
Chapter 2: Literature Review, Thesis Motivation and Objective.....	5
2.1 Hydraulic fracturing and wastewater produced.....	5
2.2 Technologies for treatment of fracking wastewater .....	8
2.2.1 Mechanical vapor compression.....	8
2.2.2 Reverse osmosis.....	9
2.2.3. Membrane distillation .....	10
2.2.4 Forward osmosis .....	11
2.2.4.1 Membranes used in FO process .....	12
2.2.4.2 Draw solutions for FO process.....	13
2.2.4.3. Downstream separation in FO process.....	14
2.3 Problems with potential technology for desalination of fracking wastewater.....	14
2.4 Pre-treatment of fracking wastewater for the FO process .....	14
2.4.1 Technologies for pre-treatment of fracking wastewater .....	14
2.4.2 Problems with potential technology for the pre-treatment of fracking wastewater....	15
2.5 Thesis motivation .....	16
2.6 Thesis objective .....	17
Chapter 3: A High Flux Polyvinyl Acetate-coated Electrospun Nylon 6/SiO <sub>2</sub> Composite Microfiltration Membrane for the Separation of Oil-in-Water Emulsion with Improved Antifouling Performance.....	18

Abstract .....	18
Keywords .....	18
3.1 Introduction .....	19
3.2 Experimental.....	20
3.2.1 Materials .....	20
3.2.2 Preparation of solutions for electrospinning .....	20
3.2.3 Fabrication of MF membrane .....	21
3.2.3.1 Electrospinning.....	21
3.2.3.2 Coating, drying and washing.....	21
3.2.4 Fabrication of N6 and PVAc films .....	21
3.2.5 Physicochemical characterization .....	22
3.2.6 Porosity and pore size .....	23
3.2.7 Membrane performance evaluation .....	23
3.2.7.1 Hydraulic permeability measurement .....	23
3.2.7.2 Rejection test .....	24
3.2.7.3 Membrane antifouling test .....	24
3.2.7.4 Testing the stability of the membrane .....	25
3.3 Results and discussion .....	26
3.3.1 Membrane morphology.....	26
3.3.2 Structural study of the nylon 6/SiO <sub>2</sub> composite by XRD and FTIR analysis .....	33
3.3.3 Wettability and surface roughness of the membrane .....	34
3.3.4 Porosity, pore size, pore size distribution and tensile strength of the membranes .....	36
3.3.5 Permeation and rejection of the membrane .....	39
3.3.6 Antifouling propensity and stability of the membrane .....	42
3.4 Conclusions .....	45
Acknowledgements .....	46

Chapter 4: Forward Osmosis Treatment of Fracking Wastewaters: Evaluation of Suitable Organic Draw Solutions .....	47
Abstract .....	47
Keywords .....	47
4.1 Introduction .....	48
4.2 Selection of organic draw solutions.....	49
4.3 Experimental.....	50
4.3.1 Solution of the draw solutes.....	50
4.3.2 Membrane performance evaluation .....	51
4.3.3 FO experiment for the draw solutions .....	52
4.3.4 Investigation of thermolytic and thermally distillable properties of the draw solutes	53
4.3.5 Fracking wastewaters.....	54
4.3.6 Pre-treatment of the fracking wastewater .....	55
4.3.7 Desalination of fracking wastewater.....	56
4.4 Results and discussion .....	57
4.4.1 FO water flux and structural parameter of the membrane .....	57
4.4.2 Reverse salt flux and specific reverse salt flux of the draw solutions .....	58
4.4.3 Compatibility of the organic draw solutions with the commercial TFC membrane...60	
4.4.4 Studies into the recovery of the organic draw solutes downstream in the FO process .....	61
4.4.5 Characteristics of the fracking wastewater before and after pre-treatment .....	62
4.4.6 FO performance in desalination of fracking wastewaters.....	63
4.4.6.1 Water flux.....	63
4.4.6.2 Compositions of feed and draw solutions .....	66
4.5 Conclusions .....	68
Acknowledgements .....	68

Chapter 5: Silica Nanoparticle Containing Novel Thin-Film Composite Forward Osmosis Membrane with High Flux and Antifouling Properties.....	69
Abstract .....	69
Keywords .....	69
5.1 Introduction .....	70
5.2 Experimental.....	72
5.2.1 Materials .....	72
5.2.2 Fabrication of TFC membrane.....	72
5.2.2.1 Fabrication of N6/SiO <sub>2</sub> composite nanofiber substrate by electrospinning technique .....	72
5.2.2.2 Formation of PA/SiO <sub>2</sub> composite active layer on the substrate .....	73
5.2.3 Fabrication of N6 substrate by casting and phase inversion method.....	73
5.2.4 Physicochemical characterization .....	74
5.2.5 Porosity and pore size of the electrospun substrate .....	74
5.2.6 Performance evaluation of the TFC membrane .....	75
5.2.6.1 Water permeability, salt rejection, salt permeability and structural parameters ..	75
5.2.6.2 Water flux and reverse salt flux in FO experiment .....	75
5.2.6.3 Membrane antifouling test .....	76
5.3 Results and discussion .....	77
5.3.1 Morphology of the electrospun substrates .....	77
5.3.2 Structural study of the electrospun N6/SiO <sub>2</sub> composite by XRD and FTIR analysis.	79
5.3.3 Wettability and surface roughness of the electrospun substrates.....	80
5.3.4 Porosity, pore size and tensile strength of the electrospun substrates .....	81
5.3.5 Characteristics of casted N6 substrate .....	83
5.3.6 Morphology of the TFC membrane .....	83
5.3.7 Wettability and tensile strength of the membranes .....	87

5.3.8 Performance of the membranes .....	88
5.3.8.1 FO water flux and structural parameter of the membranes .....	88
5.3.8.2 Reverse salt flux and specific reverse salt flux of the membranes in FO process ...	91
5.3.8.3 Antifouling propensity of membrane in the FO process .....	92
5.4 Conclusions .....	94
Acknowledgements .....	94
Chapter 6: Performance of Combined MF-FO-MD Processes for Fracking Wastewater Treatment .....	95
Abstract .....	95
Keywords .....	95
6.1 Introduction .....	96
6.2 Materials and methods .....	97
6.2.1 Materials .....	97
6.2.2 Methods .....	98
6.2.2.1 Physicochemical characterization of membranes .....	98
6.2.2.2 Porosity and pore sizes of MF membranes .....	98
6.2.2.3 Pure water permeability of the membranes .....	98
6.2.2.4 Treatment of fracking wastewater .....	99
6.2.2.4.1 Pre-treatment of the fracking wastewater .....	99
6.2.2.4.2 Treatment of the pre-treated fracking wastewater by FO .....	100
6.2.2.4.3 Water flux recovery for the FO membranes fouled by fracking wastewater .....	100
6.2.2.4.4 Recycle of draw solutions in FO .....	101
6.3 Results and discussion .....	101
6.3.1 Characteristics of the membranes used for treatment of fracking wastewater .....	101
6.3.2 Pre-treatment of fracking wastewater by microfiltration .....	103
6.3.3 FO performance in desalination of fracking wastewater .....	108

6.3.3.1 Water flux and compositions of feed and draw solutions .....	108
6.3.3.2 Investigation of fouling behaviour for FO membranes .....	112
6.3.3.3 FO water flux recovery for pre-treated fracking wastewater as foulant .....	114
6.3.4 Recycling draw solution in the FO using MD .....	115
6.4. Conclusions .....	116
Acknowledgements .....	117
Chapter 7: Contributions, Conclusions and Recommendations for Future Work.....	118
7.1 Contributions .....	118
7.2 Conclusions .....	119
7.3 Recommendations for future work .....	121
References .....	123
Appendices .....	140
Appendix A .....	140
Appendix B.....	146
Appendix C.....	147
Appendix D.....	147

## List of Figures

Figure 1-1. A simple schematic of the hydraulic fracturing process [1].	1
Figure 1-2. A simple schematic representation of the forward osmosis process.	2
Figure 1-3. A simple schematic representation of the microfiltration process [3].	3
Figure 1-4. A conceptual schematic of proposed fracking wastewater treatment process.	4
Figure 2-1. Schematic of the hydraulic fracturing process [16].	6
Figure 2-2. Deep well underground injection of fracking wastewater [26].	8
Figure 2-3. A schematic representation of mechanical vapor compression process [30].	9
Figure 2-4. A schematic representation of the RO process [34].	10
Figure 2-5. Various configurations of membrane distillation process [41].	11
Figure 2-6. A schematic representation of experimental set up of FO process.	12
Figure 2-7. Dead-end and cross-flow operation modes of the microfiltration process [63].	15
Figure 2-8. A schematic representation of electrospinning technique.	17
Figure 3-1. FE-SEM images of electrospun nanofibers of (A) pristine N6, and N6/SiO <sub>2</sub> composites with SiO <sub>2</sub> contents of (B) 10, (C) 20 and (D) 30 wt.% . A mixture of 80% formic acid and 20% acetic acid by volume was used as solvent to prepare pristine N6 and N6/SiO <sub>2</sub> blended solutions for electrospinning. The surface of the electrospun nanofiber mats was coated with Pt to capture these FE-SEM images. The SEM-EDX spectra of the nanofibers were taken from the red spotted regions.	27
Figure 3-2. SEM-EDX spectra of nanofibers of (A) pristine N6 and (B, C, D) N6/SiO <sub>2</sub> composite.	28
Figure 3-3. TEM images of the nanofibers of (A) pristine N6; N6/SiO <sub>2</sub> composites with SiO <sub>2</sub> contents of (B) 10, (C) 20 and (D) 30 wt.%; and (E) FE-SEM image of the SiO <sub>2</sub> nanoparticles. The Cu grid and Si detector were used when capturing the TEM images of the electrospun nanofibers. The surface of the dispersed SiO <sub>2</sub> nanoparticles was coated with Pt to capture the FE-SEM images of the SiO <sub>2</sub> nanoparticles.	30
Figure 3-4. Surface FE-SEM images of the PVAc-coated electrospun membranes for (A) pristine N6 and (B) N6/SiO <sub>2</sub> (20 wt.%) composite, and (C) Cross-sectional FE-SEM image of PVAc-coated electrospun N6/SiO <sub>2</sub> (20 wt.%) composite membrane. The surface of the membranes was coated with Pt to capture these FE-SEM images. A 10 wt.% PVAc solution in	

acetone was used to fabricate the coating layer on the electrospun nanofiber mats through casting and then the phase inversion method. ....32

Figure 3-5. (A) XRD and (B) FTIR data for the nanofibers of pristine N6 and N6 with various SiO<sub>2</sub> contents (10, 20 and 30 wt.%). The X-ray source is copper and is equipped with a Vantec area detector. ....33

Figure 3-6. (A) The variation of water contact angle as a function of time for the PVAc-coated E.Spun N6/SiO<sub>2</sub> (20 wt.%) composite membrane, (B) The variation of water contact angle as a function of time for the commercial PSf membrane, AFM images of (C) E.Spun N6, (D) E.Spun N6/SiO<sub>2</sub> (20 wt.%) composite and (E) PVAc-coated E.Spun N6/SiO<sub>2</sub> (20 wt.%) composite. ....36

Figure 3-7. (A) Effect of SiO<sub>2</sub> nanoparticles and PVAc coating on the porosity of the electrospun N6 membrane, (B) Pore size of the PVAc-coated electrospun N6/SiO<sub>2</sub> composite membrane, (C) Pore size distribution of membranes, (D) Tensile strength of the fabricated and commercial PSf and PVDF membranes and (E) Schematic representation of the electrospun N6/SiO<sub>2</sub> composite. The porosity, average pore size and maximum pore size of each membrane were investigated via the gravimetric method, filtration velocity method and bubble point method, respectively.....38

Figure 3-8. Effect of applied pressure on the pure water flux for (A) the fabricated PVAc-coated electrospun N6/SiO<sub>2</sub> composite membrane with a mean pore size of 170 nm, (B) the commercial PSf membrane with a mean pore size of 200 nm and (C) the commercial PVDF membrane with a mean pore size of 220 nm, and on the rejection of oil by (D) the fabricated PVAc-coated electrospun N6/SiO<sub>2</sub> composite membrane, (E) the commercial PSf membrane and (F) the commercial PVDF membrane. A dead-end stirred cell filtration device connected to a nitrogen gas cylinder was used to investigate the pure water permeability and oil rejection at a stirring rate of 500 rpm and applied pressure, in bar, of 0.28 (4 psi), 0.55 (8 psi), 0.83 (12 psi), 1.1 (16 psi) and 1.38 (20 psi) at 25°C. ....40

Figure 3-9. Size distributions (A) and Stability (B) of oil droplets.....41

Figure 3-10. Permeability as a function of time for the (A) fabricated, (B) commercial PSf and (C) commercial PVDF membranes for O/W emulsion, (D) the water flux recovery for the fabricated and commercial PSf and PVDF membranes, and (E) permeability as a function of

time for DI, acidic and alkaline water and (F) the water contact angles of the PVAc-coated E.Spun N6/SiO<sub>2</sub> (20%) membrane before and after the permeation of DI, acidic and alkaline water. ....45

Figure 4-1. Flow chart for the selection of the organic draw solutes. ....50

Figure 4-2. (A) Reverse salt flux, (B) Structural formula of anion and (C) Specific reverse salt flux of the draw solutions. ....60

Figure 4-3. (A) Pure water permeability and (B) salt permeability of the membrane before and after FO experiment with each organic draw solution. ....61

Figure 4-4. Water flux as a function of time for (A) synthetic and (B) real fracking wastewaters, normalized water flux as a function of time for (C) synthetic and (D) real fracking wastewaters, and average water fluxes over 6 h for (E) synthetic and (F) real fracking wastewaters. [Fracking wastewaters as feed, and KAc, KF, NaGly, NaP and NaCl as draw solutions at an osmotic pressure of 18.48 MPa in FO process; Each set of experiments was conducted thrice and then the average values of obtained data from these three sets of experiments are presented in Figure 4-4]. ....65

Figure 5-1. FE-SEM images of electrospun substrates of (A) N6 and (B) N6/SiO<sub>2</sub> (20 wt.%) composite. A mixture of 80% formic acid and 20% acetic acid by volume was used as solvent to prepare pristine N6 and N6/SiO<sub>2</sub> blended solutions for electrospinning. The surface of the electrospun substrates was coated with Pt to capture these FE-SEM images. The SEM-EDX spectra of the electrospun substrates were taken from the yellow spotted regions. ....78

Figure 5-2. SEM-EDX spectra of electrospun substrates of (A) N6 and (B) N6/SiO<sub>2</sub> composites. (The SEM-EDX spectra of the electrospun substrates of pristine N6 and N6/SiO<sub>2</sub> composites were taken from the yellow spotted regions of Figure 5-1). ....78

Figure 5-3. TEM images of electrospun substrates of (A) N6 and (B) N6/SiO<sub>2</sub> composites. The Cu grid and Si detector were used when capturing the TEM images of the electrospun substrates. ....79

Figure 5-4. (A) XRD and (B) FTIR data for the electrospun N6 and N6/SiO<sub>2</sub> composite substrates. (The X-ray source is copper and equipped with a Vantec area detector). ....80

Figure 5-5. Wettability of the electrospun substrates of (A) N6 and (B) N6/SiO<sub>2</sub> composite. ....81

Figure 5-6. (A) FE-SEM image and (B) Water contact angle of casted N6 substrate. ....83

Figure 5-7. FE-SEM images of the top surface of electrospun N6/SiO<sub>2</sub> composite supported TFC membranes with PA/SiO<sub>2</sub> composite active layer with SiO<sub>2</sub> concentrations of (A) 0%, (B) 1%, (C) 2%, (D) 4% and (E) 6%, and (F) Cross-sectional FE-SEM images of the TFC membrane in the case of 4% SiO<sub>2</sub> nanoparticles incorporated in the PA active layer [The percentages of SiO<sub>2</sub> nanoparticles in the active layer were taken with respect to MPD during interfacial polymerization]. .....85

Figure 5-8. SEM-EDX spectra of electrospun N6/SiO<sub>2</sub> composite supported TFC membranes with (A) PA and (B) PA/SiO<sub>2</sub> composite active layers. (The SEM-EDX spectra of the TFC membranes were taken from the yellow spotted regions of Figure 5-7). .....86

Figure 5-9. AFM images of the TFC membranes of (A) electrospun N6/SiO<sub>2</sub>-PA and (B) electrospun N6/SiO<sub>2</sub>-PA/SiO<sub>2</sub> composites with 4% SiO<sub>2</sub> content in the PA active layer [The percentages of SiO<sub>2</sub> nanoparticles in the active layer were taken into account in regards to MPD during interfacial polymerization]. .....86

Figure 5-10. (A) Reverse salt flux and (B) Specific reverse salt flux of the membranes. Each set of FO experiments was conducted thrice and then the average values of obtained reverse salt flux and specific reverse salt flux from these three sets of experiments are presented in Figure 5-10. ....91

Figure 5-11. (A) Decline of water flux when 1 M NaCl was used as draw solution against DI water as feed, (B) Fouling behavior of the membrane when 1 M NaCl was used as draw solution against DI water with foulant, SA, as feed solution, (C) Decline of water flux after cleaning of the membrane fouled by SA (Draw solution: 1 M NaCl, Feed solution: DI water), (D) Fouling behavior of membrane when 1 M NaCl was used as draw solution against DI water with foulant, CaSO<sub>4</sub>, as feed solution and (E) Decline of water flux after cleaning of the membrane fouled by CaSO<sub>4</sub> (Draw solution: 1 M NaCl, Feed solution: DI water). [Each set of FO experiments was conducted thrice and then the average values of obtained reverse salt flux and specific reverse salt flux from these three sets of experiments are presented in Figure 5-11]. .....93

Figure 6-1. Pure water permeability for (A) nanocomposite and PSf MF membranes, and (B) permeability as a function of time for fracking wastewater using two different MF membranes (nanocomposite and polysulfone) and (C) magnification of blue spotted region of Fig. (B).

[Each set of experiments was conducted three times. The average values are presented in Figure 6-1 B and Figure 6-1 C]......104

Figure 6-2. The  $dt/dV$  versus  $V$  filtration curves for fouling stage of the (A) Nanocomposite, (B) PSf membranes in the microfiltration of fracking wastewater. [After data calculation, the  $dt/dV$  versus  $V$  filtration curve was plotted and fitted with the linear regression method. The specific cake resistance was determined from the equation  $dt/dV = 1/q + K/2 V$  [101,178] where  $dV$  is the permeate volume in the time of  $dt$  and  $q$  is a constant]. [Each set of experiments was conducted three times. The average values are presented in Figure 6-2]......105

Figure 6-3. (A) Specific cake resistance for the fouling stage and (B) Flux recovery for MF membranes in the microfiltration of fracking wastewater. ....106

Figure 6-4. Water flux as a function of time for raw (A, B) and pre-treated (C, D) fracking wastewaters using two different FO membranes (Nanocomposite and PA). [Each set of experiments was conducted three times and the average values obtained are reported in Figure 6-4]. .....109

Figure 6-5. FE-SEM images for (A) virgin membranes, and fouled membranes when (B) raw and (C) pre-treated fracking wastewaters were employed as feed while NaP was used as draw solution. ....112

Figure 6-6. SEM-EDX spectra of (A, B) virgin membranes, and fouled membranes when (C, D) raw and (E, F) pre-treated fracking wastewaters were employed as feed while NaP was used as draw solution. (The SEM-EDX spectra were taken from the red spotted regions of Figure 6-5)......114

Figure 6-7. (A) Decline of water flux for the pristine membrane when 4.6 M NaP is used as draw solution against pre-treated fracking wastewater, (B) Decline of water flux after cleaning the membrane fouled by the pre-treated fracking wastewater (Draw solution: 4.6 M NaP, Feed: Pre-treated fracking wastewater), and (C) Initial FO water flux recovery after cleaning of the membrane fouled by the pre-treated fracking wastewater. [Each set of experiments was conducted three times and the average values are reported in Figure 6-7 A and Figure 6-7 B]. .....115

Figure 6-8. Permeate flux, (B) Permeate quality and (C) Feed concentration as a function of time in MD process in which the pre-treated fracking wastewater was used as feed with

nanocomposite membrane. [Feed: Draw solutions NaCl (4.0 M) and NaP (4.6 M) obtained at the end of FO experiment used for pre-treated fracking wastewater using nanocomposite FO membrane; Feed temperature: 50 °C; Permeate temperature: 20 °C; Membrane effective area: 34 cm<sup>2</sup>]. [Each set of experiments was conducted three times with average values obtained reported in Figure 6-8]. .....116

## List of Tables

Table 2-1. Composition of fracking wastewater by ions and compounds, and their function in the hydraulic fracturing process [19, 22-25].	7
Table 2-2. Wastewater pre-treatment technologies with their functions [58].	15
Table 3-1. Water contact angles of nanoparticle and the various films/nanofiber mats/membranes.	35
Table 3-2. List of fabricated (for oil-water separation) and commercial MF membranes to compare their performance.	42
Table 4-1. Properties of the draw solutions at the temperature of 24°C.	51
Table 4-2. Composition of inorganic dissolved solids of the real fracking wastewater.	54
Table 4-3. FO water flux (at 2.8 MPa osmotic pressure of the draw solutions against DI water as feed) and structural parameter of the membrane.	58
Table 4-4. A list of the organic draw solutes as thermolytic and distillable at 50°C.	62
Table 4-5. Characteristics of fracking wastewaters.	63
Table 4-6. TDS and TOC in the feed and draw solutions at the beginning and end of the FO experiment.	67
Table 5-1. Porosity, pore size, and tensile strength of the electrospun substrates.	82
Table 5-2. Water contact angle and tensile strength of the TFC membranes.	88
Table 5-3. FO water flux (at 1 M NaCl draw solution against DI water as feed) and structural parameters of the membranes.	89
Table 5-4. Performance comparison of various FO TFC flat-sheet membranes in FO mode.	90
Table 6-1. Characteristics of the membranes in terms of thickness, porosity, mean pore size, water contact angle and water permeability.	102
Table 6-2. Characteristics of fracking wastewaters before and after pre-treatment by microfiltration.	107
Table 6-3. TDS and TOC in the feed and draw solutions at the beginning and end of the FO experiment.	111

## List of Equations

$\varepsilon_1(\%) = \frac{W_w - W_d}{\rho_w A_{m1} L_1} \times 100$	(3-1)	-----	23
$r_m = \sqrt{\left[ \frac{(2.9 - 1.75\varepsilon_1) \times 8\eta L_1 Q_T}{\varepsilon_1 A_{m1} \Delta P_1} \right]}$	(3-2)	-----	23
$R_{\max} = \frac{2\sigma \cos\theta}{P_b}$	(3-3)	-----	23
$J_0 = \frac{V}{A_{m1} \Delta t_1}$	(3-4)	-----	24
$A_1 = \frac{J_0}{\Delta P_1}$	(3-5)	-----	24
$R_o = \frac{C_{o,f} - C_{o,p}}{C_{o,f}} \times 100$	(3-6)	-----	24
$\frac{dt}{dV} = \frac{1}{q} + \frac{K}{2} V$	(3-7)	-----	25
$FR = \frac{J_x}{J_y} \times 100 (\%)$	(3-8)	-----	25
$J = \frac{\Delta V}{A_m \Delta t}$	(4-1)	-----	51
$A = \frac{J}{\Delta P}$	(4-2)	-----	51
$R (\%) = \frac{C_f - C_p}{C_f} \times 100$	(4-3)	-----	51
$B = \frac{A(1 - R)(\Delta P - \pi)}{R}$	(4-4)	-----	51
$S = \left( \frac{D}{J_w} \right) \ln \left[ \frac{A\pi_{\text{draw}} + B}{A\pi_{\text{feed}} + J_w + B} \right]$	(4-5)	-----	52
$J_s = \frac{C_{f,e} V_{f,e} - C_{f,i} V_{f,i}}{A_m \Delta t}$	(4-6)	-----	53
$\pi_{o,p} = \rho_w R_i T_m$	(4-7)	-----	53
$\pi_{o,p,f} = - \left( \frac{R_i T}{V_0} \right) \ln a_1$	(4-8)	-----	55

$a_1 = \frac{P}{P_0}$	(4-9) -----	55
$J_1 = \frac{V_1}{A_{m2}\Delta t_2}$	(6-1) -----	101
$R_1(\%) = \frac{C_{f1} - C_{p1}}{C_{f1}} \times 100$	(6-2) -----	101

## List of Abbreviations

FO	Forward Osmosis	XRD	X-ray Diffraction
MF	Microfiltration	FTIR	Fourier Transform Infra-Red
RO	Reverse Osmosis	AFM	Atomic Force Microscope
MD	Membrane Distillation	FR	Flux Recovery
CP	Concentration Polarization	RH	Relative Humidity
ICP	Internal Concentration Polarization	LMH	Litre.meter <sup>-2</sup> .hour <sup>-1</sup>
ECP	External Concentration Polarization	MPa	Mega Pascal
TFC	Thin-Film Composite	KAc	Potassium Acetate
PVAc	Polyvinyl Acetate	NH <sub>4</sub> Ac	Ammonium Acetate
TEOS	Tetraethyl Orthosilicate	NH <sub>4</sub> C	Ammonium Carbamate
SDS	Sodium Dodecyl Sulfate	KF	Potassium Formate
PVDF	Poly(vinylidene fluoride)	NaGly	Sodium Glycolate
PSf	Polysulfone	NaP	Sodium Propionate
N6	Nylon 6	NH <sub>4</sub> F	Ammonium formate
SiO <sub>2</sub>	Silica	TOC	Total Organic Carbon
DI	De-ionized	PA	Polyamide
FE-SEM	Field Emission-Scanning Electron Microscopy	E.Spun N6/SiO <sub>2</sub> - PA/SiO <sub>2</sub>	Electrospun N6/SiO <sub>2</sub> supported TFC FO membrane with PA/SiO <sub>2</sub> active layer
TEM	Transmission Electron Microscopy	E.Spun N6/SiO <sub>2</sub> - PA	Electrospun N6/SiO <sub>2</sub> supported TFC FO membrane with PA active layer
E.Spun Comm.	Electrospun Commercial	MPD TMC	m-phenylenediamine 1, 3, 5- Benzenetricarbonyl Trichloride
R <sub>a</sub>	Average surface roughness	TDS	Total Dissolved Solids

O/W	Oil-in-Water	EDX	Energy dispersive X-ray
SA	Sodium Alginate	CaSO <sub>4</sub>	Calcium sulfate
NSERC	Natural Science and Engineering Research Council of Canada	r <sub>m</sub>	Mean pore size
FRQNT	Fonds de recherche du Québec – Nature et technologies	R <sub>max</sub>	Maximum pore size
DLS	Particle size analyzer	A	Water permeability coefficient
K	Specific cake resistance	B	Salt permeability coefficient
S	Structural parameter	R	Solute rejection
DMF	N,N-dimethyl formamide	E.Spun N6-PA/SiO <sub>2</sub>	Electrospun N6 supported TFC FO membrane with PA/SiO <sub>2</sub> active layer
CTA	Cellulose Triacetate	E.Spun N6/PA	Electrospun N6 supported TFC FO membrane with PA active layer

## Chapter 1: Introduction

Shale gas is widely produced in many regions across the United States of America through a process called hydraulic fracturing (fracking). In this process, fractures in the underground rocks containing natural gas are created by pumping fluids to target underground rock layers at high pressures through a hole drilled from the surface. The fluids used for hydraulic fracturing generally consist of water, sand, and chemical additives that can open and extend naturally existing fractures in the underground rocks. The fractures can be extended through the rock for several hundred feet from the drilled hole. The pumped sand particles keep the fractures open so newly liberated natural gas comes out easily from the underground rocks. A simple schematic of the hydraulic fracturing process is exhibited in Figure 1-1.

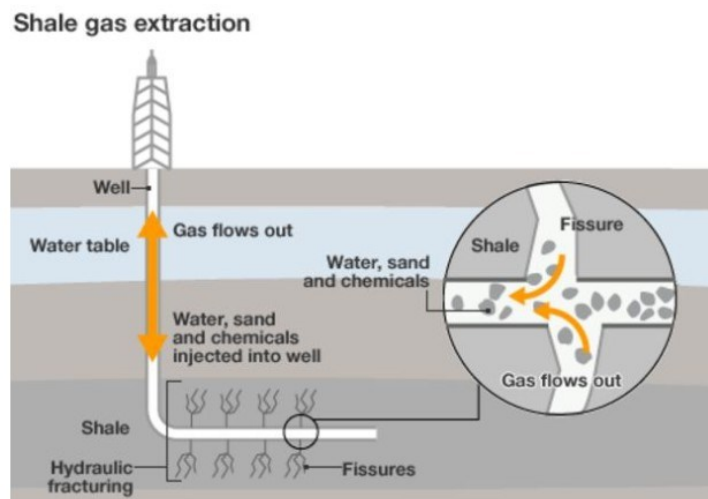


Figure 1-1. A simple schematic of the hydraulic fracturing process [1].

Because of the need for high pressure fluids to fracture rocks, large volumes of fracking fluid are employed during hydraulic fracturing, and therefore huge amounts of wastewater are discharged into the environment. Hydraulic fracturing fluid, called fracking wastewater, has significant adverse effects on both human health and the environment in general due to its high salinity. The effective management of fracking wastewater is a major concern for both the shale gas industry and industry regulators in order to balance the economics and the adverse effects of shale gas development. Recycling of fracking wastewater is therefore a potentially effective way to increase hydraulic fracturing viability.

Forward osmosis (FO) is an emerging technology that has been identified for the recycling of fracking wastewater through desalination. FO is a natural osmotic process in which

pure water flows from a feed/diluted solution to draw/concentrated solution through a semi-permeable membrane due to the difference in solute concentration—also known as osmotic pressure—between these two solutions. In fact, the semi-permeable membrane rejects salts and undesirable elements but allows water to flow through the membrane, and the draw solution creates a high osmotic pressure across the membrane, which is why water flows from the feed side to the draw side. A simple schematic representation of the forward osmosis process is exhibited in Figure 1-2.

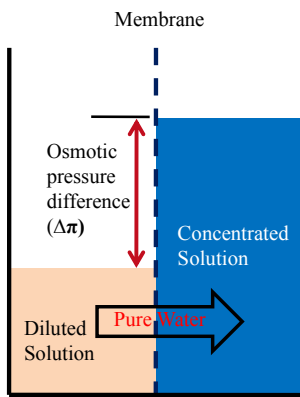


Figure 1-2. A simple schematic representation of the forward osmosis process.

Effective membranes and suitable draw solutions are two important aspects that need to be optimized to allow for the efficient treatment of fracking wastewater through forward osmosis process. Membranes currently in use are prone to fouling and as such demonstrate low water flux, and draw solutions in use don't show the necessary osmotic pressure, often leading to low osmotic pressures with high reverse salt flux. A membrane with high flux, high rejection and antifouling properties, and a draw solution offering high osmotic pressure yet low reverse salt flux are crucial to making the forward osmosis process successfully applicable in recycling fracking wastewater.

Moreover, the pre-treatment of fracking wastewater, before forward osmosis, is necessary to increase the efficiency and life expectancy of forward osmosis membranes by minimizing membrane fouling via preventative measures. The composition of fracking wastewater indicates that microfiltration should be an effective pre-treatment method for this type of wastewater. Microfiltration is a pressure dependent physical separation process in which insoluble solids, turbidity, and microorganisms can be removed from wastewaters based on the pore sizes (0.1 - 10  $\mu\text{m}$ ) of the membrane used in the process [2]. A simple schematic representation of the microfiltration process is shown in Figure 1-3.

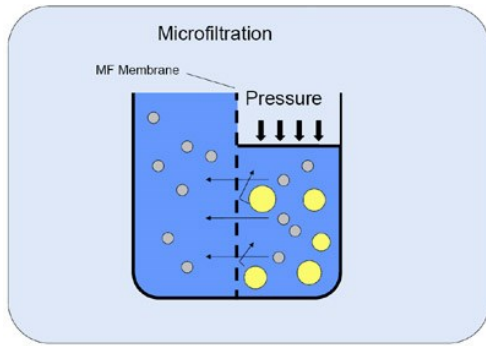


Figure 1-3. A simple schematic representation of the microfiltration process [3].

However, a general lack of suitable MF membranes is a major drawback for wider use of microfiltration as a pre-treatment step for fracking wastewater. Currently, the microfiltration membranes available provide low water permeability with a high propensity toward fouling. However, a highly permeable membrane with high rejection and antifouling properties is vital for microfiltration pre-treatment of fracking wastewater.

Therefore, the purpose of this research is to (1) fabricate a forward osmosis membrane with high flux with high rejection and antifouling, (2) identify suitable draw solutions with high osmotic pressure yet low reverse salt flux, and (3) fabricate a microfiltration membrane—showing high permeability, high rejection and antifouling propensity—for the pre-treatment of fracking wastewater to be recycled by forward osmosis and then membrane distillation processes.

Electrospinning is a process that can produce continuous polymer fibers—with diameters in the range of nanometers—through the application of an external electric field imposed on a spinneret containing the solutions of polymer or polymer/nanoparticles blend. Electrospun nanofiber mats possess some unique structural features such as a high surface-area-to-volume ratio, interconnected open pores and high porosity. These characteristics make them extremely suitable to fabricate membranes for water filtration applications. Therefore, the electrospinning technique can be used to fabricate suitable membranes for forward osmosis and microfiltration processes.

The complete process (conceptual) implemented for the treatment of fracking wastewater is shown in Figure 1-4. The initial, raw fracking wastewater contained dissolved organic compounds and inorganic salts with insoluble sand particles and oil. Microfiltration was used to remove both the sand particles and the oil from the wastewater. Afterward, forward osmosis and then membrane distillation processes were used to desalinate the fracking

wastewater. In fact, when put into practice, treated water with TDS 23-44 mg/L was obtained from fracking wastewater after the combined MF-FO-MD treatment.

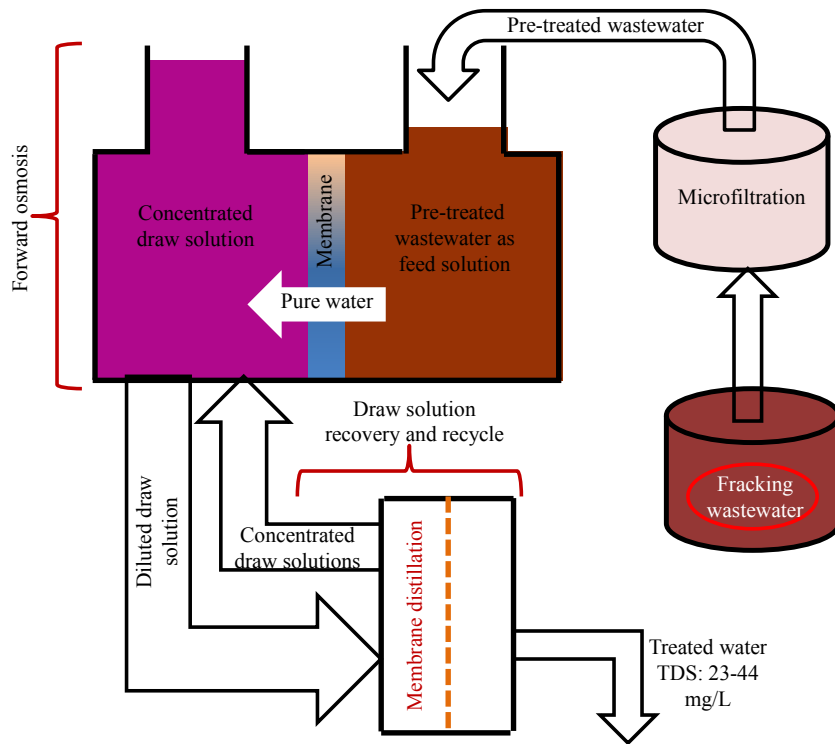


Figure 1-4. A conceptual schematic of proposed fracking wastewater treatment process.

This thesis consists of 7 chapters, the titles of which are provided below:

- Chapter 1: Introduction
- Chapter 2: Literature Review, Thesis Motivation and Objective
- Chapter 3: A High Flux Polyvinyl Acetate-coated Electrospun Nylon 6/SiO<sub>2</sub> Composite Microfiltration Membrane for the Separation of Oil-in-Water Emulsion with Improved Antifouling Performance
- Chapter 4: Forward Osmosis Treatment of Fracking Wastewaters: Evaluation of Suitable Organic Draw Solutions
- Chapter 5: Silica Nanoparticle Containing Novel Thin-Film Composite Forward Osmosis Membrane with High Flux and Antifouling Properties
- Chapter 6: Performance of Combined MF-FO-MD Processes for Fracking Wastewater Treatment
- Chapter 7: Contributions, Conclusions and Recommendations for Future Work

## **Chapter 2: Literature Review, Thesis Motivation and Objective**

### **2.1 Hydraulic fracturing and wastewater produced**

A substantial amount of natural gas can be held in porous pockets of underground rock. This phenomenon is described as “shale gas” [4]. In 2008, shale gas accounted for roughly 30 percent of the total national natural gas production of the United States [5]. This is a significant increase from only 4 percent of national production in 2005 [5]. Shale gas production has grown from less than 1 billion cubic feet per day in 2000 to almost 12 billion cubic feet in 2012, which accounts for U.S. to become a net exporter of natural gas. The total production of shale gas was expected to double further to over 24 billion cubic feet by 2015, and triple by 2030 [4, 6]. The U.S. Energy Information Administration (EIA) estimates that shale gas will comprise 50% of all national natural gas production by 2030 [7]. However, major shale gas production is not confined to the United States alone. With Australia, Canada, China, the European Union as a whole, India, Indonesia, and Russia all producing shale gas, the International Energy Agency [8] expects the production of natural gas to more than triple by 2035, and \$ 6.9 trillion USD will have been invested in production infrastructure by that point. The EIA estimates that there are 48 major shale gas basins around the world, located in 32 countries, with a reserve size similar to that of conventional natural gas reserves [9].

Drilling into shale rock and injecting fluid into the ground at high to crack the shale and release the natural gas held inside is referred to as “hydraulic fracturing” or “fracking” for short [8,10]. In this process, access to the shale is made via drilling, after which a sand/water suspension and proppants (chemicals) are pumped into the shale layer at high pressures. Consequently, natural gas is released and flows back to the surface with the drilling fluids [8, 11-12]. A schematic of the hydraulic fracturing process is shown in Figure 2-1. Hydraulic fracking has opened shale formations as viable natural gas zones [8,10]. Currently, shale gas is being produced in many regions of the United States [13], with Texas, Pennsylvania, Louisiana, and Arkansas leading production in 2014 [14]. It is expected that about 80 percent of all natural gas production sites developed over the next decade will employ hydraulic fracturing [15] to release the gas.

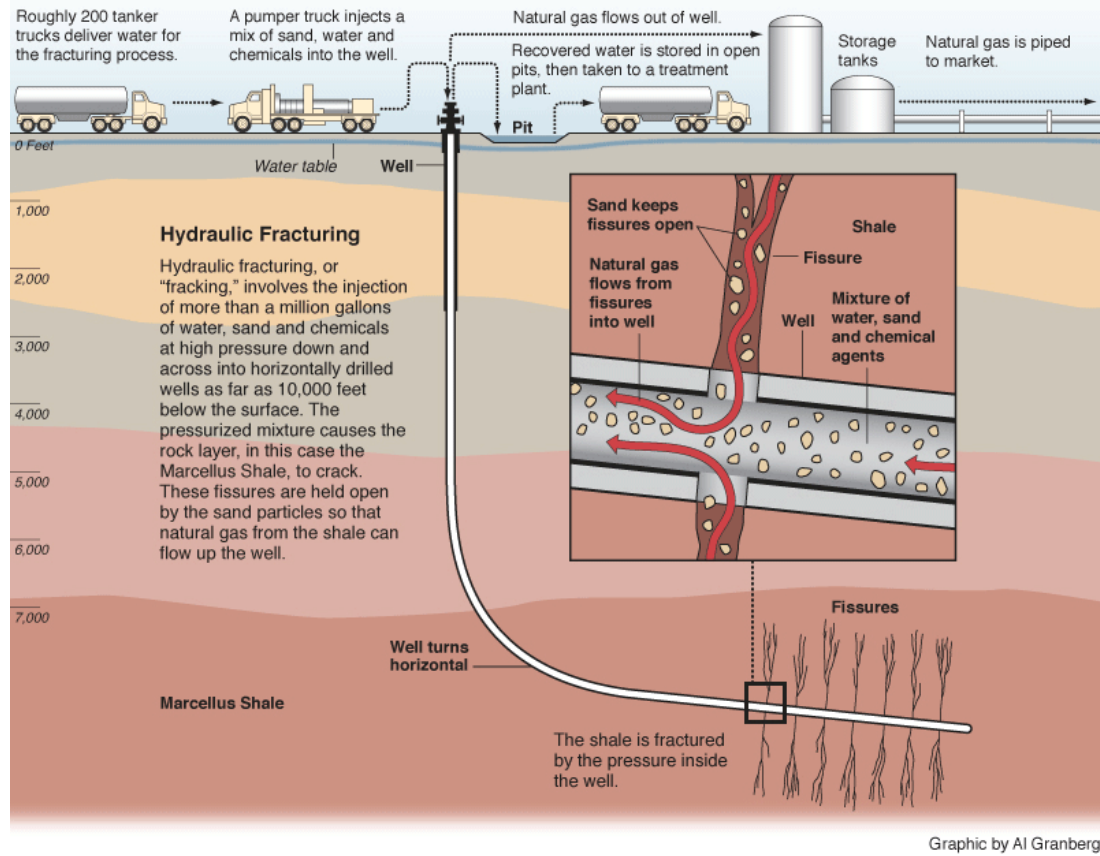


Figure 2-1. Schematic of the hydraulic fracturing process [16].

The production of shale gas through hydraulic fracturing has been widely criticized due to the potential entry of hydraulic fracturing fluids—called fracking wastewaters—into the environment during the fracturing process and the subsequent management of these wastewaters after industrial use [17]. It has been estimated that 2-4 million gallons of water are required for drilling and hydraulically fracturing a shale gas well [18]. Effective management of fracking wastewater is of major concern in order to balance the economics of shale gas development and the effects on both human health and the environment at large [19-20]. The main negative characteristic of shale gas wastewater is its high-salinity, due to the water coming into contact with different types of salts trapped in the shale as underground brines [21]. As well, fracking wastewater is enriched with isopropanol, ethylene glycol, N,N-Dimethyl formamide, glutaraldehyde, oil, and sand [22-25]. All of these organic compounds, along oil and sand are pumped into the shale layer during hydraulic fracturing. A complete list of the

ions and the compounds found in fracking wastewater, and their functions are listed in Table 2-1.

Table 2-1. Composition of fracking wastewater by ions and compounds, and their function in the hydraulic fracturing process [19, 22-25].

Component	Concentration (mg/L)	Function
Chloride (Cl <sup>-</sup> )	135590	-
Bromide (Br <sup>-</sup> )	1600	-
Sulfate (SO <sub>4</sub> <sup>2-</sup> )	501	-
Carbonate (CO <sub>3</sub> <sup>2-</sup> )	660	-
Sodium (Na <sup>+</sup> )	44000	-
Calcium (Ca <sup>2+</sup> )	31000	-
Magnesium (Mg <sup>2+</sup> )	2000	-
Strontium (Sr <sup>2+</sup> )	6800	-
Barium (Ba <sup>2+</sup> )	4700	-
Potassium (K <sup>+</sup> )	622	-
Manganese (Mn <sup>2+</sup> )	7	-
Iron (Fe <sup>3+</sup> )	55	-
Isopropanol	668	Surfactant
Ethylene glycol	473	Scale inhibitor
N,N-Dimethyl formamide	19	Corrosion inhibitor
Glutaraldehyde	11	Biocide
Sand	2500	To keep fissures open
Oil	700	Friction reducer
pH	4-10	-
Total dissolved solids	228706	-

Currently, the deep-well underground injection method (Figure 2-2) is used to manage fracking wastewater, however, this management system increases the risk of triggering an earthquake [26].

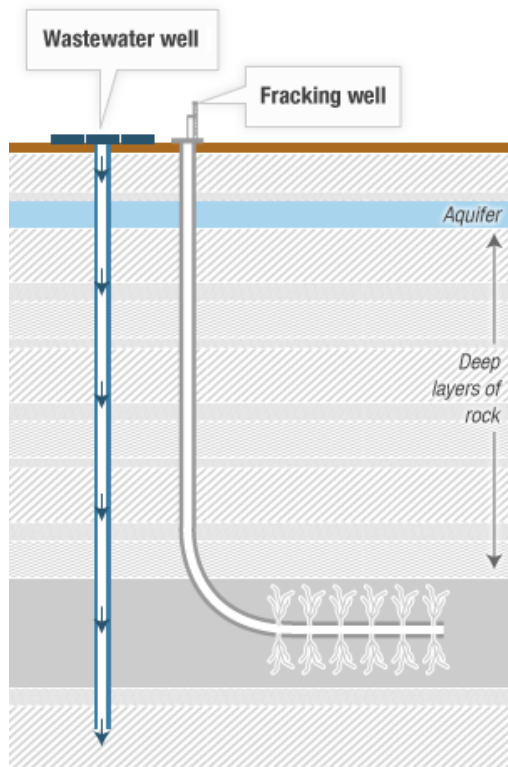


Figure 2-2. Deep well underground injection of fracking wastewater [26].

A possible solution to these noted environmental issues is the treatment of fracking wastewater before discharge/reuse. However, treatment of highly saline wastewater is challenging and energy intensive.

## 2.2 Technologies for treatment of fracking wastewater

Various technologies such as mechanical vapor compression, reverse osmosis, membrane distillation, and forward osmosis can be used for the desalination of fracking wastewater [24]. All of these processes are described in the following sections.

### 2.2.1 Mechanical vapor compression

Mechanical vapor compression uses electrical energy to drive separation. In this process, electricity is used to supply thermal energy for the desalination of saline water. This process consists of an open-loop heat pump, where a compressor driven by an electrical motor, supplies the energy required to evaporate water from a high-salinity feed [27]. A schematic representation of the mechanical vapor compression process is shown in Figure 2-3. Currently, mechanical vapor compression is used for the desalination of seawater and wastewater produced from heavy-oil fields [27-29].

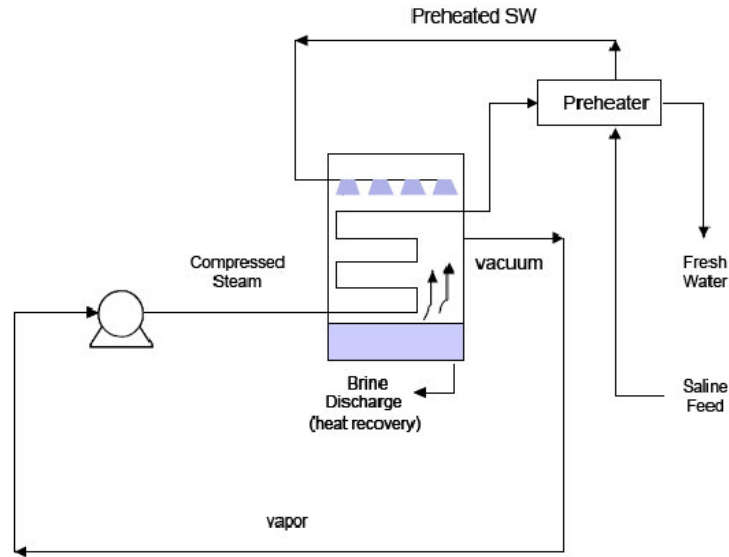


Figure 2-3. A schematic representation of mechanical vapor compression process [30].

Compared to the other production-water desalination technologies, the primary drawback of this process is its high energy requirements ( $10.4\text{--}13.6\text{ kW h/m}^3$  distillate) [27-28]. Also, the mechanical vapor compression process requires high-grade electrical energy to perform the separation process. Hence, an existing power grid or other continuous supply of electricity is required to apply this technology to the desalination of saline water [31-32].

### 2.2.2 Reverse osmosis

Reverse osmosis (RO) is a membrane-based pressure-driven process for the desalination of saline water [33]. To accomplish RO, applied pressure is required to force water molecules through the membrane, over coming the osmotic pressure that is driven by the concentration of the solution. A schematic representation of the RO process is exhibited in Figure 2-4.

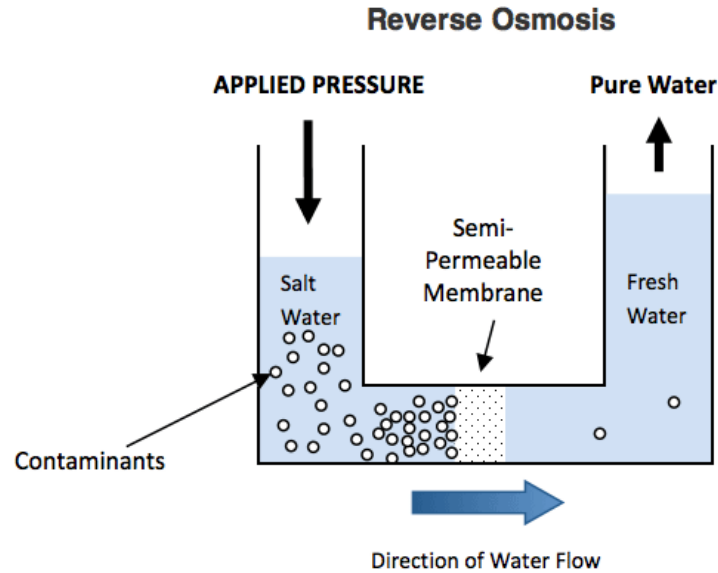


Figure 2-4. A schematic representation of the RO process [34].

RO is an energy-intensive process that requires a specific energy of about  $2 \text{ kWh/m}^3$  permeate for the desalination of seawater [35]. The salinity of fracking wastewater is higher than that of seawater. Therefore, the required specific energy for desalination of fracking wastewater will be higher than that needed for desalination of seawater. Also, a high propensity of membrane fouling is common in the pressure-driven RO process.

### 2.2.3. Membrane distillation

Membrane distillation (MD) (Figure 2-5) is an emerging technology that utilizes low-grade heat or industrial-waste heat at a temperature of approximately  $50^\circ\text{C}$  to drive separation [24]. MD is a thermally driven process where water vapor transport occurs through a non-wetted microporous hydrophobic membrane. The driving force behind the MD process is the vapor pressure gradient, which is generated by the temperature difference across the membrane. As the driving force involves vapour pressure and it is not purely thermal, membrane distillation can occur at a lower temperature than conventional thermal distillation. The hydrophobic nature of the membrane prevents penetration of the pores due to surface tension, unless a trans-membrane pressure higher than the membrane liquid entry pressure is applied. Therefore, liquid/vapor interfaces are formed at the entrance of each pore. Water transport through the membrane can be summarized in three steps: (1) the formation of vapor at the hot feed solution/membrane interface; (2) the transport of the vapor phase through the microporous

system; (3) the condensation of vapor at the “cold side” of the membrane/permeate solution interface [36-37]. However, the composition of fracking wastewater creates some unique challenges in the MD process [24]. During hydraulic fracturing, certain feed components, such as alcohols and surfactants, are added and these substances can lower the liquid surface tension of the feed solution and cause wetting of the pores of the membrane [38-40]. The feed solution can then flow directly through the wetted pores of the membrane, which can deteriorate permeate quality.

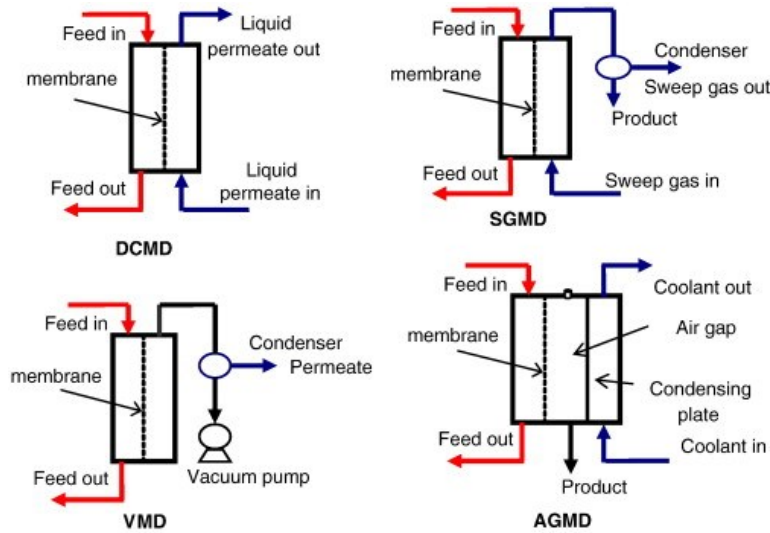


Figure 2-5. Various configurations of membrane distillation process [41].

#### 2.2.4 Forward osmosis

Forward osmosis is a natural osmotic process in which pure water flows from a diluted solution (feed solution) side to a concentrated solution (draw solution) side through a semi-permeable membrane due to differences in the concentration (or osmotic pressure) between these two solutions [42-43]. In fact, the semi-permeable membrane rejects salts and undesirable elements yet allows water to flow to the draw solution, creating a high osmotic pressure across the membrane, driving water to flow from feed to draw side. A schematic representation of an experimental setup of the FO process is shown in Figure 2-6.

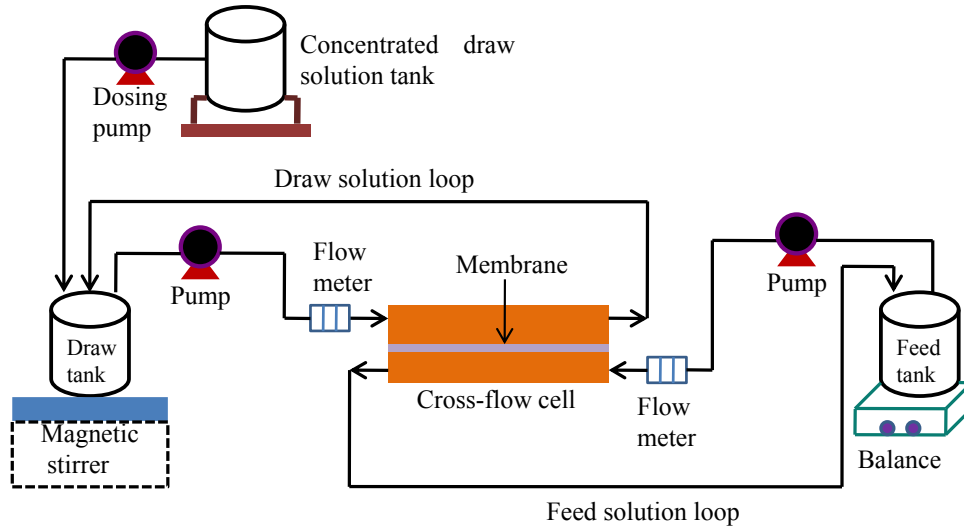


Figure 2-6. A schematic representation of experimental set up of FO process.

FO is an emerging technology for desalination. This process is advantageous as compared to other technologies for the desalination of highly saline feed waters as it requires fairly straightforward and inexpensive equipment that operates at low-pressures as water is transported through the membrane due to osmotic pressure rather than by applied hydraulic pressure [24]. The low-pressure required for the operation of the FO process also leads to a low propensity for irreversible fouling of the membrane [44-46].

#### 2.2.4.1 Membranes used in FO process

The first asymmetric cellulose acetate RO membranes developed in the 1960's [47] were initially intended for FO, however, due to inherent transport limitations were considered ineffective. Other RO membranes have also shown non-impressive results for FO due to hydrophobicity and relatively thick support layers [48]. Thick support layers often lead to poor performance of osmotically driven membrane processes, which can be mostly attributed to concentration polarization (CP).

Both internal CP (ICP) and external CP (ECP) exist. CP is caused by a balance between flux, rejection, and diffusion, and lowers both flux and membrane selectivity. ICP is exclusive to FO and occurs within the porous support layer of the membrane, while ECP is present at the surface of the dense active layer. The breakthrough necessary for the wider implementation of FO came with the development of thin, FO tailored cellulose triacetate membranes by HTI,

allowing higher fluxes through reduced ICP [49-50]. ICP, however, is still an issue for FO and is the main driver for further membrane development.

For wastewater treatment specifically, the propensity for FO membrane fouling needs to be addressed more vigilantly. The ideal FO membrane must also allow fast transport of water towards the draw side, with ideally no migration of solutes between the draw and feed solutions. Desirable FO membrane characteristics for use in wastewater applications demand (1) a dense, ultra-thin, active separating layer for high solute rejection; (2) an open, thin (as possible), hydrophilic support layer, with high mechanical stability, sustaining long-term operation and reducing ICP; and (3) a high affinity for water (hydrophilicity) for enhanced flux and reduced fouling propensity.

Different materials have been used for FO membranes [51]. The widely-used cellulose triacetate membrane is highly resistant to chlorine [52] and is unsusceptible to adsorption of mineral and fatty oils, including petroleum. Cellulose triacetate is also less sensitive to thermal, chemical and biological degradation [53], and hydrolysis at alkaline conditions than is cellulose acetate. However, permeability and fouling have been issues for cellulose triacetate membranes. New generation, commercial thin-film composite (TFC) membranes for FO are reportedly superior to cellulose triacetate membranes [51], in regards to permeability and stability at broader pH ranges. Still, permeability and fouling propensity are significant issues for commercial TFC membranes.

#### 2.2.4.2 Draw solutions for FO process

Choice of a draw solution plays a significant role in the FO process. An effective draw solution can contribute to obtaining high water flux. Commonly used draw solutions in osmotic processes are inorganic salts (calcium chloride, calcium nitrate, potassium bromide, potassium chloride, potassium bicarbonate, potassium sulfate, magnesium chloride, magnesium sulfate, sodium chloride, sodium bicarbonate, sodium sulfate, ammonium chloride, ammonium bicarbonate, ammonium sulfate) [54-56]. However, the reverse salt fluxes of inorganic draw solutions tend to skew high and as such it is likely to obtain low water flux in the FO process. In fact, reverse salt flux generates ICP and ECP which decreases water flux in the FO process. Therefore, efficient draw solutions are needed to make the FO process commercially viable.

#### 2.2.4.3. Downstream separation in FO process

To further increase commercial viability of FO, the draw solution needs to be reused. Currently, two types of separation processes—membrane distillation and thermal distillation—are being used to recycle draw solutions in FO [56-57]. The separation process is selected depending on the characteristics of the draw solution. Membrane distillation and thermal distillation were chosen as separation processes for distillable and thermolytic draw solutions, respectively [56-57].

#### 2.3 Problems with potential technology for desalination of fracking wastewater

FO is the most promising technology for the desalination of fracking wastewater as compared to other existing technologies such as mechanical vapor compression, reverse osmosis, and membrane distillation. However, effective membranes and draw solution are concerns for the application of this technology (FO) for desalination purposes.

#### 2.4 Pre-treatment of fracking wastewater for the FO process

The primary objective of pre-treatment is to make the feed water more compatible with the FO membrane. Pre-treatment is required to increase the efficiency and life expectancy of the membrane elements by minimizing fouling of the membrane. Fracking wastewater contains sand particles and oil, with dissolved organic compounds and inorganic salts [22-25]. Pre-treatment can remove sand particles and oil from fracking wastewater, making this wastewater suitable for desalination via FO.

##### 2.4.1 Technologies for pre-treatment of fracking wastewater

Wastewater can be pre-treated by using various technologies such as pre-screens, clarifier, media filtration, activated carbon, greensand filter, ozone, UV, coagulation, flocculation, sedimentation, ultrafiltration, or microfiltration. The functions of each technology are described in Table 2-2.

Table 2-2. Wastewater pre-treatment technologies with their functions [58].

Technology	Function
Pre-screens	Large objects and sand removal
Clarifier	Suspended solids reduction
Media filtration	Suspended solids removal
Activated carbon	Organic removal and dechlorination
Greensand filter	Iron / Manganese reduction
Ozone	Organic removal and reducing biological activities
UV	Reducing biological activities
Coagulation	Particulate, organic and biological activity removal
Flocculation	
Sedimentation	
Ultrafiltration	Particulate and bacteria removal and organic reduction
Microfiltration	

Ultrafiltration and microfiltration processes are commonly used for the separation of oil from water [59-62]. Depending on the insoluble contaminants in fracking wastewater (sands and oil), sedimentation and either ultrafiltration or microfiltration can be used as pre-treatment technologies. Sedimentation removes sand particles, while both ultrafiltration or microfiltration remove oil from the fracking wastewater. However, microfiltration is more convenient than ultrafiltration, which needs to higher pressures but provides lower permeability than microfiltration. The operating modes of the microfiltration process are exhibited in Figure 2-7.

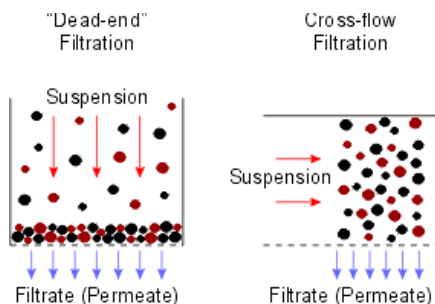


Figure 2-7. Dead-end and cross-flow operation modes of the microfiltration process [63].

#### 2.4.2 Problems with potential technology for the pre-treatment of fracking wastewater

As discussed in the earlier section, sedimentation and microfiltration are suitable technologies for pre-treatment of fracking wastewater. However, a lack of suitable membranes is a crucial issue for MF process. MF membranes currently in use provide low water permeability with a propensity toward fouling.

## 2.5 Thesis motivation

The amount of global fracking wastewater will be increasing daily due to the rising application of hydraulic fracturing. This increased amount of fracking wastewater will have a general effect of reducing the volume of fresh water reserves. The fracking wastewater produced should be reused/recycled in order to keep the reserve of fresh water constant and to protect the environment at large. As high salinity fracking wastewater cannot be reused/recycled directly, a feasible treatment method is necessary to make this wastewater suitable for reuse or recycle. Literature has demonstrated that the emerging forward osmosis process, coupled with microfiltration as a pre-treatment method is a viable strategy to treat the fracking wastewater [24, 59-62]. However, the viability of forward osmosis and microfiltration processes to treat wastewater depends on certain technological aspects, such as, choice/development of a suitable FO membrane, choice of effective draw solutions to be used in the FO process and choice/development of a suitable membrane for MF. Currently, existing literature lacks suitable membranes for FO and MF processes and effective draw solutions for FO process. Therefore, the fabrication of suitable membranes for these two processes and selection of effective draw solutions for FO are required to effectively treat fracking wastewater.

Electrospinning is a process that can produce continuous polymer fibers with diameters in the range of nanometers through the application of an external electric field imposed on a spinneret containing the polymer solution [64-65]. Electrospun nanofiber mats possess some unique structural features such as a high surface area-to-volume ratio, interconnected open pores and high porosity. These characteristics make them extremely suitable to fabricate membranes for water filtration applications [66-69]. Electrospun nanofiber mats obtained from hydrophilic polymers or hydrophilic polymers mixed with hydrophilic nanoparticles can be used to fabricate highly effective membranes for FO and MF processes. A schematic representation of the electrospinning technique is shown in Figure 2-8.

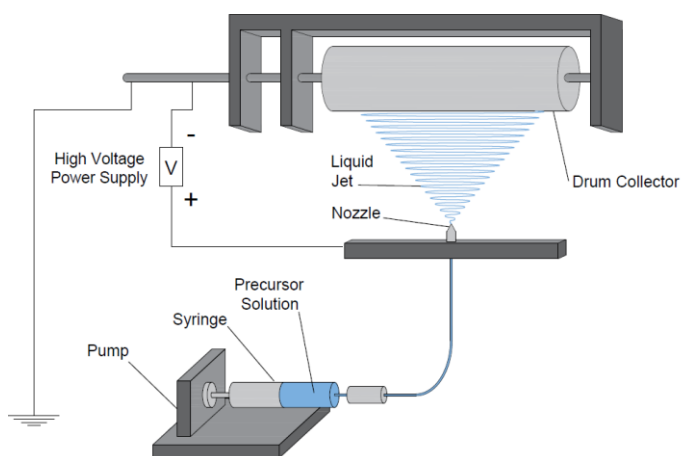


Figure 2-8. A schematic representation of electrospinning technique.

## 2.7 Thesis objective

The goal of the research is to treat fracking wastewaters by a combined MF/FO/MD process. In order to achieve the above goal, a polyvinyl acetate-coated electrospun nylon 6/SiO<sub>2</sub> composite MF membrane and a TFC FO membrane with polyamide/SiO<sub>2</sub> active layer supported by electrospun nylon 6/SiO<sub>2</sub> composite substrate have been fabricated. A comprehensive study has also been conducted to identify effective organic draw solutions to attain the above goal.

The fabricated membrane materials and efficient draw solutions with their functions are as follows:

- Highly hydrophilic polyvinyl acetate (PVAc)-coated electrospun nylon 6/SiO<sub>2</sub> composite MF membrane: To provide higher water flux and antifouling properties with the rejection of suspended solids and oil found in fracking wastewater.
- Highly hydrophilic electrospun nylon 6/SiO<sub>2</sub> composite supported TFC FO membrane with polyamide/SiO<sub>2</sub> composite as active layer: To provide higher water flux and antifouling properties in the FO process with the rejection of dissolved solids found in fracking wastewater.
- Effective organic draw solutions for the FO process: An essential requirement of the FO process is the draw solution. Effective organic draw solutions exhibit higher osmotic pressure with lower reverse salt flux. The higher osmotic pressure with a lower reverse salt flux of the draw solution contributes to higher water flux through the membrane.

### **Chapter 3: A High Flux Polyvinyl Acetate-coated Electrospun Nylon 6/SiO<sub>2</sub> Composite Microfiltration Membrane for the Separation of Oil-in-Water Emulsion with Improved Antifouling Performance**

[Islam et al., J. Membr. Sci. 537 (2017) 297-309]

#### **Abstract**

A high flux and antifouling PVAc-coated electrospun nylon 6 (N6)/SiO<sub>2</sub> composite MF membrane was prepared using a facile electrospinning technique. The fabricated MF membrane was robust (tensile strength of 23.3 MPa) with a porosity and average pore size of 78% and 170 nm, respectively. The PVAc-coated electrospun N6/SiO<sub>2</sub> composite membranes were used for the first time for microfiltration of oil-in-water (O/W) emulsions. This membrane achieved a water permeability of 4814 LMH/bar. During this microfiltration of O/W emulsions at 4 psi of applied pressure, the oil rejections of 98.80%, 99% and 99.20% were achieved from oil concentrations of 250 mg/L, 500 mg/L and 1000 mg/L, respectively. The fabricated membrane also showed antifouling properties with a water flux recovery of 85% with an O/W emulsion. Moreover, a strong interaction between the electrospun nanofiber mat and the PVAc coating demonstrated the structural stability of the membrane.

**Keywords:** Nylon 6/SiO<sub>2</sub> composite; Polyvinyl acetate; Microfiltration membrane; Electrospinning

### 3.1 Introduction

Everyday large quantities of oily wastewater are released from metallurgical, transportation, food processing, petrochemical, oil, gas and pharmaceutical industries [70]. This oily wastewater released can have significant negative impacts on the environment. Numerous technologies such as coagulation, flocculation, heating, ozonation, air flotation, ultrasonic separation and membrane filtration are used to treat oily wastewater [71-75]. MF membranes are receiving increased attention in the treatment of oily wastewater because the approach requires a low operating pressure yet has demonstrated excellent oil removal [76-77]. A facile technique called electrospinning is currently used in the fabrication of microfiltration membranes for a variety of application [78-80]. Electrospinning is a process that can produce continuous polymer fibers with diameters in the range of nanometers through the application of an external electric field imposed on a spinneret containing the polymer solution [64-65]. Electrospun nanofiber mats possess some unique structural features such as a high surface area-to-volume ratio, interconnected open pores and high porosity. These characteristics make them extremely suitable for filtration applications [66-69]. Nylon 6 is a synthetic polymer that has been applied to fabricate electrospun nanofiber mats [81-82]. Electrospun nylon 6 nanofiber mats are a suitable material for water filtration membranes because of their high mechanical strength, high resistance to abrasion and chemicals, extensive surface area, and high porosity [81-82]. The incorporation of SiO<sub>2</sub> nanoparticles into the polymer renders the composite (polymer/SiO<sub>2</sub>) hydrophilic due to the superhydrophilic property of SiO<sub>2</sub> nanoparticles [83]. In addition, the combination of the porous SiO<sub>2</sub> along with the integrated network structures renders a composite with higher porosity and mechanical strength [84-85]. PVAc is a thermoplastic polymer resistant to water, grease, oil and petroleum fuels [86]. These characteristics permit PVAc to be a valuable material for water filtration membranes [87].

Development of MF membranes with high water permeability and rejection (to oil), antifouling properties and desirable mechanical strength is crucial for their application in oil-water separation. The study presented here focuses on the preparation of a novel PVAc-coated nylon 6/SiO<sub>2</sub> composite MF membrane by utilizing the electrospinning technique and evaluating the separation performance in the treatment of synthetic oily wastewater emulsions. The electrospun N6/SiO<sub>2</sub> composite was highly hydrophilic and exhibited high mechanical strength due to the superhydrophilic property of SiO<sub>2</sub> nanoparticles and the interconnected spider-net

like structure of N6 nanofiber mats, respectively. The electrospun N6/SiO<sub>2</sub> composite was also highly porous. The high porosity and hydrophilicity of the electrospun N6/SiO<sub>2</sub> composite contributed to high water permeability as well as the low fouling potential of the membrane. PVAc was used as a coating material to decrease the surface roughness and average pore size of the electrospun nanofiber mats. In addition, the performance of the fabricated membrane was compared to the commercial MF membranes comprised of polysulfone and poly(vinylidene fluoride) (the commonly used commercial MF membrane in the treatment of oily wastewater [59,88-91]).

## 3.2 Experimental

### 3.2.1 Materials

Nylon 6, tetraethyl orthosilicate (TEOS), ethyl alcohol, polyvinyl acetate ( $M_w$  140,000), ammonium hydroxide, acetone and sodium dodecyl sulfate (SDS) were obtained from Sigma-Aldrich, USA. Both formic acid and acetic acid were received from Fisher Scientific, USA. The commercial MF membranes of poly(vinylidene fluoride) (PVDF) (Durapore<sup>R</sup>) (mean pore size 0.22  $\mu\text{m}$ ) and polysulfone (PSf) (HT) (mean pore size 0.20  $\mu\text{m}$ ) were purchased from Millipore, USA and Pall Corporation, USA, respectively. Machine oil (90% base oil with 10% additives, density of 881.4  $\text{kg}/\text{m}^3$  at 20 °C, kinematic viscosity of 271.62  $\text{mm}^2/\text{s}$  at 20 °C, and surface tension of 29.8  $\text{mN}/\text{m}$  at 20 °C) was received from Canadian Tire (Canada). De-ionized (DI) water was obtained from a Millipore Integral 10 water system (Millipore, Billerica, MA).

### 3.2.2 Preparation of solutions for electrospinning

N6 (21% by weight) was dissolved in a mixture of formic and acetic acids (80% formic acid and 20% acetic acid by volume) using magnetic stirring (rpm 350) for 5 h at room temperature. Separately, a SiO<sub>2</sub> solution was prepared by mixing TEOS, ethanol and water at a molar ratio of 1:2:2, respectively, in the presence of an ammonium hydroxide catalyst and stirred at 25°C for 4 h. The SiO<sub>2</sub> nanoparticles were then separated from the mixture through centrifugation. Subsequently, the SiO<sub>2</sub> nanoparticles were dispersed in a formic acid (80% by volume) and acetic acid (20% by volume) mixture under sonication for 20 min. An appropriate ratio of SiO<sub>2</sub> dispersion was then added into the N6 solution and sonicated for 5 min and then stirred for 5 h at ambient condition.

### 3.2.3 Fabrication of MF membrane

#### 3.2.3.1 Electrospinning

A schematic of electrospinning technique is shown in Figure 2-8, which is similar to other approaches in the literature [64, 92]. In this process, high-voltage electricity (Nanospinner NE300, Inovenso, Turkey) was applied to the prepared solutions in a syringe (volume 20 mL, inside diameter 19.05 mm) via an alligator clip attached to the syringe nozzle. The applied voltage was adjusted to 30 kV. The solution was delivered to the nozzle tip via a syringe pump to control the solution flow rate (0.18 mL/h). Fiber mats were collected on an electrically grounded metallic drum placed 8.8 cm above the nozzle tip [64, 92]. Temperature (25°C) and relative humidity (40%) were controlled throughout the fabrication process.

#### 3.2.3.2 Coating, drying and washing

A PVAc coating layer was applied onto the electrospun nanofiber mat through casting and then phase inversion techniques. PVAc was dissolved in acetone under magnetic stirring for 3 h to make a 10% casting solution. The N6 nanofiber mat was first soaked in DI water before coating in order to minimize the penetration of the PVAc solution into the nanofiber mat. After making the coating, the resulting two-tier composite membrane was dried for 4 h at ambient conditions and then immersed in de-ionized water for 24 h in order to remove the excess solvent from the membrane.

#### 3.2.4 Fabrication of N6 and PVAc films

Films of pristine N6 and PVAc were also prepared to investigate water contact angles. A 21% N6 solution (by weight) in 80% formic acid and 20% acetic acid mixture (by volume) was used to fabricate N6 film. The N6 solution was casted manually on a clean glass plate using a casting knife with the thickness of 60  $\mu\text{m}$  at ambient condition. After casting, the film was dried for 24 h at ambient condition and then it was removed from the glass plate. A 10% PVAc solution (by weight) in acetone was used to make PVAc film. The PVAc solution was casted manually on an aluminium foil putting on glass plate using a casting knife with the thickness of 60  $\mu\text{m}$  at ambient condition. The PVAc film was dried for 24 h at ambient condition after casting and then it was removed from the aluminium foil.

### 3.2.5 Physicochemical characterization

Field emission-scanning electron microscopy (FE-SEM) (QUANTA FEG 450) with a platinum coating on the sample surface, and transmission electron microscopy (TEM) (TF20) were performed to examine the morphology of the membrane. The cross-sectional morphology of the membrane was also investigated by FE-SEM. The pore size and the pore distributions of the membranes were investigated by image processing of FE-SEM's pictures using ImageJ software. Discrete pore diameters were determined by analyzing FE-SEM images of the membranes using ImageJ software. Three hundred pores were taken into consideration to investigate the pore size distributions of the membranes. A structural study of the membrane was conducted via the use of X-ray diffraction (XRD) (Bruker D8 Discover instrument in which the X-ray source is copper and is equipped with a Vantec area detector), and Fourier transform infra-red (FTIR) (NICOLET 6700 FT-IR) spectrometry. The wettability, surface roughness, and tensile strength of the membrane were investigated using a VCA optima instrument (AST Products, Inc.), an atomic force microscope (AFM) (BRUKER, NanoScope<sup>RV</sup>) and Instron (Mini 44), USA, respectively. The VCA optima instrument (AST Products, Inc.), was used to investigate the water contact angle of SiO<sub>2</sub> nanoparticles. The analysis was performed using the same protocol for SiO<sub>2</sub> nanoparticles described elsewhere [93]. Briefly, a few drops of suspension of SiO<sub>2</sub> nanoparticles in ethanol were placed on a glass slide first and then dried in an oven at 80°C for 30 min followed by cooling the SiO<sub>2</sub> nanoparticles on the glass slide at room temperature. Then the VCA optima instrument was used to determine the water contact angle of the SiO<sub>2</sub> nanoparticles placed on the glass slide. A particle size analyzer (DLS) (Malvern, Zetasizer Nano S90) was used to determine size distribution of oil droplets. The thicknesses of the membrane and film were measured using a TMI instrument (Testing Machines, Inc.). The oil concentrations were determined using a UV-spectrophotometer (PerkinElmer Instruments, Lambda 40 UV/VIS Spectrometer) at a wavelength of 256 nm [94]. The methodology and UV-calibration curve for the determination of oil content in O/W emulsions are provided in the appendix (Figure A-1, and Table A-1, Table A-2 and Table A-3, Appendix A).

### 3.2.6 Porosity and pore size

The gravimetric method was used to investigate the porosity of the membrane using the following equation [95-99]:

$$\varepsilon_1(\%) = \frac{W_w - W_d}{\rho_w A_{m1} L_1} \times 100 \quad (3-1)$$

where  $W_w$  and  $W_d$  are the weight of the wet and dry membranes, respectively;  $\rho_w$  is the water density ( $0.998 \text{ g cm}^{-3}$ );  $A_{m1}$  is the effective area of the membrane and  $L_1$  is the membrane thickness.

The mean pore size was determined via the filtration velocity method. The volume of permeate water was obtained using a dead-end stirred cell filtration device (Millipore stirred ultra-filtration cells, 8010, USA, effective area of  $0.0003 \text{ m}^2$ ) connected to a nitrogen gas cylinder. The mean pore size ( $r_m$ ) was calculated using the Guerout-Elford-Ferry equation [96-99]:

$$r_m = \sqrt{\left[ \frac{(2.9 - 1.75\varepsilon_1) \times 8\eta L_1 Q_T}{\varepsilon_1 A_{m1} \Delta P_1} \right]} \quad (3-2)$$

where  $\varepsilon_1$  is the membrane porosity;  $\eta$  is the water viscosity ( $8.9 \times 10^{-4} \text{ Pa s}$ );  $L_1$  is the membrane thickness;  $Q_T$  is the permeate volume per unit time;  $\Delta P_1$  is the applied pressure (1 bar) and  $A_{m1}$  is the effective area of the membrane.

The maximum pore size ( $R_{max}$ ) was determined via the bubble point method. The bubble point pressure was determined by using the aforementioned dead-end stirred cell filtration system. The membrane was immersed in DI water for 4 h and then fitted on the dead-end cell. The output tube of the dead-end cell was immersed in DI water so that the bubble point pressure could be read. The maximum pore size was calculated according to Laplace's equation [96]:

$$R_{max} = \frac{2\sigma \cos\theta}{P_b} \quad (3-3)$$

where  $\sigma$  is the surface tension of water ( $72.80 \times 10^{-3} \text{ Nm}^{-1}$ );  $\theta$  is the contact angle of water on the membrane and  $P_b$  is the minimum bubble point pressure.

### 3.2.7 Membrane performance evaluation

#### 3.2.7.1 Hydraulic permeability measurement

Pure water flux was measured using the aforementioned dead-end stirred cell filtration system. The membrane was pre-compacted at an applied pressure of 1.72 bar (25 psi) until a constant water flux was achieved. Water flux at a temperature of  $25 \text{ }^\circ\text{C}$  was measured at the applied

pressures of 0.28, 0.55, 0.83, 1.1 and 1.38 bar. The equations (3-4) and (3-5) were used to calculate the hydraulic (water) permeability for the membrane [95,100]:

$$J_0 = \frac{V}{A_{m1} \Delta t_1} \quad (3-4)$$

$$A_1 = \frac{J_0}{\Delta P_1} \quad (3-5)$$

where  $J_0$ ,  $V$ ,  $A_{m1}$ ,  $A_1$ ,  $\Delta t_1$  and  $\Delta P_1$  are the pure water flux/permeate flux, permeated water volume, membrane effective area, water permeability, measurement time, and applied pressure across the membrane, respectively.

### 3.2.7.2 Rejection test

The rejection of the composite membrane was tested with synthetic O/W emulsions. The aforementioned dead-end stirred cell filtration system was used to investigate the rejection. The membrane was pre-compacted at an applied pressure of 1.72 bar (25 psi) using DI water until a constant water flux was achieved. Afterwards, the emulsion was allowed to permeate through the membrane at a stirring rate of 500 rpm and various applied pressures (0.28, 0.55, 0.83, 1.1 and 1.38 bar) under nitrogen gas. The rejection was calculated using the following equation [95]:

$$R_o = \frac{C_{o,f} - C_{o,p}}{C_{o,f}} \times 100 \quad (3-6)$$

where  $R_o$  is the oil rejection and  $C_{o,f}$  and  $C_{o,p}$  are the concentrations of oil in the feed and permeate solutions, respectively. This experiment was conducted at a temperature of 25 °C.

The O/W emulsions (250 mg/L, 500 mg/L and 1000 mg/L) were made using a mixture of machine oil, surfactant (SDS) and DI water. The weight ratio of oil to surfactant was 4:1. In order to prepare a stable oil-in-water emulsion, the mixture of machine oil, SDS and DI water was subjected to ultrasonication for 5 min.

### 3.2.7.3 Membrane antifouling test

The dead-end stirred cell filtration system was used to evaluate the antifouling propensity of the membrane. In this experiment, the antifouling propensity was investigated by measuring the permeability as a function of time as well as the percentage of water flux recovery after fouling. Initially, the membrane was pre-compacted at an applied pressure of 0.55 bar (8 psi) under nitrogen gas using DI water until a constant water flux was achieved. A pure water flux was then measured at 0.28 bar (4 psi) of applied pressure using equation (3-4). Afterwards, the

O/W emulsion (1000 mg/L) was used as a feed solution to obtain the permeability at a stirring rate of 500 rpm and a 0.28 bar pressure. Water permeability was calculated at various time intervals for 2 h using equations (3-4) and (3-5) [95, 100]:

After data calculation, the  $dt/dV$  versus  $V$  filtration curve was plotted and fitted with the linear regression method. The specific cake resistance (K) was determined from the following equation [101].

$$\frac{dt}{dV} = \frac{1}{q} + \frac{K}{2} V \quad (3-7)$$

where  $dV$  is the permeate volume in the time of  $dt$  and  $q$  is a constant.

The membrane with a lower specific cake resistance shows a better antifouling performance during the filtration of wastewater.

After filtering the feed solutions, the membranes were cleaned by rinsing with DI water for 30 min, and the pure water flux was then measured again at the same pressure (0.28 bar). The water flux recovery (FR) was calculated according to the following equation [97, 99, 102-103]:

$$FR = \frac{J_x}{J_y} \times 100 (\%) \quad (3-8)$$

where  $J_y$  and  $J_x$  are the pure water flux of membrane before and after fouling, respectively.

#### 3.2.7.4 Testing the stability of the membrane

DI water, a 0.0001M HCl solution (pH 4) and a 0.0001 M NaOH solution (pH 10) were used to evaluate the membrane stability. The membrane stability was investigated by measuring the permeability as a function of time in this experiment. In order to perform the experiment, pure water, acidic water (pH 4) and alkaline water (pH 10) were forced to pass through the membrane using the aforementioned dead-end stirred cell filtration system. Initially, the membrane was pre-compacted at an applied pressure of 0.55 bar (8 psi) under nitrogen gas using DI water until a constant water flux was achieved. The experiment was conducted for 3 h at the applied pressure and temperature of 0.28 bar (4 psi) and 25 °C, respectively. The permeate flux was measured in 10 min time intervals. Equation (3-4) was used to calculate permeate flux for the membrane. In addition, the water contact angles of the membrane after the permeation of DI water, acidic water and alkaline water were measured to investigate the membrane stability.

### 3.3 Results and discussion

#### 3.3.1 Membrane morphology

The FE-SEM images of the pristine N6 and the N6/SiO<sub>2</sub> composite electrospun nanofibers with different SiO<sub>2</sub> contents (10, 20 and 30%) are exhibited in Figure 3-1. Figure 3-1 A shows the nanofibers of the pristine N6 which have a fiber diameter range of 80-160 nm. The relative humidity (RH) showed a significant effect on fiber morphology [104], which has been discussed in the appendix (Figure A-2, Appendix A). A RH of 40% was determined to be the optimum condition for the N6 solution to produce the best electrospun nanofibers (Figure 3-1 A). The higher applied voltage (30 kV) during the electrospinning caused N6 to ionize in the acid solvent which resulted in the formation of spider-net like structure of nanofibers shown in Figure 3-1 A [82, 105]. The diameters of the fibers increased gradually with increasing content of SiO<sub>2</sub> nanoparticles (Figure 3-1 B, Figure 3-1 C and Figure 3-1 D). The addition of highly surface-active SiO<sub>2</sub> nanoparticles can increase both the viscosity and surface tension of electrospinning solutions, which contribute to increase the diameters of composite nanofibers [106]. Furthermore, the density of the spider-net like structure of nanofibers was decreased with the incorporation of SiO<sub>2</sub> nanoparticles. The addition of SiO<sub>2</sub> nanoparticles may decrease the conductivity of the ionic N6 solution which in turn decreases the ionization of the N6 during the electrospinning process. Hence, the density of the spider-net like structure of nanofibers was decreased due to decrease in the conductivity of the ionic N6 [82]. Moreover, aggregated SiO<sub>2</sub> nanoparticles were observed in the nanofibers of the 30 wt.% SiO<sub>2</sub> content (Figure 3-1 D), however no aggregation is noted for lower SiO<sub>2</sub> concentrations (Figure 3-1 B and Figure 3-1 C). For this reason, 20 wt.% SiO<sub>2</sub> content was the optimum dose for N6/SiO<sub>2</sub> composite nanofibers.

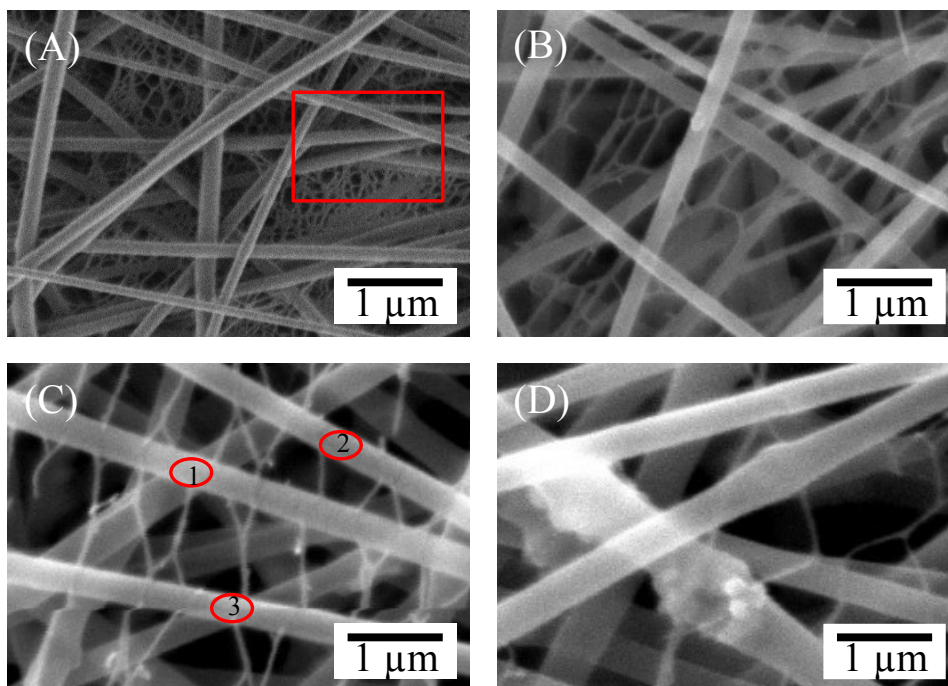


Figure 3-1. FE-SEM images of electrospun nanofibers of (A) pristine N6, and N6/SiO<sub>2</sub> composites with SiO<sub>2</sub> contents of (B) 10, (C) 20 and (D) 30 wt.% . A mixture of 80% formic acid and 20% acetic acid by volume was used as solvent to prepare pristine N6 and N6/SiO<sub>2</sub> blended solutions for electrospinning. The surface of the electrospun nanofiber mats was coated with Pt to capture these FE-SEM images. The SEM-EDX spectra of the nanofibers were taken from the red spotted regions.

The SEM-EDX spectra of the nanofibers for the pristine N6 and N6/SiO<sub>2</sub> composites are exhibited in Figure 3-2. The EDX analysis suggests the presence of C, N and O atoms of N6 (Figure 3-2 A). Pt was also obtained in the EDX spectrum due to the Pt coating applied to conduct the SEM analysis for the nylon 6 nanofibers. The N6/SiO<sub>2</sub> composite showed a new peak for Si and an O peak with a higher intensity than previously observed for N6 alone (Figure 3-2 B, Figure 3-2 C and Figure 3-2 D). In order to assure good dispersion of incorporated SiO<sub>2</sub> nanoparticles in the N6 nanofiber, SEM-EDX spectra were taken from more than one point for the same SiO<sub>2</sub> content. This result confirmed the successful incorporation of SiO<sub>2</sub> nanoparticles into the N6 nanofibers.

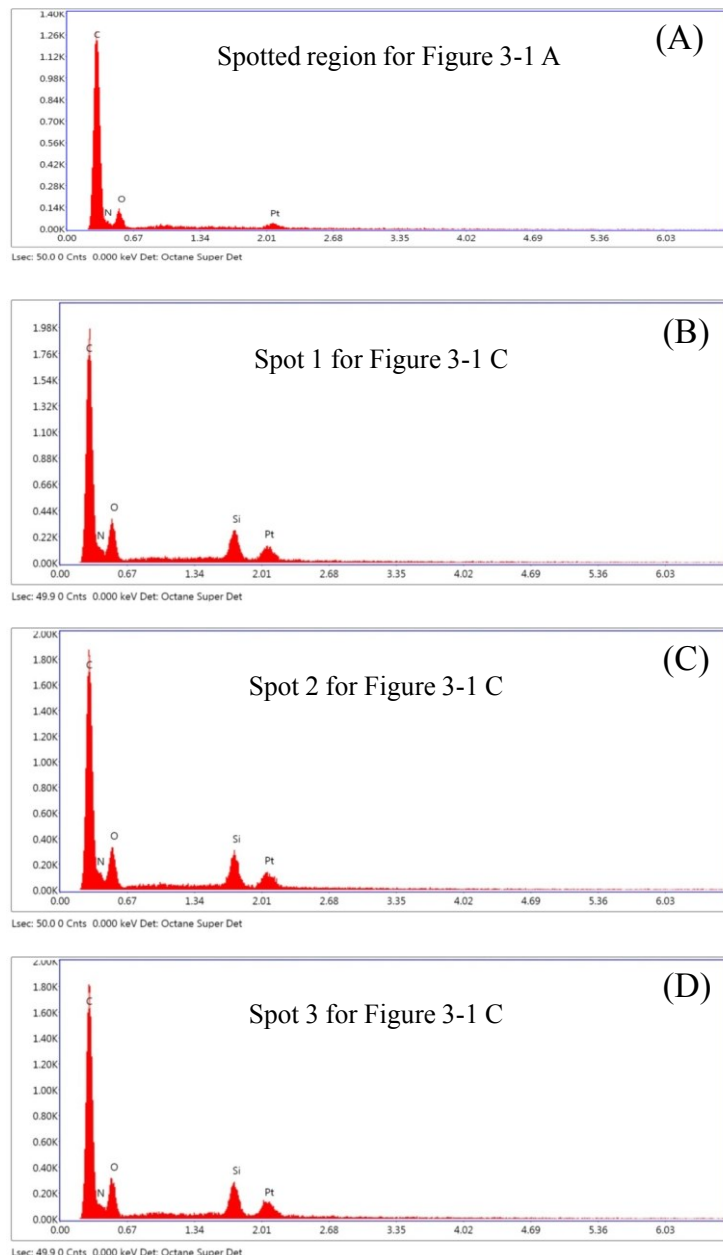


Figure 3-2. SEM-EDX spectra of nanofibers of (A) pristine N6 and (B, C, D) N6/SiO<sub>2</sub> composite.

Figure 3-3 exhibits the TEM images of the nanofibers of the pristine N6 and N6/SiO<sub>2</sub> composites as well as an FE-SEM image of the SiO<sub>2</sub> nanoparticles. The SiO<sub>2</sub> nanoparticles were incorporated and well-distributed in the N6 nanofibers for the samples containing 10 wt.% and 20 wt.% SiO<sub>2</sub> content (Figure 3-3 B and Figure 3-3 C). However, the sample with 30 wt.% SiO<sub>2</sub> content displayed the aggregation of the SiO<sub>2</sub> nanoparticles in the nanofibers (Figure 3-3

D). Hence, the N6/SiO<sub>2</sub> composite nanofibers were fabricated with 20 wt.% SiO<sub>2</sub> content because it maximized SiO<sub>2</sub> content without any noticed particle aggregation. The TEM images also show the size of the nanoparticles (about 30 nm), which is also exhibited by FE-SEM images (Figure 3-3 E). In the FE-SEM image (Figure 3-3 E), the nanoparticles were aggregated, however, the size of a single nanoparticle was clearly demonstrated in their composite (Figure 3-3 B and Figure 3-3 C).

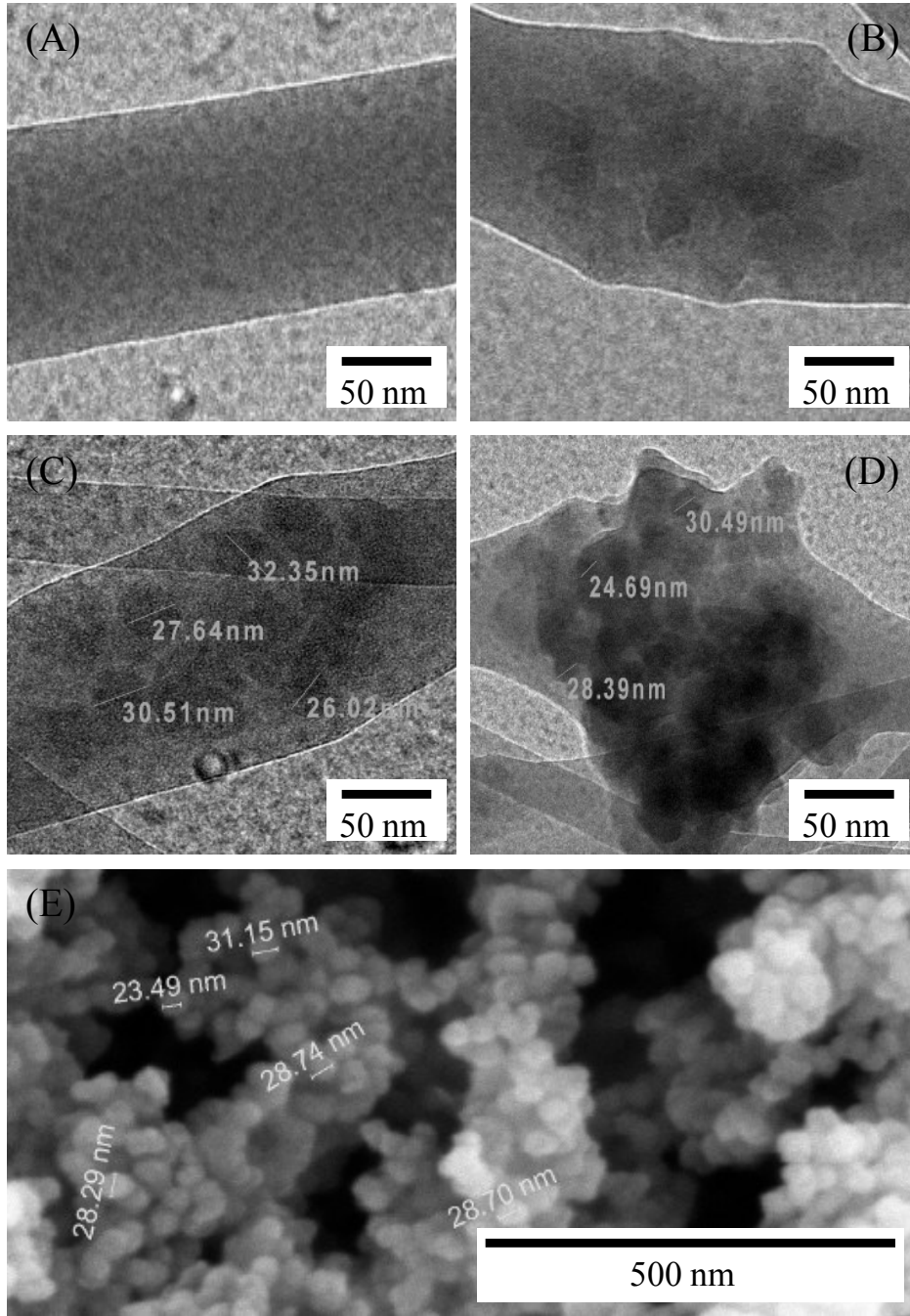


Figure 3-3. TEM images of the nanofibers of (A) pristine N6; N6/SiO<sub>2</sub> composites with SiO<sub>2</sub> contents of (B) 10, (C) 20 and (D) 30 wt.%; and (E) FE-SEM image of the SiO<sub>2</sub> nanoparticles. The Cu grid and Si detector were used when capturing the TEM images of the electrospun nanofibers. The surface of the dispersed SiO<sub>2</sub> nanoparticles was coated with Pt to capture the FE-SEM images of the SiO<sub>2</sub> nanoparticles.

The surface morphology of the PVAc-coated electrospun N6 and N6/SiO<sub>2</sub> composite membranes are displayed in Figure 3-4. The pore sizes of both membranes were about 100-300 nm. However, the porosity of PVAc-coated electrospun N6/SiO<sub>2</sub> composite membrane was higher (Figure 3-4 B) than the pristine N6 membrane (Figure 3-4 A). The PVAc coating was fabricated on the electrospun nanofiber mats through casting, then phase inversion. A highly volatile solvent (acetone) was used to prepare the PVAc casting solution. The membrane was dried for 4 h after casting the PVAc solution on the electrospun nanofiber mats. Membrane pores were created during the drying process, due to high volatility of the solvent; however, it was possible for much of the solvent to remain inside the coating. In order to remove any remaining solvent, the membranes were immersed in de-ionized water for 24 h and many of the membrane pores were created during this period [107]. In fact, the N6/SiO<sub>2</sub> nanofiber mat resulted in a PVAc-coated membrane with a higher porosity than that of the PVAc-coated N6 membrane because the composite was highly hydrophilic and therefore strongly facilitated the diffusion of water from the coagulation bath to the membrane when the membrane was immersed in de-ionized water in order to remove the excess solvent from it. The cross-section of the fabricated PVAc-coated electrospun N6/SiO<sub>2</sub> (20 wt.%) composite membrane is shown in Figure 3-4 C. The thicknesses of the fabricated membranes were ~ 155 μm including the coating layer which had a thickness of ~ 7 μm. The coating layer was strongly attached on the surface of electrospun nanofiber mat due to the interaction between the polar amide groups of N6 and the polar ester groups of PVAc [86].

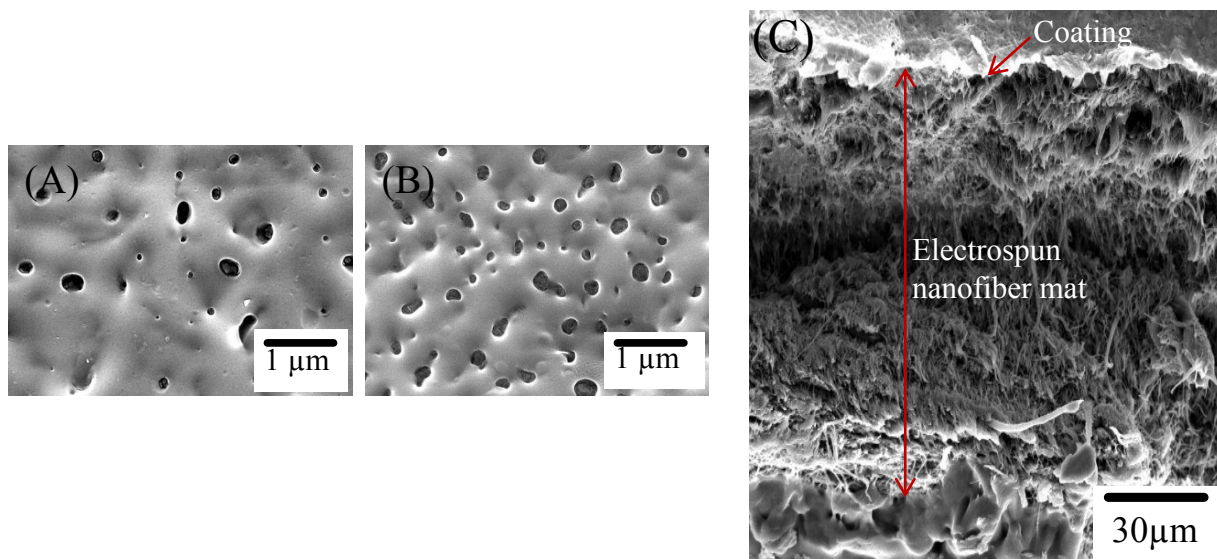


Figure 3-4. Surface FE-SEM images of the PVAc-coated electrospun membranes for (A) pristine N6 and (B) N6/SiO<sub>2</sub> (20 wt.%) composite, and (C) Cross-sectional FE-SEM image of PVAc-coated electrospun N6/SiO<sub>2</sub> (20 wt.%) composite membrane. The surface of the membranes was coated with Pt to capture these FE-SEM images. A 10 wt.% PVAc solution in acetone was used to fabricate the coating layer on the electrospun nanofiber mats through casting and then the phase inversion method.

### 3.3.2 Structural study of the nylon 6/SiO<sub>2</sub> composite by XRD and FTIR analysis

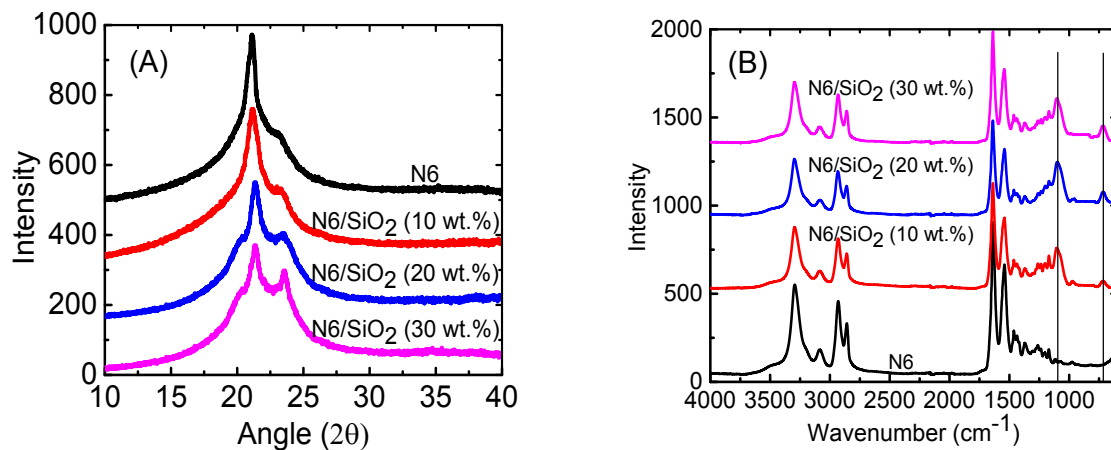


Figure 3-5. (A) XRD and (B) FTIR data for the nanofibers of pristine N6 and N6 with various SiO<sub>2</sub> contents (10, 20 and 30 wt.%). The X-ray source is copper and is equipped with a Vantec area detector.

Figure 3-5 A shows the XRD data for the nanofibers of the pristine N6 and the N6/SiO<sub>2</sub> composites with various SiO<sub>2</sub> contents. The XRD data of the pristine N6 shows a peak at  $2\theta = 21.2^\circ$  indicating the morphology of a semi-crystalline polymer containing crystals of  $\gamma$ -form, which is consistent with literature [108]. The incorporation of SiO<sub>2</sub> into N6 caused a reduction in the peak intensity and smaller peaks appeared as a result of the crystal structure splitting from  $\gamma$  ( $2\theta = 21.2^\circ$ ) into the  $\alpha$ -form at  $2\theta = 23.5^\circ$  [108]. As the SiO<sub>2</sub> content increased, the intensity of the peak at  $2\theta = 21.2^\circ$  decreased while the peak intensity at  $2\theta = 23.5^\circ$  grew. This occurred due to the increased transformation of the crystal structure from  $\gamma$ -form to  $\alpha$ -form with the addition of SiO<sub>2</sub> nanoparticles.

The FTIR spectra are exhibited in Figure 3-5 B. The FTIR spectrum of N6 nanofibers shows typical peaks at  $1545\text{ cm}^{-1}$  (N-H deformation),  $1637\text{ cm}^{-1}$  (C=O stretching) and  $3294\text{ cm}^{-1}$  (N-H stretching) [106]. These peaks can also be seen in the spectra for the 10, 20 and 30 wt.% SiO<sub>2</sub> contents for the N6/SiO<sub>2</sub> composite nanofibers. Two new peaks at  $1100\text{ cm}^{-1}$  and  $800\text{-}700\text{ cm}^{-1}$  were obtained due to incorporation of SiO<sub>2</sub> nanoparticles into the N6 nanofibers. The peak at  $1100\text{ cm}^{-1}$  was the characteristic signal of a Si-O-Si bond in the N6/SiO<sub>2</sub> composite [106]. The peak at  $800\text{-}700\text{ cm}^{-1}$  was obtained because of  $\nu(\text{Si-OH})$  in the N6/SiO<sub>2</sub> composite [64]. In fact,

hydrogen bonds were formed between the O atom of the hydroxyl group of the SiO<sub>2</sub> nanoparticles and the H atom of the amide group of N6 (Figure 3-7 E).

### 3.3.3 Wettability and surface roughness of the membrane

The wettability of the various films, nanofiber mats and membranes is exhibited in Table 3-1. The water contact angle of the casted N6 film was 71°. However, the water contact angle (static) of the electrospun (E.Spun) N6 nanofiber mat was reduced to 39° when the electrospinning technique was used rather than casting. The dynamic water contact angles of the E.Spun N6 nanofiber mat were also investigated and the obtained advancing and receding water contact angles of the E. Spun N6 nanofiber mat were shown to be 50° and 12°, respectively (Figure A-3, Appendix A). The very low receding water contact angle (12°) demonstrated excellent adhesion between the water droplet and the E. Spun N6 nanofiber mat. This increase of hydrophilicity is due to the capillary effect of the highly porous nanofiber mats [83]. A significant decrease in the water contact angle (39° to 15°) was observed when 20 wt.% SiO<sub>2</sub> nanoparticles were incorporated into the electrospun N6 nanofibers. The water contact angle of N6 nanofiber was 39° while SiO<sub>2</sub> nanoparticles were shown to be superhydrophilic. A water contact angle of 15° was obtained for the electrospun N6/SiO<sub>2</sub> composite due to the synergistic effect of N6 and SiO<sub>2</sub> nanoparticles, even though the SiO<sub>2</sub> nanoparticles were wrapped in the interior of the electrospun nanofibers. PVAc was used as the coating material on the electrospun nanofiber mats which was determined to have a water contact angle of 49°, comparable with the value from other literature (45°) [109]. After coating the surface of the electrospun nanofiber mats, the water contact angles were increased from 39 to 43° and from 15 to 21° for the electrospun N6 and N6/SiO<sub>2</sub> composite, respectively. Nonetheless, the water contact angles of PVAc-coated N6 and N6/SiO<sub>2</sub> composite membranes were both lower than that of pristine PVAc film because of the hydrophilic effect of the E.Spun N6 and N6/SiO<sub>2</sub> nanofiber mats. In addition, the water droplet was quickly absorbed through the PVAc-coated N6/SiO<sub>2</sub> electrospun membrane after touching its surface during the contact angle measurement (Figure 3-6 A), indicating the highly hydrophilic property of the membrane [110]. It took 1 sec to completely immerse the water droplet through the membrane (Figure 3-6 A). The water contact angles for the commercial (Comm.) PVDF and PSf membranes were 123° and 45°, respectively, indicating the hydrophobic (PVDF) and hydrophilic (PSf)

properties. The water droplet was stable on the surface of the PVDF membrane, however, the water droplet was quickly absorbed through the PSf membrane after touching its surface and that was completely absorbed in 2.5 sec by the membrane (Figure 3-6 B). The surface roughness can increase the fouling propensity of membrane; therefore, the electrospun N6/SiO<sub>2</sub> composite membrane was coated by PVAc in order to decrease its surface roughness. The average surface roughness ( $R_a$ ) of the electrospun N6 nanofiber mat was 193 nm (Figure 3-6 C). However, the average surface roughness of the the electrospun N6 nanofiber mat increased to 285 nm due to the addition of surface-active SiO<sub>2</sub> nanoparticles (Figure 3-6 D), which was reduced to 120 nm after coating with PVAc (Figure 3-6 E). Moreover, the coating was designed to reduce the pore size of the electrospun N6/SiO<sub>2</sub> composite nanofiber mat. The average pore size of the composite nanofiber mat was 455 nm, however it was reduced to 170 nm after being coated with PVAc (Figure A-4, Appendix A).

Table 3-1. Water contact angles of nanoparticle and the various films/nanofiber mats/membranes.

Nanoparticle/Film/Nanofiber mat/Membrane	Water contact angle (°)
SiO <sub>2</sub> nanoparticle	0
N6 film	71 ± 2
PVAc film	49 ± 2
E.Spun N6 nanofiber mat	39 ± 1
E.Spun N6/SiO <sub>2</sub> (20 wt.%) nanofiber mat	15 ± 1
PVAc-coated E.Spun N6 membrane	43 ± 1.5
PVAc-coated E.Spun N6/SiO <sub>2</sub> (20 wt.%) membrane	21 ± 1
Commercial PSf membrane	45 ± 2
Commercial PVDF membrane	123 ± 3

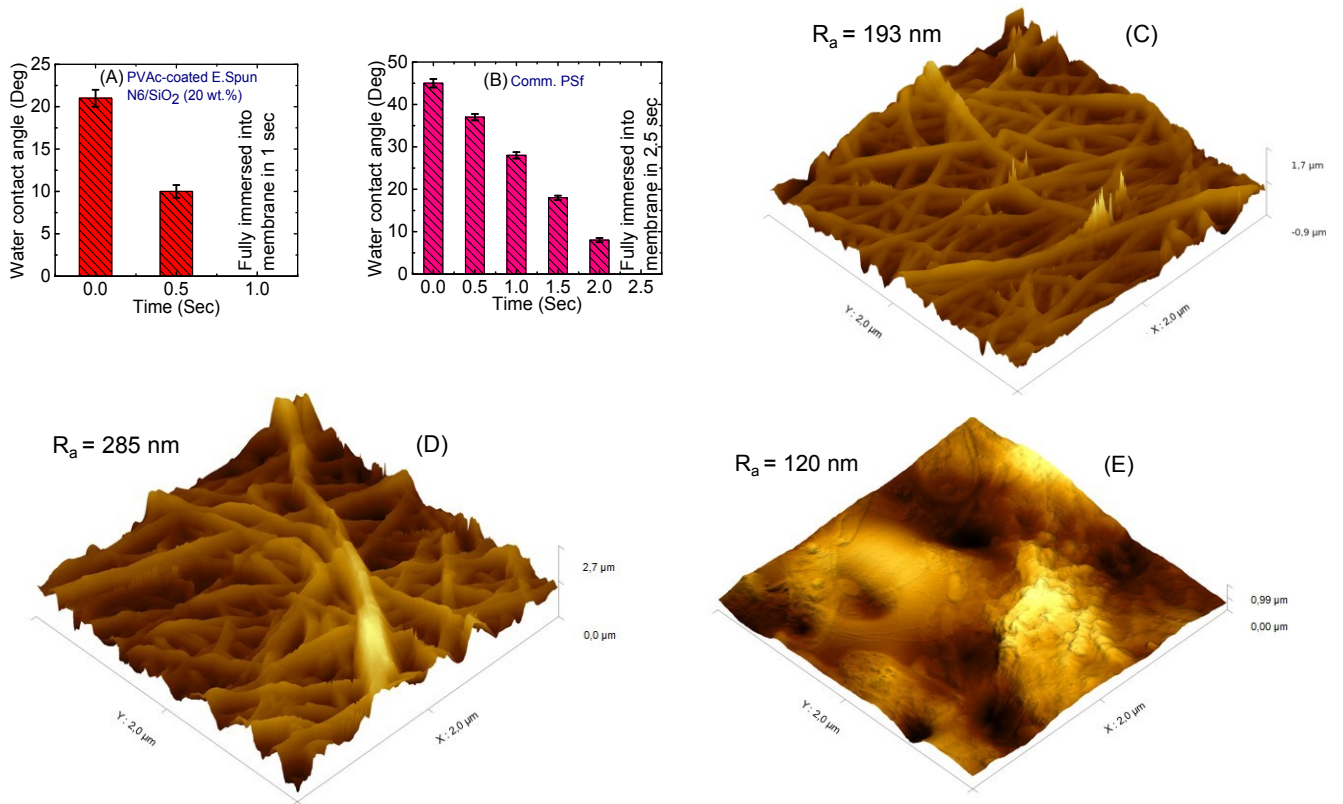


Figure 3-6. (A) The variation of water contact angle as a function of time for the PVAc-coated E.Spun N6/SiO<sub>2</sub> (20 wt.%) composite membrane, (B) The variation of water contact angle as a function of time for the commercial PSf membrane, AFM images of (C) E.Spun N6, (D) E.Spun N6/SiO<sub>2</sub> (20 wt.%) composite and (E) PVAc-coated E.Spun N6/SiO<sub>2</sub> (20 wt.%) composite.

### 3.3.4 Porosity, pore size, pore size distribution and tensile strength of the membranes

The variations in the porosity of the different electrospun membranes are shown in Figure 3-7 A. The electrospun N6 membrane with 21 wt% of N6 solution exhibited high porosity (81%) due to the high surface area to volume ratio of the nanofibers. The porosity of the N6 nanofiber mat was reduced by 18% after being coated with PVAc. However, the incorporation of SiO<sub>2</sub> nanoparticles (20 wt%) increased the porosity of the N6 nanofibers by 11% due to the porous structure of the SiO<sub>2</sub> nanoparticles [84]. The porosity of the N6/SiO<sub>2</sub> composite nanofiber mat was decreased from 92% to 78% with the pore sizes of 170 nm (average) and 295 nm

(maximum) after being coated with PVAc (Figure 3-7 A and Figure 3-7 B). The pore size distributions of the fabricated as well as the commercial membranes are exhibited in Figure 3-7 C. The average pore sizes were 170, 200, and 220 nm for the fabricated, commercial PSf, and commercial PVDF membranes, respectively. However, the pore sizes ranged from 100 to 300 nm, 115 to 309 nm, and 126 to 328 nm for the fabricated, commercial PSf, and commercial PVDF membranes, respectively. The PVAc-coated N6/SiO<sub>2</sub> composite membrane had a 15% higher porosity than that of the PVAc-coated N6 membrane due to the higher hydrophilicity of the N6/SiO<sub>2</sub> nanofiber mat. Compared to the pristine N6 nanofiber mat, the presence of superhydrophilic SiO<sub>2</sub> nanoparticles in the N6/SiO<sub>2</sub> composite nanofiber mats strongly facilitated the diffusion of water from the coagulation bath to the PVAc-coated electrospun nanofiber mats, leading to the development of pore density in the membrane.

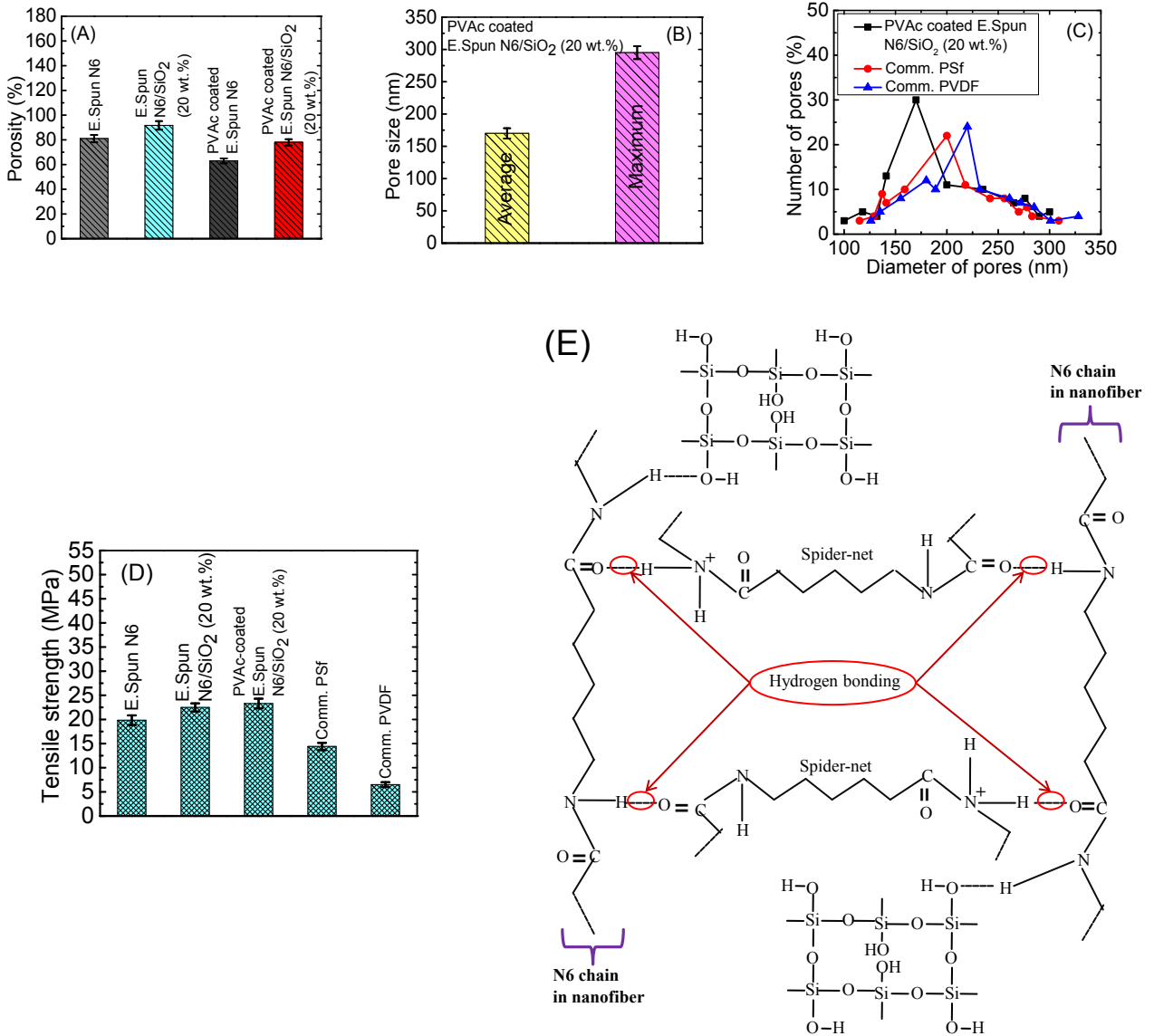


Figure 3-7. (A) Effect of SiO<sub>2</sub> nanoparticles and PVAc coating on the porosity of the electrospun N6 membrane, (B) Pore size of the PVAc-coated electrospun N6/SiO<sub>2</sub> composite membrane, (C) Pore size distribution of membranes, (D) Tensile strength of the fabricated and commercial PSf and PVDF membranes and (E) Schematic representation of the electrospun N6/SiO<sub>2</sub> composite. The porosity, average pore size and maximum pore size of each membrane were investigated via the gravimetric method, filtration velocity method and bubble point method, respectively.

The tensile strength of the fabricated membranes is exhibited in Figure 3-7 D. The E.Spun N6 nanofiber mat showed a tensile strength of 19.84 MPa, which is much higher than that of commercial PSf (tensile strength 14.4 MPa) and PVDF (tensile strength of 6.5 MPa) membranes. The higher tensile strength of the E.Spun N6 was obtained due to the highly interconnected spider-net like structure in the N6 nanofiber mats. The ionic species of the N6 solution can form stronger hydrogen bonds because of the extra available charge on them in the presence of high applied voltage during the electrospinning process. The protonated amide group of ionic N6 can effectively form hydrogen bonds with oxygen atoms of a N6 molecule in the main fiber and form another hydrogen bond between an oxygen atom in the ionic molecule and a hydrogen atom from the amide group of another main fiber to form the interconnected spider-net like nanofiber mats (Figure 3-7 E). The incorporation of SiO<sub>2</sub> nanoparticles enhanced the tensile strength of the electrospun N6 nanofiber mats (22.48 MPa), most likely due to the integrated network structure of SiO<sub>2</sub> (Figure 3-7 E). The tensile strength of the N6/SiO<sub>2</sub> composite nanofiber mat slightly increased (23.3 MPa) after being coated with PVAc. The PVAc created a compression effect on the membrane surface increasing the tensile strength of the PVAc-coated N6/SiO<sub>2</sub> composite nanofiber mats.

### 3.3.5 Permeation and rejection of the membrane

The pure water permeability and oil rejection of the fabricated and commercial MF membranes are presented in Figure 3-8. In Figure 3-8 A, Figure 3-8 B and Figure 3-8 C, it was observed that the water flux increased linearly with an increase in applied pressure from 0.28 bar (4 psi) to 1.38 bar (24 psi). This increase was gradually attained in 0.28 bar (4 psi) increments. It was also observed that the value of the water permeability at each applied pressure was constant for all the three types of membranes (4814, 2728 and 1015 LMH/bar for the fabricated, PSf and PVDF membranes, respectively) (Figure 3-8 A, Figure 3-8 B and Figure 3-8 C), which indicates that no deformation of structural parameters of the membranes occurred when increasing the applied pressure. The water permeability of the PVAc-coated N6/SiO<sub>2</sub> composite membrane was much higher than that of the commercial PSf and PVDF membranes due to its higher hydrophilicity.

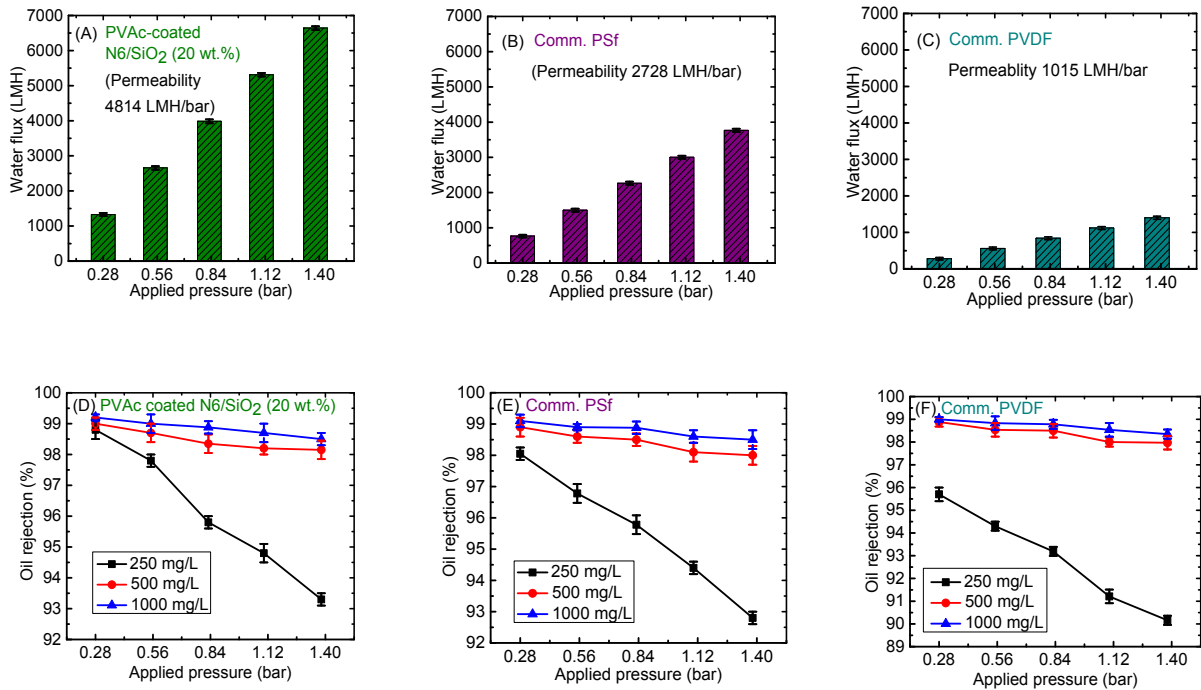


Figure 3-8. Effect of applied pressure on the pure water flux for (A) the fabricated PVAc-coated electrospun N6/SiO<sub>2</sub> composite membrane with a mean pore size of 170 nm, (B) the commercial PSf membrane with a mean pore size of 200 nm and (C) the commercial PVDF membrane with a mean pore size of 220 nm, and on the rejection of oil by (D) the fabricated PVAc-coated electrospun N6/SiO<sub>2</sub> composite membrane, (E) the commercial PSf membrane and (F) the commercial PVDF membrane. A dead-end stirred cell filtration device connected to a nitrogen gas cylinder was used to investigate the pure water permeability and oil rejection at a stirring rate of 500 rpm and applied pressure, in bar, of 0.28 (4 psi), 0.55 (8 psi), 0.83 (12 psi), 1.1 (16 psi) and 1.38 (20 psi) at 25°C.

The rejections of the membranes were conducted with O/W emulsions. The size distribution of oil droplets in the O/W emulsions with concentrations of 250 mg/L, 500 mg/L, and 1000 mg/L at the same homogenizing conditions are presented in the Figure 3-9 A. As can be seen from this figure, the size range of oil droplets varies between 0.31  $\mu\text{m}$  – 0.73  $\mu\text{m}$  with an average size of 0.435  $\mu\text{m}$ , 0.71  $\mu\text{m}$  – 1.22  $\mu\text{m}$  with an average size of 0.85  $\mu\text{m}$ , and 1.36  $\mu\text{m}$  – 2.03  $\mu\text{m}$  with an average size of 1.58  $\mu\text{m}$  for oil concentrations of 250 mg/L, 500 mg/L, and 1000 mg/L, respectively. At the same homogenizing conditions, the size of the oil droplets increased with

increasing oil concentration, which is found to be a trend in literature as well [111]. In fact, the increase in oil content causes a higher interaction between the oil droplets and water through the surfactant which enhances the size of oil droplets. The stability of the oil droplets was investigated for the oil concentration of 250 mg/L right after the preparation of the sample and again after 24 h. The size distribution at both these times was similar demonstrating the good stability of the emulsions (Figure 3-9 B).

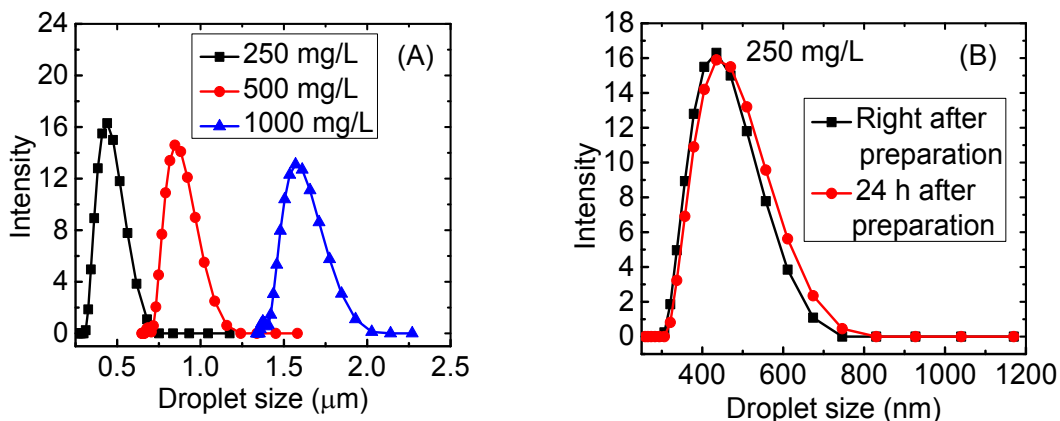


Figure 3-9. Size distributions (A) and Stability (B) of oil droplets.

Figure 3-8 D represents the rejection of oil as a function of applied pressure for various oil concentrations (250 mg/L, 500 mg/L and 1000 mg/L) for the fabricated membrane and 98.80%, 99%, and 99.20% oil rejections were obtained with these oil concentrations, respectively, at the applied pressure of 0.28 bar. It was also noted that the percentage of oil rejection decreased with an increase of applied pressure for lower oil concentration (250 mg/L). The reason behind this is that some smaller oil droplets at the 250 mg/L oil concentration level permeated through the membrane pores and reached the permeate side at higher applied pressures. However, the oil rejections were almost constant for higher oil concentrations (500 mg/L and 1000 mg/L) due to the relatively higher size of oil droplets (Figure 3-8 D). The almost identical trend of oil rejection was obtained for the commercial PSf membrane at high concentrations (500 mg/L and 1000 mg/L) due to high oil droplet sizes at these two concentrations (Figure 3-8 E). However, oil rejection was lower at an oil concentration of 250 mg/L at various applied pressures due to the lower hydrophilicity and the slightly higher pore size for the commercial PSf membrane as

compared to the fabricated membrane (Figure 3-8 E). The oil rejection trends of the commercial PVDF membrane were also identical to the fabricated and the commercial PSf membranes for 500 and 1000 mg/L oil concentrations because of the higher oil droplet sizes in these two concentrations (Figure 3-8 D, Figure 3-8 E and Figure 3-8 F). However, the commercial PVDF membrane had lower oil rejections than the other two types of membranes for 250 mg/L oil concentration due to the combined effect of hydrophobicity and the slightly higher pore size of the membrane (Figure 3-8 F). A comparison list of performance of the fabricated PVAc-coated E.Spun N6/SiO<sub>2</sub> (20 wt.%) composite membrane with other MF membranes is shown in Table 3-2.

Table 3-2. List of fabricated (for oil-water separation) and commercial MF membranes to compare their performance.

Membrane		Supplier	Av. pore size (nm)	Permeability (LMH/bar)	Oil rejection	Reference
Fabricated	TiO <sub>2</sub> decorated superhydrophilic PVDF membrane	-	210	890	99%	[59]
	Poly(lysine methacrylamide)-grafted PVDF	-	220	2500	99%	[60]
	PVAc-coated E.Spun N6/SiO <sub>2</sub> (20 wt.%) composite	-	170	4814	99%	This research
Commercial	Polypropylene	Membrana GmbH, Germany	200	5075	-	[112]
	Poly(vinylidene fluoride)	Cobetter filtration, China	200	3988	-	[113]
	Polyvinyl chloride	Polychim, Devnya, Bulgaria	300	537	-	[114]
	Polyamide	GE Whatman, UK	200	5017	-	[115]

### 3.3.6 Antifouling propensity and stability of the membrane

Membrane fouling is an inevitable process during wastewater filtration. The fouling process can be segmented into three steps. First, the pore clogging period; second, the cake build-up

period on the membrane surface; and third, the cake filtration period according to the changes of the membrane flux [101,116]. Figure 3-10 A, Figure 3-10 B and Figure 3-10 C show the permeability as a function of time for the fabricated PVAc-coated E.Spun N6/SiO<sub>2</sub> (20 wt.%), commercial PSf and commercial PVDF membranes, respectively, for filtration of O/W emulsion (1000 mg/L). As shown in Figure 3-10 A, Figure 3-10 B and Figure 3-10 C, membrane fluxes dropped dramatically during the first 7 min (pore clogging period), and then declined slowly (cake build-up period) and eventually the fluxes became steady (cake filtration period) after 70 min for the fabricated membrane, 65 min for the commercial PSf membrane and 50 min for the commercial PVDF membrane. During the pore clogging stage (first stage), the fouling rate depends largely on the pore size and porosity of the membrane, which cannot fully reflect the antifouling properties of the membranes. Moreover, the fouling rate in the cake filtration stage (third stage) is closely related to the structure of the cake layer formed during oil droplet filtration. In the second stage, the formation rate of the cake layer on the membrane surface is closely interrelated with the fouling rate of the membrane. Thus, the slopes of the fitted linear curves of  $dt/dV$  versus  $V$  for all the three types of membranes in the second stage are considered as the fouling rate of the membrane (Figure A-5, Appendix A). The specific cake resistances (calculated from the fitted line curves) were 0.000088, 0.00018 and 0.07976 for the fabricated, commercial PSf and commercial PVDF membranes, respectively. The antifouling properties in terms of water flux recovery of the fabricated membrane, and the commercial PSf and PVDF membranes using O/W emulsion is exhibited in Figure 3-10 D and in the supporting information (Table A-4, Appendix A). The increasing of water flux recovery means increasing of antifouling propensity of a membrane. The obtained water flux recovery of the fabricated, commercial PSf and commercial PVDF membranes were 85%, 74% and 23%, respectively. The higher water flux recovery of the fabricated membrane was achieved due to its hydrophilic nature and very low value of specific cake resistance (0.000088). The high flux recovery of the fabricated membrane demonstrated the antifouling propensity of the membrane [99-101]. To understand the improved antifouling performance of the fabricated membrane, the oil contact angle under water was also investigated (Figure A-6, Appendix A). In order to investigate oil contact angle under water, the membrane was first immersed into water, then the oil contact angle on the wetted-surface of the membrane was measured. The highly hydrophilic

surface (water contact angle of  $21^\circ$ ) shifted to oleophobic after immersing the membrane into water. The oil contact angle on the oleophobic membrane surface was  $116^\circ$ , which indicated a repulsion between oil droplets and the wetted-membrane surface.

In order to investigate structural stability, the permeability of the PVAc-coated E.Spun N6/SiO<sub>2</sub> (20 wt.%) membrane was measured as a function of time for a duration of 3 h using DI water, acidic water (pH 4) and alkaline water (pH 10) (Figure 3-10 E). The permeability of the membrane for all three types of liquids was the same (about 4828 LMH/bar) over the 3 h. The water contact angles of the membrane were also measured after the permeation of each liquid and were compared to that of the membrane before permeation. The water contact angles of the membrane before and after permeation were the same ( $21^\circ$ ) (Figure 3-10 F). This result indicated the stability of the membrane in which there was a strong interaction between the electrospun nanofiber mat and the PVAc coating through the interaction between the polar amide groups of N6 and the polar ester groups of PVAc.

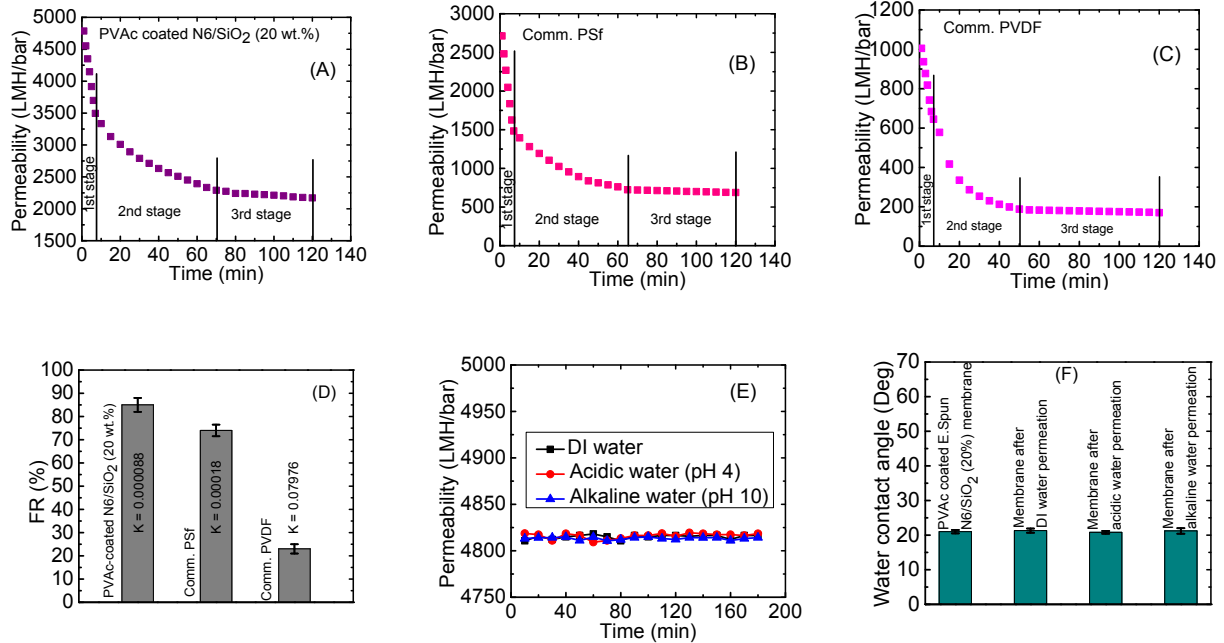


Figure 3-10. Permeability as a function of time for the (A) fabricated, (B) commercial PSf and (C) commercial PVDF membranes for O/W emulsion, (D) the water flux recovery for the fabricated and commercial PSf and PVDF membranes, and (E) permeability as a function of time for DI, acidic and alkaline water and (F) the water contact angles of the PVAc-coated E.Spun N6/SiO<sub>2</sub> (20%) membrane before and after the permeation of DI, acidic and alkaline water.

### 3.4 Conclusions

A novel PVAc-coated electrospun N6/SiO<sub>2</sub> composite microfiltration membrane was fabricated for the separation of oil from O/W emulsions. The successful fabrication of electrospun N6/SiO<sub>2</sub> composite nanofibers was confirmed via FE-SEM, TEM, XRD and FTIR analyses. The FE-SEM was also used to investigate the morphology of the surface of the PVAc-coated N6/SiO<sub>2</sub> composite membrane. The fabricated membrane was highly hydrophilic (water contact angle 21°) with both high porosity and mechanical strength. The fabricated membrane also showed a high water flux of 4814 LMH/bar and almost 99% oil rejection at oil concentrations of 250 mg/L, 500 mg/L and 1000 mg/L in the feed mixture. The water flux recovery of 85% for the fabricated membrane using O/W emulsion, indicated the antifouling properties of the membrane. The membrane was also stable due to a beneficial interaction

between the electrospun nanofiber mat and the PVAc coating. Depending on the obtained performance of the membrane, it can be concluded that the novel fabricated microfiltration membrane has a huge potential for the separation of O/W emulsions.

#### Acknowledgements

Md. Saifur Rahaman gratefully acknowledges the FRQNT for providing funding support for this project. Md. Shahidul Islam acknowledges the support of a doctoral-level scholarship from the FRQNT. The authors also acknowledge ongoing support from Concordia University, Canada.

## **Chapter 4: Forward Osmosis Treatment of Fracking Wastewaters: Evaluation of Suitable Organic Draw Solutions**

### *Abstract*

The selection of an appropriate draw solution is crucial to the successful implementation of desalination of highly saline fracking wastewaters via the FO process. In this report, four organic compounds, such as potassium acetate, potassium formate, sodium glycolate, and sodium propionate were identified as candidate draw solutes for desalination of fracking wastewater by FO process. In the FO treatment of synthetic fracking wastewater (15.68 MPa osmotic pressure) using the identified draw solutions at 18.48 MPa osmotic pressure, the observed average water fluxes (over 6 h) ranged between 10.50 and 13.26 LMH with high rejection of inorganic and organic contaminants. However, comparatively higher average water fluxes (19.05 to 24.05 LMH) were obtained for the real fracking wastewater (osmotic pressure 12.83 MPa) with high rejection of inorganic and organic contaminants. Higher water flux was obtained due to a higher osmotic pressure difference between the draw and feed solutions for the real fracking wastewater as compared to that for synthetic fracking wastewater. For recycling these identified draw solutes, membrane distillation could be used as downstream separation techniques in the FO process.

**Keywords:** Organic draw solutions; Forward osmosis process; Fracking wastewaters; Desalination

## 4.1 Introduction

Shale gas is a major source of natural gas and a large amount is being produced across the United States (about 37 billion cubic feet/day) [4, 117-120]. Vast amounts of gas have been harvested from shale plays through the process of hydraulic fracturing (“fracking” for short) [121]. Fracking involves injecting fluid into the ground at high pressure in order to crack shale rocks, ultimately releasing the gas within. In this process, a hole is drilled to the shale layer, after which a sand/water/proppant (chemical) mixture is pumped to the shale layer at high pressure. Consequently, this induces fissures through the shale layer, and natural gas is released and flows back to the surface along with the drilling fluids. Managing these flowback fluids constitutes a major environmental challenge for fracking operations [17, 19-20]. The waters can vary in salinity, contain a variety of salts, and be laden with oils, sand and fracking chemicals [19, 21-24]. This mixture of contaminants makes treatment options challenging to implement.

Technologies, such as mechanical vapor compression, reverse osmosis, membrane distillation, and forward osmosis have all been investigated to desalinate fracking wastewater [24]. Mechanical vapor compression and reverse osmosis are energy-intensive processes and the composition of fracking wastewater creates distinct challenges in the membrane distillation (most notably fouling and wetting) [24]. Forward osmosis has been proposed to treat fracking wastewater as well, possibly with economic advantages over these more conventional processes [24]. The primary concept underlying this process is the osmotic transport of water (water flux) through a semi-permeable membrane from a low salinity feed solution to a high salinity draw solution [122-128]. A downstream separator integrated for the recovery of draw solutions is important for successful implementation of the FO process. The schematic representation for the FO process with the downstream separator is shown in supporting information (Figure B-1). In the FO process, the thermal distillation and membrane distillation processes can be used to recover thermolytic and distillable draw solutes, respectively, using industrial waste heat [129-130].

The efficacy of membrane based osmotic processes is highly dependent on the membrane and the draw solute used. A significant amount of research has been conducted into improving membrane performance, but there is still opportunity for more research into draw solutes. The selection of a suitable draw solute is dependent upon a number of criteria, such as

high diffusivity, low viscosity, high osmotic pressure, low reverse salt flux, and an effective regeneration method [125]. Those compounds with high water solubility and a high degree of dissociation are potential candidates for draw solutes [131]. In recent years, inorganic salts [132] and various synthetic organic compounds [133-134] have been tested as draw solutes to generate osmotic pressure. These studies have shown that draw solutions with higher water flux to reverse salt flux ratios are the most effective for osmotic processes.

Currently, there is a gap in the literature identifying those effective draw solutions that can make the FO process commercially viable. Previously, Hickenbottom et al. and Bowden et al., and Corzo et al. studied organic draw solutions for application in osmotic heat engines, in osmotic membrane bioreactors, and for reclamation of effluents released from wastewater treatment plant, respectively [130,135-136]. In this paper—for the first time—we report on four organic draw solutes (potassium acetate, potassium formate, sodium glycolate and sodium propionate) effective for desalination of highly saline fracking wastewaters (synthetic and real) via the FO process. These draw solutes were chosen because of their high osmotic pressure with very low specific reverse salt flux in FO process.

#### 4.2 Selection of organic draw solutions

Figure 4-1 represents the method used to select organic draw solutes. Initially, 550 organic compounds were screened to obtain the desired draw solutions. Those compounds that were not solid at room temperature and standard atmospheric pressure, and that were not soluble in water were eliminated by a desktop screening method, creating a shortlist of the remaining chemicals. The osmotic pressures of the draw solutions, as a function of concentration, were then determined using the OLI Stream Analyzer™ (OLI Systems, Inc.). Those draw solutions that had an osmotic pressure lower than 15.68 MPa (the osmotic pressure of fracking wastewater determined in our laboratory) at saturation concentration were excluded to obtain the desired draw solutes. At the end of the selection process, seven organic compounds were obtained as desired organic draw solutes. The obtained organic draw solutes were potassium acetate, ammonium acetate, ammonium carbamate, ammonium formate, potassium formate, sodium glycolate, and sodium propionate.

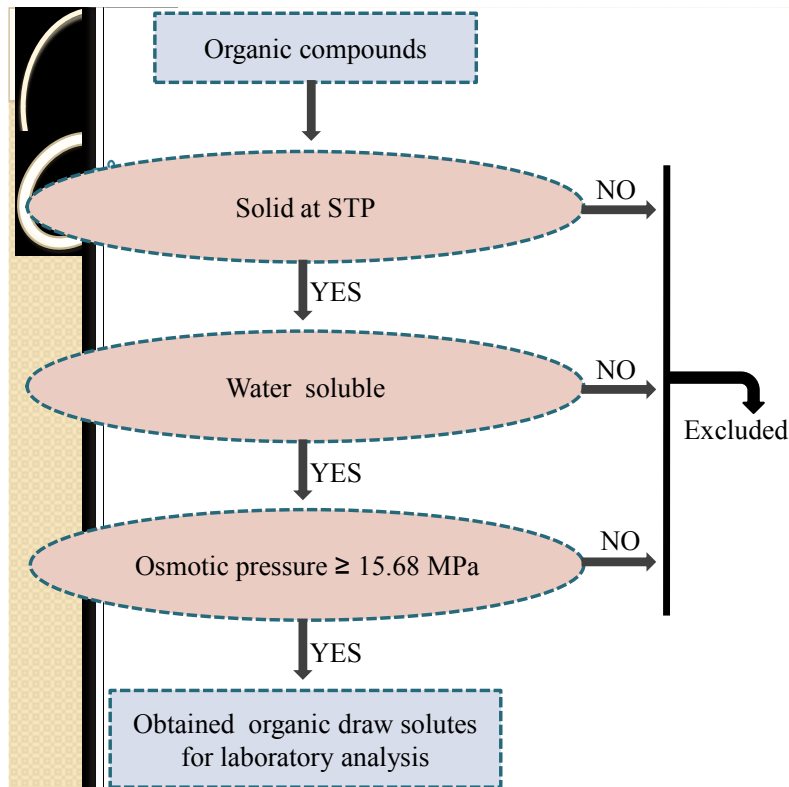


Figure 4-1. Flow chart for the selection of the organic draw solutes.

### 4.3 Experimental

#### 4.3.1 Solution of the draw solutes

Certified ACS-grade organic compounds from Sigma-Aldrich, USA were used to make all draw solutions. These included potassium acetate (KAc), ammonium acetate (NH<sub>4</sub>Ac), ammonium carbamate (NH<sub>4</sub>C), ammonium formate (NH<sub>4</sub>F), potassium formate (KF), sodium glycolate (NaGly), sodium propionate (NaP), and sodium chloride (NaCl). DI water (Millipore, Billerica, MA) was used as the feed stream in all experiments. The concentration of each draw solution at 2.8 MPa osmotic pressure (the literature established osmotic pressure at which draw solutions were investigated against DI water as feed solution in FO process [132,135]) was determined using the OLI Stream Analyzer™ (OLI Systems, Inc.) (Table 4-1). The OLI Stream Analyzer™ was also used to find the mutual diffusivity (D), viscosity, solubility, and osmotic pressure at solubility for each draw solution (Table 4-1).

Table 4-1. Properties of the draw solutions at the temperature of 24°C.

Draw solution	D ( $\times 10^{-9} \text{ m}^2/\text{s}$ )	At 2.8 MPa osmotic pressure		Solubility (g/L)	Conc. (M) at solubility	Osmotic pressure (MPa) at solubility
		Conc. (M)	Viscosity (cP)			
KF	1.3477	0.68	1.00	2713.60	32.26	130
KAc	0.9873	0.66	1.02	2570	26.19	108
NH <sub>4</sub> F	1.322	0.62	1.03	1427	22.63	101
NH <sub>4</sub> C	1.250	0.38	0.98	580	6.60	45.20
NaP	1.643	0.69	0.98	1000	10.41	41.80
NH <sub>4</sub> Ac	1.155	0.91	1.00	1430	18.55	33.10
NaGly	1.547	0.73	1.04	650	6.56	24.60
NaCl	1.38	0.61	0.99	359	6.14	27.40

#### 4.3.2 Membrane performance evaluation

A flat sheet TFC forward osmosis membrane (Hydration Technology Innovations, HTI, Albany, OR) was used to conduct all FO experiments. The water permeability coefficient (A) and salt permeability coefficient (B) for the TFC membrane were investigated using a flat-sheet bench-scale cross-flow RO test system. A piece of the membrane, with an effective surface area of 19.94 cm<sup>2</sup>, was placed in a stainless steel test cell with the active surface of the membrane facing the feed stream. Using a high-pressure positive displacement pump (Hydra-cell pump), the feed solution was re-circulated at the flow rate of 1.0 L/min. DI water was used as the feed stream to investigate A, and a 20 mM solution of each draw solute was used as the feed stream to investigate R (rejection) and B for the TFC membrane. A, R, and B for the membrane were determined using the following equations [137-140]:

$$J = \frac{\Delta V}{A_m \Delta t} \quad (4-1)$$

$$A = \frac{J}{\Delta P} \quad (4-2)$$

$$R (\%) = \frac{C_f - C_p}{C_f} \times 100 \quad (4-3)$$

$$B = \frac{A(1-R)(\Delta P - \Delta \pi)}{R} \quad (4-4)$$

where J is the pure water flux, A<sub>m</sub> is the effective membrane area, ΔV is the permeate volume, Δt is time, ΔP is the hydraulic pressure difference across the membrane, C<sub>f</sub> is the salt concentration of the feed solution, C<sub>p</sub> is the salt concentration of the permeate solution, and Δπ

is the osmotic pressure of the feed solution. Conductivity of the feed and permeate solutions was investigated using a calibrated conductivity meter (Oakton, Eutech Instruments) to calculate solute rejection.

The pressure was increased in 0.345 MPa increments from 0.345 to 1.034 MPa to investigate A of the TFC membrane. Constant pressure was applied at each increment for 8 h. Water flux through the membrane was obtained from a liquid flow sensor (Sensorion, The Sensor Company) that was directly connected to a computer. To investigate R and B, 1.896 MPa pressure was applied to the RO cell. The salt concentration of the permeate solution was investigated using a calibrated conductivity meter (Oakton, Eutech Instruments). This experiment was conducted at a constant temperature of 24°C using a chiller (Polystat, Cole-Parmer).

A flat-sheet bench-scale FO test system was used to determine the structural parameter (S) of the TFC membrane by applying the following equation [138-139,141-142]. In this approach, de-ionized water was used as the feed solution, while the draw solutes were held at a concentration at 2.8 MPa osmotic pressure.

$$S = \left( \frac{D}{J_w} \right) \ln \left[ \frac{A\pi_{\text{draw}} + B}{A\pi_{\text{feed}} + J_w + B} \right] \quad (4-5)$$

where  $J_w$  is the FO water flux for the draw solutions.

#### 4.3.3 FO experiment for the draw solutions

A bench-scale experimental setup (Figure 2-6) was used to evaluate the FO performance of the draw solutions with commercially available TFC membranes. A piece of the membrane with an effective surface area of 19.94 cm<sup>2</sup> was placed in an acrylic cross-flow cell with the active layer of the membrane facing the feed stream. On both sides of the membrane, the cross-flow cell had symmetric channels, which allowed for both the feed solution and the draw solution to flow tangentially to the membrane. Recirculation of the feed and draw solutions on opposite sides of the membrane was executed by two variable-speed gear pumps (Gear Pump Drive, Cole-Parmer Instrument Company). The flow rate of each solution was maintained at 0.5 L/min. The feed solution temperature and draw solution temperature were held constant at 24 °C and monitored with a thermometer. The feed solution and the draw solution were placed in two separate 4.0 L reservoirs to conduct the experiment. The feed solution container was placed on a digital analytical balance. The water flux and the reverse salt

flux were determined to evaluate the FO performance of the draw solutions. Each experiment was conducted for one hour and the concentration of the draw solution was adjusted by adding concentrated draw solution in every 15 min. The water flux of the draw solution was obtained from the digital analytical balance using the equation (4-1). A sample of the feed solution was collected before and after the experiment to determine the salt concentration using a calibrated conductivity meter (Oakton, Eutech Instruments) to investigate the reverse salt flux. A digital analytical balance was used to determine initial and final volume of the feed solution. Reverse salt flux was calculated by the following equation (4-6) [143]:

$$J_s = \frac{C_{f,e}V_{f,e} - C_{f,i}V_{f,i}}{A_m \Delta t} \quad (4-6)$$

where  $C_{f,e}$  and  $V_{f,e}$  are the salt concentration and total volume of the feed at the end of the tests, respectively, and  $C_{f,i}$  and  $V_{f,i}$  are the initial salt concentration and total volume of the feed, respectively.  $A_m$  and  $\Delta t$  are the effective membrane area and FO experiment conducting time, respectively.

#### 4.3.4 Investigation of thermolytic and thermally distillable properties of the draw solutes

The thermolytic and thermally distillable properties of the draw solutes were investigated using the gravimetric method. In this method, a fixed weight ( $W_1$  g) of a draw solute was taken and then a solution of the draw solute was prepared in DI water. Afterwards, the draw solution was heated in a beaker (liquid surface area  $18.09 \text{ cm}^2$ ) at  $50 \text{ }^\circ\text{C}$  to evaporate all the water and then the residue was weighed ( $W_2$  g).

If  $W_1 = W_2$ , the draw solute is distillable.

If  $W_1 > W_2$ , the draw solute is thermolytic.

Afterwards, the osmotic pressures of the residue from the distillable draw solutes were investigated using a Micro-Osmometer (Precision Systems) at  $24^\circ\text{C}$ . The Micro-Osmometer can determine osmolality (Osmol/kg) of each draw solution. Then osmolality was converted to molality (mol/kg) for each draw solution. Finally, the following equation (4-7) was used to calculate osmotic pressure [123]:

$$\pi_{o,p} = \rho_w R_i T m \quad (4-7)$$

where  $\pi_{o,p}$  is the osmotic pressure,  $\rho_w$  is the density of the solvent (water),  $R_i$  is the molar gas constant,  $T$  is absolute temperature, and  $m$  is the molality.

#### 4.3.5 Fracking wastewaters

Synthetic fracking wastewater was prepared in our laboratory according to the composition demonstrated by literatures (Table 2-1) [19, 21-24]. Sodium carbonate, sodium sulfate, sodium chloride, ferric chloride, barium chloride, magnesium chloride, manganese chloride, strontium chloride, calcium bromide, calcium chloride, potassium chloride, isopropanol (C<sub>3</sub>H<sub>8</sub>O), ethylene glycol (C<sub>2</sub>H<sub>6</sub>O<sub>2</sub>), N,N-dimethyl formamide (DMF), and glutaraldehyde (C<sub>5</sub>H<sub>8</sub>O<sub>2</sub>)—all obtained from Sigma Aldrich, USA—machine oil (Canadian Tire, Canada), sand (size less than 38 μm, Quikrete, USA), and DI water (Millipore, Billerica, MA) were used to prepare the synthetic fracking wastewater. First, oil was added into DI water and then ultrasonicated for 30 min to prepare oil-in-water emulsion with an oil content of 0.7 g/L. Afterwards, sodium carbonate, sodium sulfate, sodium chloride, ferric chloride, barium chloride, magnesium chloride, manganese chloride, strontium chloride, calcium bromide, calcium chloride, potassium chloride, isopropanol, ethylene glycol, N,N-dimethyl formamide, glutaraldehyde, and sand with concentrations of 1.166, 0.741, 110.016, 0.16, 7.136, 7.917, 0.016, 12.286, 2, 84.915, 1.182, 0.668, 0.473, 0.019, 0.011, and 2.5 g/L, respectively, were added to the emulsion under magnetic stirring (350 rpm) to prepare the synthetic fracking wastewater.

The true fracking wastewater sample was obtained from Canbriam Energy Inc., Calgary, Alberta, Canada. The composition of inorganic dissolved solids of this wastewater is provided in Table 4-2.

Table 4-2. Composition of inorganic dissolved solids of the real fracking wastewater.

Component	Conc. (mg/L)
Sodium (Na <sup>+</sup> )	54400
Potassium (K <sup>+</sup> )	1950
Calcium (Ca <sup>2+</sup> )	8010
Magnesium (Mg <sup>2+</sup> )	909
Barium (Ba <sup>2+</sup> )	501
Strontium (Sr <sup>2+</sup> )	1490
Iron (Fe <sup>2+</sup> )	29.5
Chloride (Cl <sup>-</sup> )	109186
Bromide (Br <sup>-</sup> )	1850
Iodide (I <sup>-</sup> )	29.6
Bicarbonate (HCO <sub>3</sub> <sup>-</sup> )	174.5
Sulfate (SO <sub>4</sub> <sup>2-</sup> )	50.3

\*Data obtained from Canbriam Energy Inc., Calgary, Alberta, Canada

#### 4.3.6 Pre-treatment of the fracking wastewater

The synthetic fracking wastewater was retained for 2 h to sediment the suspended solids to the bottom of the container. Afterward, the water was decanted to another container and this water was then microfiltered through a commercial microfiltration membrane (Mean pore size 0.2  $\mu\text{m}$ , HT-200, Pall Corporation, USA) in a dead-end stirred cell filtration device (Millipore stirred ultra-filtration cells, 8010, USA, effective area of 0.0003  $\text{m}^2$ ) connected to a nitrogen gas cylinder. The membrane was pre-compacted at an applied pressure of 4 psi using DI water until a constant water flux was achieved and then the microfiltration process for the fracking wastewater as a feed was conducted for 12 h at a stirring rate and applied pressure of 500 rpm and 4 psi, respectively. Turbidity, conductivity, and pH of the fracking wastewater immediately after preparation, after sedimentation, and after microfiltration were investigated using a MicroTPW Turbidimeter (HF, Scientific, Inc., USA), a calibrated conductivity meter (Oakton, Eutech Instruments), and a calibrated pH meter (Oakton, Eutech Instruments), respectively. Total organic carbon of the fracking wastewater after sedimentation and after microfiltration were determined using a TOC analyzer (TOC V<sub>CPH/CPN</sub>, Shimadzu Corp., Japan). The true fracking wastewater was more clear than the synthetic fracking wastewater and, therefore, the sedimentation step was skipped for the true fracking wastewater. However, microfiltration was conducted for this wastewater using the same experimental condition as for synthetic fracking wastewater. Turbidity, TOC, conductivity, and pH were measured after sample collection and after microfiltration of the true fracking wastewater. The osmotic pressure of the fracking wastewaters after microfiltration was also investigated as the following way. The van Laar equation (4-8) was used to calculate the osmotic pressure of the fracking wastewater [144-145]:

$$\pi_{\text{o.p.f}} = - \left( \frac{R_i T}{V_0} \right) \ln a_1 \quad (4-8)$$

where  $\pi_{\text{o.p.f}}$  is the osmotic pressure,  $R_i$  is the ideal gas constant,  $T$  is the absolute temperature,  $V_0$  is the molar volume of solvent and  $a_1$  is the water activity.

The water activity was calculated using the following equation (4-9) [144, 146-147]:

$$a_1 = \frac{P}{P_0} \quad (4-9)$$

where  $P$  and  $P_0$  are the vapor pressures of the fracking wastewater and DI water, respectively, at 24 °C. The vapor pressures of the fracking wastewater and DI water were investigated using a U-Tube Manometer (Tenaquip, Canada).

#### 4.3.7 Desalination of fracking wastewater

A bench-scale experimental FO setup (Figure 2-6) was used to desalinate fracking wastewater using a commercial TFC membrane (Hydration Technology Innovations, HTI, Albany, OR). A piece of the membrane with an effective surface area of 19.94 cm<sup>2</sup> was placed in an acrylic cross-flow cell with the active layer of the membrane facing the feed solution. The fracking wastewaters (synthetic and true) and the identified organic compounds were used as the feed and draw solutions (KAc 4.47 M, KF 4.57 M, NaGly 4.93 M, NaP 4.60 M), respectively, in the FO experiment. NaCl (4.03 M) was also used as a draw solution for desalination of fracking wastewater in the FO experiment. On both sides of the membrane, the cross-flow cell had symmetric channels, which allowed for both the feed solution and the draw solution to flow tangentially to the membrane. Re-circulation of the feed solution and the draw solution on opposite sides of the membrane was executed using two variable-speed gear pumps (Gear Pump Drive, Cole-Parmer Instrument Company). The flow rate of each solution was maintained at 0.5 L/min. The feed solution temperature and the draw solution temperature were held constant at 24°C and monitored with a thermometer. The feed solution and the draw solution were placed in two separate 4.0 L reservoirs to conduct the experiment. The feed solution container was placed on a digital analytical balance. Each experiment was conducted for six hours and the concentration of the draw solution was adjusted by adding concentrated draw solution in every 15 min. The water flux of the draw solution was obtained from the digital analytical balance by using equation (4-1). Samples of the feed and draw solutions at the beginning and after the FO experiment were collected in order to investigate total dissolved solids (TDS) and TOC. Gravimetric method was used to determine TDS while a TOC analyzer (TOC V<sub>CPH/CPN</sub>, Shimadzu Corp., Japan) was used to examine TOC of the feed and draw solutions [148-149].

## 4.4 Results and discussion

### 4.4.1 FO water flux and structural parameter of the membrane

A cross-flow RO cell was used to investigate pure water permeability of the commercial TFC membrane (pure water permeability 32.5 LMH/MPa). This obtained water permeability value was very close to the value in the literature (31.6 LMH/MPa) for the same type of membrane [150]. The structural parameters of the membrane for all draw solutions were determined through the investigation of salt rejection and salt permeability coefficient in a cross-flow RO cell (Table 4-3). The salt rejection for the organic draw solutions was 99.43 – 99.58%, whereas it was 97.27% for NaCl. The salt permeability coefficient of the organic draw solutions was 0.249 – 0.340 LMH, which was much lower than that of the NaCl draw solution (1.65 LMH). Higher salt rejection and lower salt permeability coefficients were obtained for the organic draw solutions due to the larger sizes of their hydrated ions as compared to that of the NaCl draw solution. FO water fluxes for the draw solutions at 2.8 MPa osmotic pressure against DI water are presented in Table 4-3. The obtained FO water fluxes for the organic draw solutions were higher (15.48 to 19.71 LMH) than that of the NaCl draw solution (12.70 LMH) under the same experimental conditions. Higher FO water fluxes were obtained for the organic draw solutions due to the much lower salt permeability that caused lower concentration polarization and the much lower membrane structural parameter as compared to those of NaCl (Table 4-3). The FO water flux for the NaCl draw solution using the same type of membrane is comparable with the value from the literature (~ 18 LMH at 1M NaCl) [150]. In the experiment, the concentration of the NaCl draw solution was less (0.61 M NaCl solution) than that used in the literature [150]. Hence, the water flux obtained in our experiment for the NaCl draw solution was lower as compared to the value from the literature [150]. The structural parameters of the membrane for the organic draw solutions ranged from 404 to 468  $\mu\text{m}$ , much lower than the value for the NaCl draw solution (729  $\mu\text{m}$ ). The performances of the identified organic draw solutions were not compared to another commonly used draw solution  $\text{NH}_4\text{HCO}_3$  due to its lower osmotic pressure than that of the fracking wastewater (Table B-1, Appendix B and Table 4-5) .

Table 4-3. FO water flux (at 2.8 MPa osmotic pressure of the draw solutions against DI water as feed) and structural parameters of the membrane.

Draw solutions	Conc. (mM)	Osmotic pressure (MPa)	R (%)	B (LMH)	FO water flux (LMH)	S ( $\mu\text{m}$ )
KAc	20	0.08	99.58	0.249	15.48	404
NH <sub>4</sub> Ac		0.04	99.56	0.266	15.86	454
NH <sub>4</sub> C		0.15	99.55	0.257	16.56	460
NH <sub>4</sub> F		0.09	99.45	0.324	16.92	468
KF		0.08	99.43	0.340	17.15	468
NaGly		0.08	99.52	0.285	18.47	450
NaP		0.08	99.51	0.291	19.71	456
NaCl		0.09	97.27	1.65	12.70	729

\* Applied pressure for rejection test and pure water permeability in RO experiments were 1.896 MPa, 32.5 LMH/MPa, respectively.

#### 4.4.2 Reverse salt flux and specific reverse salt flux of the draw solutions

The reverse salt fluxes and specific reverse salt fluxes of the draw solutions at 2.8 MPa osmotic pressure in the FO process are shown in Figure 4-2. The reverse salt fluxes of the organic draw solutions ranged from 0.021 to 0.04 mol m<sup>-2</sup> h<sup>-1</sup> (Figure 4-2 A). In membrane-based osmotic processes, reverse salt flux is substantially influenced by the diffusivity of the draw solutions, in which a higher reverse salt flux is obtained for draw solutions with higher diffusivity values [151]. For our selected organic draw solutions, a higher reverse salt flux was obtained for draw solutions with higher mutual diffusivity (Table 4-1 and Figure 4-2 A) without considering the draw solutions NH<sub>4</sub>F and KF. Both the mutual diffusivity and hydrated anion sizes could affect the reverse salt flux for these two draw solutions. Actually, the draw solutions with higher diffusivity values demonstrated a higher driving force that facilitated the draw solute passing through the membrane. Compared to the commonly used inorganic draw solution (NaCl), the reverse salt fluxes of the selected organic draw solutions were much lower under the same experimental conditions (Figure 4-2 A). The reverse salt flux of the NaCl draw solution was 0.15 mol m<sup>-2</sup> h<sup>-1</sup>. The reverse salt flux for the NaCl draw solution is comparable with the literature values (0.17 mol m<sup>-2</sup> h<sup>-1</sup> at 1 M NaCl draw solution against DI water used as feed) when using the same type of membrane [150]. The reverse salt flux for this draw solution was lower as compared to the value in the literature because of the lower concentration of NaCl solution (0.61 M) used in this experiment. In fact, the draw solutions containing larger-sized

hydrated anions showed lower reverse salt flux [132]. All of the anions of the organic draw solutes contain a C-O double bond, which can be polarized (especially  $\pi$ -bond of the double bond) in their aqueous solutions (Figure 4-2 B). This polarizing nature promoted hydration of the organic draw solutes with a larger number of water molecules as compared to the chloride ion. Therefore, the sizes of the hydrated anions of organic draw solutes were larger than that of  $\text{Cl}^-$  ions. Moreover, the much higher salt permeability of the NaCl draw solution in the RO test (Table 4-3) supports its higher reverse salt flux as compared to the selected organic draw solutions in the FO test.

The lowest specific reverse salt flux value (reverse salt flux/water flux) indicates the best draw solution performance in the FO process [132]. The low specific reverse salt flux value is obtained due to a low reverse salt flux with a high water flux for a draw solution. The obtained specific reverse salt flux for the identified organic draw solutions were  $1.36 \times 10^{-3}$  to  $2.33 \times 10^{-3} \text{ mol L}^{-1}$ , which were much lower than that of NaCl ( $12 \times 10^{-3} \text{ mol L}^{-1}$ ) at the same experimental conditions (Figure 4-2 C). The much lower specific reverse salt flux values were obtained due to much lower reverse salt fluxes with high water fluxes for the organic draw solutions compared to NaCl. The highest values of specific reverse salt fluxes were obtained for  $\text{NH}_4\text{F}$  ( $2.25 \times 10^{-3} \text{ mol L}^{-1}$ ) and  $\text{KF}$  ( $2.33 \times 10^{-3} \text{ mol L}^{-1}$ ) draw solutions due to their having the highest values of reverse salt flux among the identified organic draw solutions.

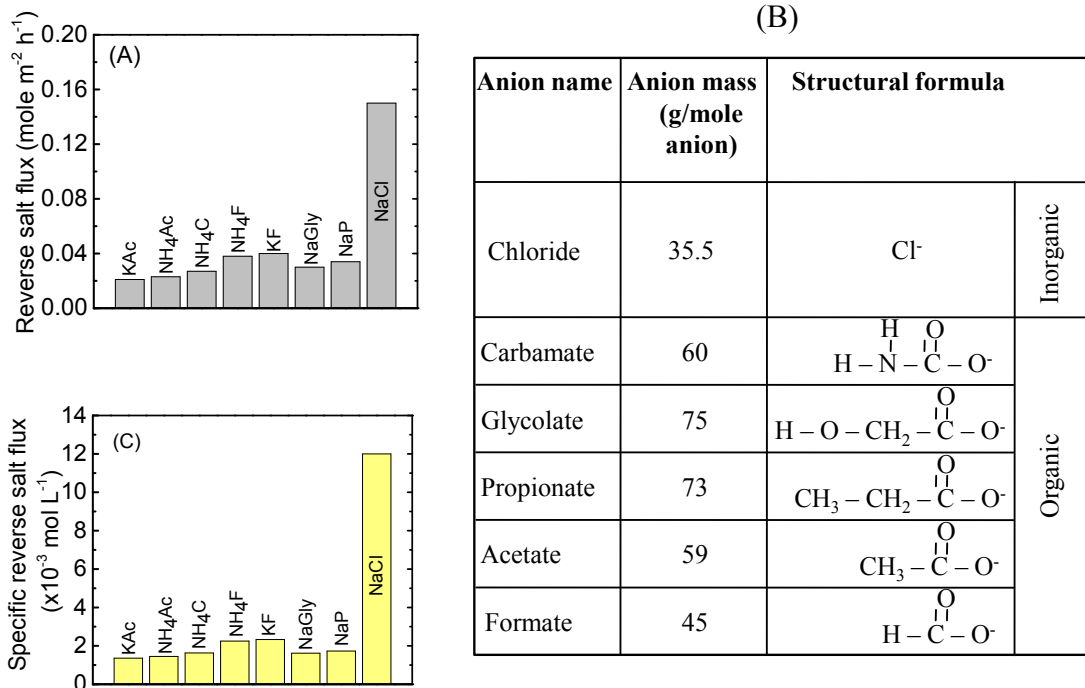


Figure 4-2. (A) Reverse salt flux, (B) Structural formula of anion and (C) Specific reverse salt flux of the draw solutions.

#### 4.4.3 Compatibility of the organic draw solutions with the commercial TFC membrane

Compatibility of the draw solution with the membrane is an important issue in the selection of a draw solution for an osmotic process. If a draw solution reacts with the membrane, the performance of the membrane can decline. For this reason, the compatibility of the selected organic draw solutions with the commercial TFC membrane was tested through the investigation of pure water permeability and salt permeability of the membrane. In a cross-flow RO cell, the pure water permeability and salt permeability of the TFC membrane was investigated before and after conducting FO experiments using the individual organic draw solutions. The water permeability of the TFC membrane before conducting FO experiments was 32.5 LMH/MPa. The water permeability of the TFC membrane after conducting FO experiments with each organic draw solution was consistent at a value of 32.5 LMH/MPa (Figure 4-3 A). The salt permeability of the TFC membrane before and after conducting the FO experiments with each organic draw solution was also consistent, and it is presented in Figure

4-3 B. These results demonstrated that the commercial TFC membrane was compatible with the selected organic draw solutions.

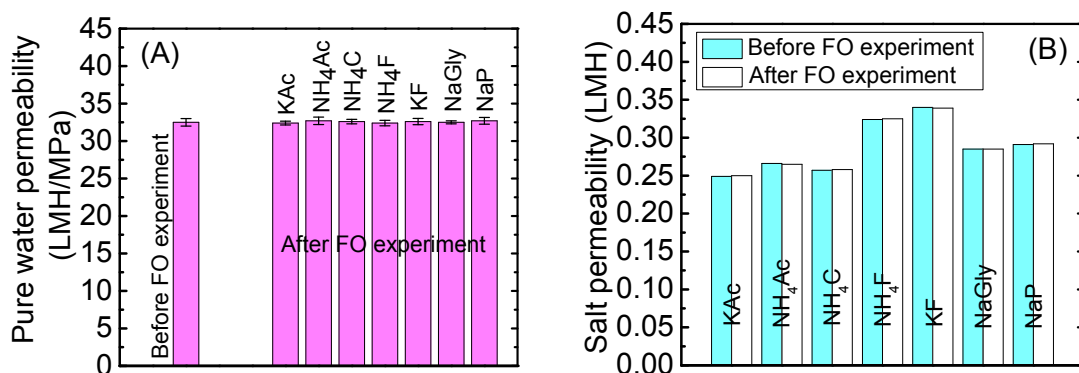


Figure 4-3. (A) Pure water permeability and (B) salt permeability of the membrane before and after FO experiment with each organic draw solution.

#### 4.4.4 Studies into the recovery of the organic draw solutes downstream in the FO process

A laboratory investigation was conducted to distinguish the organic draw solutes as distillable or thermolytic through the gravimetric method. In this method,  $W_1$  g of a draw solute was dissolved in DI water. The solution was then heated to 50°C to evaporate all water and the residue was weighed again ( $W_2$  g). Finally; the osmotic pressure of the residue (when  $W_1 = W_2$ ) at the same concentration of the draw solute was investigated. The values of  $W_1$  and  $W_2$  were consistent for the draw solutes of KAc, KF, NaGly, and NaP (Table 4-4). Moreover, the osmotic pressures of the draw solute and the corresponding residue at the same concentration were similar for these draw solutes (Table 4-4) (Conversions of osmolality to osmotic pressure for the distillable organic draw solutes are provided in Table B-2, Appendix B). These results revealed distillable properties of these draw solutes. However,  $W_1$  values were higher than that of  $W_2$  for the draw solutes of NH<sub>4</sub>Ac, NH<sub>4</sub>C, and NH<sub>4</sub>F, which demonstrated thermolytic properties of these three draw solutes (Table 4-4). Ammonium acetate decomposed into acetamide (solid) and water under applied heat [152]. Presumably, ammonium carbamate decomposed into ammonia and carbon dioxide gases at 50°C. Formamide (liquid) and water were produced by the decomposition reaction of ammonium formate under applied heat [153].

Table 4-4. A list of the organic draw solutes as thermolytic and distillable at 50°C.

Draw solute	Conc. (M)	Relation between $W_1$ and $W_2$	Osmotic pressure (MPa)		Type
			Pristine	Residue	
KAc	0.66	$W_1 = W_2$	2.80	2.80	Distillable
NH <sub>4</sub> Ac	0.91	$W_1 > W_2$	2.80	Residue obtained	Thermolytic
NH <sub>4</sub> C	0.38	$W_1 > W_2$	2.80	No residue	Thermolytic
NH <sub>4</sub> F	0.62	$W_1 > W_2$	2.80	No residue	Thermolytic
KF	0.68	$W_1 = W_2$	2.80	2.79	Distillable
NaGly	0.73	$W_1 = W_2$	2.80	2.80	Distillable
NaP	0.69	$W_1 = W_2$	2.80	2.79	Distillable

As it is demonstrated in literatures that membrane distillation and thermal distillation processes can be applied to recover distillable and thermolytic draw solutes, respectively, used in FO process [129-130]. Therefore, it can be said that the identified distillable draw solutes (KAc, KF, NaGly, and NaP) could be recovered from the solution by using the membrane distillation technique downstream of the FO process. The thermolytic draw solutes (ammonium acetate, ammonium carbamate and ammonium formate) can decompose under applied heat, however, these draw solutes cannot be regenerated from their decomposition products. Therefore, considering recyclability, the potential organic draw solutions for treatment of fracking wastewater in FO process are KF, KAc, NaGly, and NaP.

#### 4.4.5 Characteristics of the fracking wastewater before and after pre-treatment

The turbidity, conductivity, and pH of the synthetic fracking wastewater were >1100 NTU, ~98 mS, and ~4.2, respectively, immediately after preparation of the wastewater (Table 4-5). The turbidity reduced to 148 NTU after sedimentation for 2 h with almost identical conductivity and pH values as the values right after preparation. Mostly, the sand particles were suspended at the bottom of the container during the sedimentation period. The turbidity value of 148 NTU was obtained due to the presence of colloidal oil in the wastewater. At this stage, TOC of the synthetic fracking wastewater was 1194 ppm. Afterward, microfiltration (MF) through the commercial microfiltration membrane was conducted for this wastewater. The turbidity and TOC decreased significantly after conducting MF of the wastewater. The obtained turbidity and TOC after MF were 4 NTU and 599 ppm, respectively, but conductivity and pH values were the same as the values after sedimentation. The osmotic pressure of the synthetic fracking wastewater after microfiltration was 15.68 MPa (Table 4-5). The real fracking

wastewater was sand particles free because the water sample was collected from the top of the sample collection point in which the sand particles were suspended. The turbidity, TOC, conductivity, and pH of the real fracking wastewater were 106 NTU, 853 ppm, ~ 67 mS, and ~ 4.9, respectively, after collection of this water sample (Table 4-5). The turbidity and TOC reduced to 2 NTU and 413 ppm, respectively, after conducting MF for this wastewater. The osmotic pressure obtained for the real fracking wastewater after MF was 12.83 MPa. Compared to the synthetic fracking wastewater, the conductivity and osmotic pressure of the real fracking wastewater were relatively lower due to its lower concentration of TDS (Table 4-6).

Table 4-5. Characteristics of fracking wastewaters.

Water type	Condition	Turbidity (NTU)	TOC (ppm)	Conductivity (mS)	pH	Osmotic pressure (MPa) after MF
Synthetic fracking wastewater	Right after preparation	>1100	-	~ 98	~ 4.2	15.68
	After sedimentation for 2 h	148	1194			
	After MF	4	599			
Real fracking wastewater	After collection	106	853	~ 67	~ 4.9	12.83
	After MF	2	413			

#### 4.4.6 FO performance in desalination of fracking wastewaters

##### 4.4.6.1 Water flux

The final four organic draw solutions (KAc, KF, NaGly, and NaP) at 18.48 MPa osmotic pressure were used for desalination of the fracking wastewaters. The osmotic pressures of the fracking wastewaters (feed solutions) ready for the FO process were 15.68 MPa for the synthetic solution and 12.83 MPa for the true solution. The initial water fluxes (in 2 min) for synthetic fracking wastewater ranged from 11.15 to 14.19 LMH (Figure 4-4 A), while those values were from 19.51 to 24.83 LMH for the real fracking wastewater (Figure 4-4 B). NaCl is a commonly used draw solution for desalination of fracking wastewater by FO process [154-155]. The initial water fluxes were lower (9.14 LMH for synthetic fracking wastewater and 16.0 LMH for real fracking wastewater) for the commonly used draw solution (NaCl) as compared to the identified organic draw solutions at the same osmotic pressure (Figure 4-4 A

and Figure 4-4 B). The reverse salt fluxes and membrane structural parameters for the organic draw solutions were much lower as compared to NaCl (Table 4-3 and Figure 4-2 A), demonstrating the higher initial water fluxes for the organic draw solutions. The higher water fluxes in the desalination of true fracking wastewater were obtained due to higher osmotic pressure differences between the draw and feed solutions (5.65 MPa) as compared to that of synthetic fracking wastewater (2.8 MPa) (Figure 4-4 A and Figure 4-4 B). Due to membrane fouling, water fluxes decreased by 17% and 9% over 6 h for synthetic and real fracking wastewaters, respectively, in case of the organic draw solutions. The higher decline in water flux was obtained due to higher membrane fouling caused by higher dissolved organic compounds in the synthetic wastewater as compared to the true wastewater. In addition, the synthetic wastewater contains higher concentration of  $\text{Ca}^{2+}$ ,  $\text{SO}_4^{2-}$  and  $\text{CO}_3^{2-}$  ions which caused higher membrane fouling as compared to the true fracking wastewater. Generally,  $\text{Mg}^{2+}$  and  $\text{Ca}^{2+}$  ions in water can cause membrane fouling by scale formation of  $\text{MgCO}_3$ ,  $\text{MgSO}_4$ ,  $\text{CaCO}_3$  and  $\text{CaSO}_4$  [156-157]. Figure 4-4 also demonstrated that water flux declined by 27% for synthetic wastewater and by 24% for true wastewater with the NaCl draw solution. Normalized water flux decline in FO desalination of fracking wastewaters for all these draw solutions are exhibited in Figure 4-4 C and Figure 4-4 D. Compared to the organic draw solutions, the higher decline of water flux for NaCl draw solution was obtained due to the combined effect of membrane fouling and higher concentration polarization because of higher reverse salt flux for this draw solution. The average water fluxes achieved over 6 h were 10.50 to 13.26 LMH for the synthetic wastewater (Figure 4-4 E), whereas those values were 19.05 to 24.05 LMH for the real wastewater (Figure 4-4 F). The average water fluxes obtained for NaCl draw solution were 8.25 LMH for synthetic wastewater and 14.44 LMH for real wastewater (Figure 4-4 E and Figure 4-4 F).

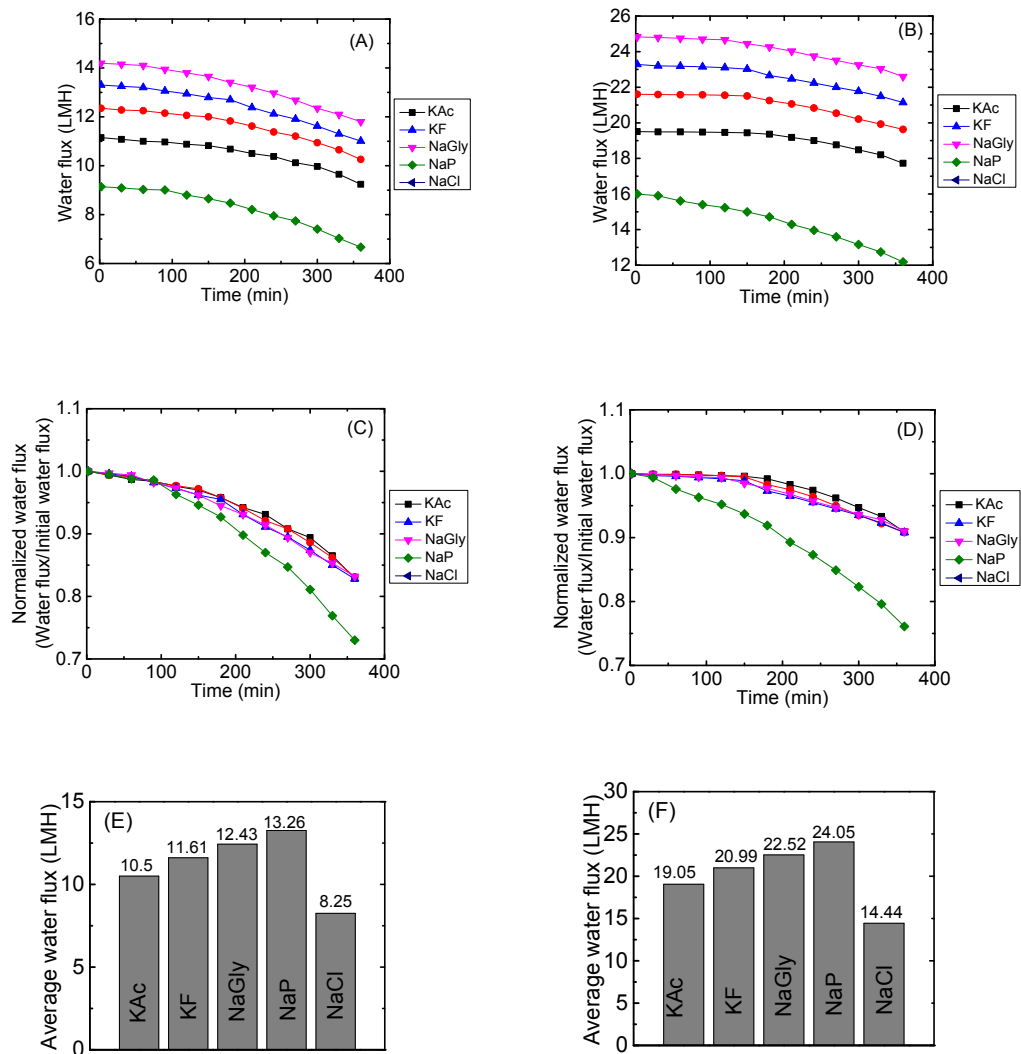


Figure 4-4. Water flux as a function of time for (A) synthetic and (B) real fracking wastewaters, normalized water flux as a function of time for (C) synthetic and (D) real fracking wastewaters, and average water fluxes over 6 h for (E) synthetic and (F) real fracking wastewaters. [Fracking wastewaters as feed, and KAc, KF, NaGly, NaP and NaCl as draw solutions at an osmotic pressure of 18.48 MPa in FO process; Each set of experiments was conducted thrice and then the average values of obtained data from these three sets of experiments are presented in Figure 4-4].

#### 4.4.6.2 Compositions of feed and draw solutions

The compositions in terms of TDS and TOC of fracking wastewaters as well as draw solutions were investigated before and after desalination (Table 4-6). The TDS values of feed solutions were little bit higher before desalination compared to those values of after desalination when the organic compounds were used as draw solutions. The TDS values of the organic draw solutions were little bit higher after desalination compared to those values of before desalination. These observations indicated that a very small quantity of solutes might pass through the membrane from feed to draw side during desalination. On the other hand, TDS values of feed solutions were little bit lower before desalination compared to those values of after desalination when NaCl were used as draw solution. TDS values of NaCl draw solution were little bit lower after desalination compared to those values of before desalination. These scenarios might happen due to higher reverse salt flux for this draw solution as compared to the organic draw solutions. The TOC values of feed solutions were little bit higher after desalination compared to those values of before desalination for the organic draw solutions. The higher TOC values were obtained due to probably reverse salt flux of organic draw solutions during FO process. However, TOC values were almost the same as before and after desalination for NaCl draw solution indicating above 99% rejection of dissolved organic compounds in fracking wastewaters.

Table 4-6. TDS and TOC in the feed and draw solutions at the beginning and end of the FO experiment.

Fracking wastewater as Feed solution	Draw solution	TDS (mg/L) in feed solution		TOC (mg/L) in feed solution		TDS (mg/L) in draw solution		TOC (mg/L) in draw solution	
		Beginning of FO test	End of FO test	Beginning of FO test	End of FO test	Beginning of FO test	End of FO test	Beginning of FO test	End of FO test
Synthetic	KAc	228706	227656	599	656	438685	439500	107280	107217
	KF		227554		646	384428	385248	54840	54789
	NaGly		227710		667	488218	488932	118320	118245
	NaP		227542		712	441876	442737	165600	165490
	NaCl		228818		597	235755	235622	0	0.8
Real	KAc	178580	177530	413	460	438685	439540	107280	107228
	KF		177460		454	384428	385256	54840	54795
	NaGly		177530		472	488218	489026	118320	118265
	NaP		177473		510	441876	442720	165600	165498
	NaCl		178744		412	235755	235561	0	0.5

## 4.5 Conclusions

A successful database-driven screening method followed by a comprehensive laboratory investigation was conducted to select effective organic draw solutions for the desalination of highly saline fracking wastewaters by FO process. Four different organic compounds, namely KAc, KF, NaGly, and NaP were obtained as effective draw solutions for the desalination of this particular wastewater. The average water fluxes obtained in 6 h ranged from 10.50 to 13.26 LMH for the synthetic fracking wastewater and those values were 19.05 to 24.05 LMH for the real fracking wastewater with high solute rejection using the selected organic draw solutions (at 18.48 MPa osmotic pressure) in FO processes. The specific reverse salt fluxes were much lower for the identified organic draw solutions as compared to the commonly used FO process draw solution (NaCl). The lower specific reverse salt flux values were obtained due to a low reverse salt flux with a high water flux for the organic draw solutions, as compared to when NaCl was used as draw solution. The identified draw solutions showed much higher osmotic pressures than those of fracking wastewaters. The selected organic draw solutions were also tested for potential recovery downstream in the FO process. The laboratory investigation revealed that the membrane distillation is a potential recovery method to reuse these draw solutions in the FO process. Hence the identified draw solutes have huge potential to be used in FO for treating high salinity waste streams such as fracking wastewater.

## Acknowledgements

Md. Saifur Rahaman gratefully acknowledges the FRQNT for providing the funding support for this project. Md. Shahidul Islam acknowledges the support of a doctoral-level scholarship from the FRQNT. The authors also acknowledge supports from the NSERC and Concordia University, Canada.

## **Chapter 5: Silica Nanoparticle Containing Novel Thin-Film Composite Forward Osmosis Membrane with High Flux and Antifouling Properties**

### **Abstract**

A novel high flux and antifouling thin-film composite forward osmosis membrane containing silica nanoparticles was fabricated using a facile electrospinning technique followed by interfacial polymerization on the surface of electrospun nanofiber mat. Both the electrospun nylon 6 substrate and the polyamide (PA) active layer contained superhydrophilic SiO<sub>2</sub> nanoparticles enhancing the hydrophilicity of the fabricated FO membrane. The fabricated electrospun N6/SiO<sub>2</sub>-supported TFC FO membrane with a PA/SiO<sub>2</sub> composite active layer (E.Spun N6/SiO<sub>2</sub>-PA/SiO<sub>2</sub>) was robust (tensile strength of 22.3 MPa) with a water contact angle of 14°. In the FO process, the fabricated TFC membrane exhibited a high water flux (27.10 LMH) with a low specific reverse salt flux ( $5.9 \times 10^{-3} \text{ mol.L}^{-1}$ ). The fabricated membrane also showed antifouling tendencies in FO process for the model foulants of sodium alginate and calcium sulfate. The initial water flux recovery for this membrane was 98% for sodium alginate and 94% for calcium sulfate. Moreover, a strong interaction between the electrospun substrate and the active layer demonstrated the structural stability of the fabricated TFC membrane.

**Keywords:** Electrospinning; Nylon 6/SiO<sub>2</sub> substrate; Polyamide/SiO<sub>2</sub> active layer; TFC FO membrane

## 5.1 Introduction

Forward osmosis processes have attracted a great deal of interest as an alternative to conventional pressure-driven membrane processes for applications in food processing, desalination, wastewater treatment, and clean energy generation [158-161]. The primary concept underlying this process is the osmotic transport of water (water flux) through a semi-permeable membrane from a low salinity feed solution into a high salinity draw solution due to the osmotic pressure gradient between these two solutions [122-123]. This exploits the natural process of osmosis, which is the diffusion of salt due to different salinities on either side of a semi-permeable membrane. An ideal membrane for the forward osmosis process is one which demonstrates high water permeability, solute rejection, and chemical and mechanical stability with a low propensity toward fouling [162-163]. Cellulose triacetate (CTA), a hydrophilic and low cost organic compound [51], is currently used in the fabrication of a commonly used single layer membrane for forward osmosis [164-166]. However, serious disadvantages of this forward osmosis membrane include its low selectivity and low stability in harsh acidic and basic conditions [167]. These obstacles have redirected researchers' attention to fabrication of TFC PA membranes [143, 166-168] instead of single layer CTA membranes for the forward osmosis process. A typical TFC forward osmosis membrane is composed of a microporous substrate and an active layer (~ 100 to 300 nm thick) attached on the top surface of the substrate [143,166-170]. The active layer of the TFC membrane is polyamide, which is formed by an interfacial polymerization reaction on the top surface of the substrate [143,166-170]. Materials such as polysulfone, polyether sulfone, and nylon with high tensile strength and highly resistant to abrasion and chemicals are used to fabricate the substrate by a phase inversion method and/or electrospinning technique [171-173]. TFC membranes are well established in pressure-driven membrane processes such as reverse osmosis and nanofiltration, however, the application of this type of membrane is still at early stages of adoption in the forward osmosis process [174]. TFC membranes currently available for forward osmosis have performance drawbacks like low water flux and propensity towards fouling due to the hydrophobic substrate with low porosity and hydrophobic active layer [175-177].

Electrospun nanofiber mats have distinctive structural characteristics, such as a high surface area-to-volume ratio, interconnected openpores, and high porosity, which make them highly suitable for filtration applications [66-69, 178]. N6 is a synthetic polymer that can be used to

fabricate electrospun nanofiber mats [82,178-179]. The fabricated electrospun N6 nanofiber mats can be applied as a suitable material for water filtration membranes because of their high mechanical strength, high resistance to abrasion and chemicals, extensive surface area, and high porosity [82,178-179]. The incorporation of SiO<sub>2</sub> nanoparticles into the polymer renders the composite (polymer/SiO<sub>2</sub>) hydrophilic due to the superhydrophilic property of the SiO<sub>2</sub> nanoparticles [83,178]. In addition, the combination of porous SiO<sub>2</sub>, along with the integrated network structures renders a composite material with higher porosity and mechanical strength [84-85,178]. Analyzing the above items, the superhydrophilic SiO<sub>2</sub> nanoparticles (size: less than fiber diameter and thickness of active layer) can be incorporated into the electrospun N6 substrate as well as the PA active layer (obtained by interfacial polymerization) to enhance the performance of the TFC forward osmosis membrane. In fact, the hydrophilicity of both the substrate and active layer, and the TFC forward osmosis membrane substrate porosity can be increased by inclusion of SiO<sub>2</sub> nanoparticles. However, non-selective voids at the interface of the active layer and nanoparticles can be generated due to non-uniform dispersion/aggregation of nanoparticles that can reduce solute rejection [180-181]. For this reason, nanoparticle content optimization is essential in order to incorporate them successfully into the active layer of the TFC membrane.

Development of a TFC membrane with high water flux and rejection, antifouling properties, and desirable mechanical strength is crucial for successful application in the forward osmosis process. The study presented here focuses on the preparation of a novel electrospun N6/SiO<sub>2</sub> composite nanofiber mat supported PA/SiO<sub>2</sub> composite (as active layer) TFC membrane with high flux and antifouling propensity in FO process. The incorporation of superhydrophilic SiO<sub>2</sub> nanoparticles into both the substrate and the active layer increased membrane hydrophilicity, and substrate porosity. A highly porous substrate together with highly hydrophilic properties was responsible to achieve high water flux with antifouling propensity for the fabricated TFC membrane. High mechanical strength was also obtained due to the interconnected spider-web like structure of the electrospun N6 nanofiber mat along with incorporation of integrated network structure SiO<sub>2</sub> nanoparticles into the N6 nanofiber mat.

## 5.2 Experimental

### 5.2.1 Materials

Nylon 6, TEOS, ethyl alcohol ( $C_2H_5OH$ ), ammonium hydroxide ( $NH_4OH$ ), m-phenylenediamine (MPD), 1, 3, 5- benzenetricarbonyl trichloride (TMC), and hexane were obtained from Sigma-Aldrich, USA. Both formic acid and acetic acid were acquired from Fisher Scientific, USA. The commercial flat-sheet TFC forward osmosis membrane was purchased from Hydration Technology Innovations (HTI, Albany, OR, USA). De-ionized (DI) water was obtained from a Millipore Integral 10 water system (Millipore, Billerica, MA).

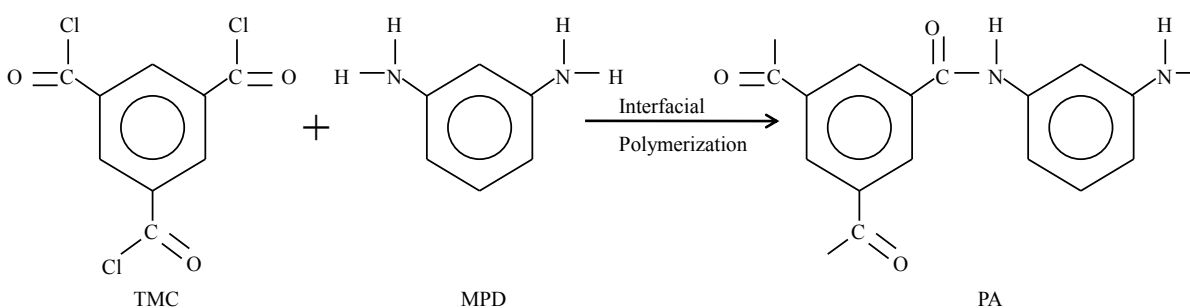
### 5.2.2 Fabrication of TFC membrane

#### 5.2.2.1 Fabrication of N6/SiO<sub>2</sub> composite nanofiber substrate by electrospinning technique

N6 (21% by weight) was dissolved in a mixture of formic and acetic acids (80% formic acid and 20% acetic acid by volume) using magnetic stirring (rpm 350) for 5 h at ambient room temperature. Separately, a SiO<sub>2</sub> solution was prepared by mixing TEOS, ethanol, and water at a molar ratio of 1:2:2, respectively, in the presence of an  $NH_4OH$  catalyst and stirred at 25°C for 4 h. SiO<sub>2</sub> nanoparticles were then separated from the mixture through centrifugation. Subsequently, SiO<sub>2</sub> nanoparticles were dispersed in a formic acid (80% by volume) and acetic acid (20% by volume) mixture under sonication for 20 min. An appropriate ratio of SiO<sub>2</sub> dispersion was added to the N6 solution and sonicated for 5 min and then stirred for 5 h at ambient conditions to make the N6/SiO<sub>2</sub> solution. In the electrospinning process, high-voltage electricity (Nanospinner NE300, Inovenso, Turkey) was applied to the prepared N6/SiO<sub>2</sub> solution in a syringe (volume 20 mL, inside diameter 19.05 mm) via an alligator clip attached to the syringe nozzle. The applied voltage was adjusted to 30 kV. The solution was delivered to the nozzle tip via a syringe pump to control the solution flow rate (0.18 mL/h). Fiber mats were collected on an electrically grounded metallic drum placed 8.8 cm above the nozzle tip [64-65]. N6 solution without SiO<sub>2</sub> nanoparticles was also electrospun to fabricate a pristine N6 nanofiber mat as a substrate of the TFC membrane. Temperature (25°C) and relative humidity (40%) were controlled throughout the fabrication process.

### 5.2.2.2 Formation of PA/SiO<sub>2</sub> composite active layer on the substrate

An active layer of PA/SiO<sub>2</sub> nanoparticle composite was formed on the electrospun N6/SiO<sub>2</sub> substrate by an interfacial polymerization reaction. First, the electrospun substrate was put on a glass plate and then the each side of the substrate was tapped with the glass plate very well. The electrospun substrate with the glass plate was immersed in an aqueous MPD/SiO<sub>2</sub> solution (1% MPD and 1, 2, 4 and 6% SiO<sub>2</sub> with respect to MPD) for 2 min. Excess MPD solution was removed from the substrate surface using an air knife. The MPD/SiO<sub>2</sub> substrate was then dipped into a solution of 0.15 wt% TMC in hexane for 1 min (to form an ultrathin PA/SiO<sub>2</sub> composite as active layer by an interfacial polymerization reaction between MPD and TMC) followed by removal of the excess TMC solution from the top surface of the substrate using an air knife. The electrospun substrate with the PA/SiO<sub>2</sub> composite active layer was then heated at ~ 75°C in an oven for 10 min to complete internal cross-linking of the remaining un-reacted precursors of interfacial polymerization reaction [182-184]. Finally, the prepared TFC membrane was stored in DI water until it was tested. A polyamide active layer was also fabricated on the electrospun N6/SiO<sub>2</sub> substrate without adding SiO<sub>2</sub> nanoparticles during the interfacial polymerization reaction between MPD and TMC. Polyamide and polyamide/SiO<sub>2</sub> composite (4% SiO<sub>2</sub> content as regards MPD) active layers were fabricated on the electrospun N6 substrate as well. A schematic representation of interfacial polymerization between MPD and TMC is exhibited in the Scheme 5.1.



Scheme 5.1. A schematic representation of interfacial polymerization between MPD and TMC.

### 5.2.3 Fabrication of N6 substrate by casting and phase inversion method

Pristine N6 substrate was also prepared by a casting and phase inversion method. A 21% N6 solution (by weight) in 80% formic acid and 20% acetic acid mixture (by volume) was casted manually on a clean glass plate using a casting knife with the thickness of 85  $\mu\text{m}$  at ambient

condition. After casting, the film was dried for 24 h at ambient condition and then it was peeled from the glass plate. Finally, the film was immersed into DI water for another 24 h in order to remove the remaining solvent.

#### 5.2.4 Physicochemical characterization

FE-SEM (QUANTA FEG 450) with a platinum coating on the sample surface was performed to observe the morphology of the substrates and TFC membranes. Cross-sectional morphology and thickness of the TFC membrane were measured using FE-SEM and a TMI instrument (Testing Machines, Inc.), respectively [178]. TEM (TF20) was conducted to examine the morphology of the electrospun substrates. A structural study of the electrospun substrates was conducted via the use of XRD (Bruker D8 Discover with a copper X-ray source and equipped with a Vantec area detector), and FTIR (NICOLET 6700 FT-IR) spectrometry. The wettability and surface roughness of both the substrates and TFC membrane were investigated using a VCA optima instrument (AST Products, Inc.), and an AFM (BRUKER, NanoScope<sup>RV</sup>), respectively. The wettability of SiO<sub>2</sub> nanoparticles was also investigated using the VCA optima instrument (AST Products, Inc.). The analysis was performed using the same protocol for SiO<sub>2</sub> nanoparticles described elsewhere [93,178]. Briefly, a few drops of SiO<sub>2</sub> nanoparticle suspension, in ethanol, were placed on a glass slide and then dried in an oven at 80°C for 30 min followed by cooling the SiO<sub>2</sub> nanoparticles on the glass slide at room temperature. Then, the VCA optima instrument was used to determine the water contact angle of the SiO<sub>2</sub> nanoparticles placed on the glass slide. The tensile strength of the substrates and TFC membrane were investigated using an Instron instrument (Mini 44), USA.

#### 5.2.5 Porosity and pore size of the electrospun substrate

The gravimetric method was used to investigate the porosity of the electrospun substrate, using the equation (3-1) [95-99].

The mean pore size of the substrate was determined via the filtration velocity method. The volume of permeate water was obtained using a dead-end stirred cell filtration device (Millipore stirred ultra-filtration cells, 8010, USA, effective area of 0.0003 m<sup>2</sup>) connected to a nitrogen gas cylinder. The  $r_m$  was calculated using the Guerout-Elford-Ferry equation (3-2) [96-99].

The  $R_{max}$  was determined via the bubble point method. The bubble point pressure was determined using the aforementioned dead-end stirred cell filtration system [178]. The substrate

was immersed in DI water for 4 h and then fitted on the dead-end cell. The output tube of the dead-end cell was immersed in DI water so that the bubble point pressure could be read. The maximum pore size was calculated according to Laplace's equation (3-3) [96]:

#### 5.2.6 Performance evaluation of the TFC membrane

##### 5.2.6.1 Water permeability, salt rejection, salt permeability and structural parameters

A flat-sheet TFC membrane was used to conduct all the forward osmosis experiments. The A and B for the TFC membrane were investigated using a bench-scale cross-flow RO test system. A piece of the membrane with an effective surface area of 19.94 cm<sup>2</sup> was placed in a stainless steel test cell with the active surface of the membrane facing the feed stream. Using a high-pressure positive displacement pump (Hydra-cell pump), the feed solution was re-circulated at 1.0 L/min. DI water was used as the feed stream to investigate A, and a 20 mM solution of NaCl was used as the feed stream to investigate R and B for the TFC membrane. Water permeability coefficient, solute rejection and salt permeability coefficient for the membrane were determined using equations (4-1), (4-2), (4-3) and (4-4) [95,137,139-140].

The pressure was increased in 0.345 MPa increments from 0.345 to 1.034 MPa in order to investigate A of the TFC membrane. Constant pressure was applied at each increment for 8h. The water flux through the membrane was obtained from a liquid flow sensor (Sensirion, The Sensor Company) directly connected to a computer. To investigate R and B, 1.896 MPa pressure was applied to the RO cell. Conductivity of the feed and permeate solutions was investigated using a calibrated conductivity meter (Oakton, Eutech Instruments) to calculate solute rejection. This experiment was conducted at a constant temperature of 24 °C using a chiller (Polystat, Cole-Parmer).

A bench-scale FO test system was used to determine the S of the TFC membrane by applying the equation (4-5) [95, 139, 141-142]. In this approach, de-ionized water was used as the feed solution, while 1 M NaCl was used as the draw solution.

##### 5.2.6.2 Water flux and reverse salt flux in FO experiment

A bench-scale experimental setup (Figure 2-6) was used to evaluate the FO performance of the TFC membranes. DI water and 1M NaCl solution were used as the feed and draw solutions, respectively, in the FO experiment. A piece of the membrane with an effective surface area of 19.94 cm<sup>2</sup> was placed in an acrylic cross-flow cell with the active layer of the membrane facing the feed stream. On both sides of the membrane, the cross-flow cell had symmetric channels,

which allowed for both the feed and the draw solutions to flow tangential to the membrane. Recirculation of the feed solution and the draw solution on the opposite sides of the membrane was executed using two variable-speed gear pumps (Gear Pump Drive, Cole-Parmer Instrument Company). The flow rate of each solution was maintained at 0.5 L/min. The feed solution temperature and the draw solution temperature were held at a constant temperature of 24 °C and monitored with a thermometer. The feed solution and the draw solution were placed in two separate 4.0 L reservoirs to conduct the experiment. The feed solution container was placed on a digital analytical balance. The water flux and the reverse salt flux were determined to evaluate the FO performance of the TFC membranes. Each experiment was conducted for one hour and the concentration of the draw solution was adjusted by adding concentrated draw solution in every 15 min. The water flux through the membrane was obtained from the digital analytical balance by using equation (4-1). To investigate the reverse salt flux, a sample of the feed solution was collected before and after the experiment to determine the salt concentration using a calibrated conductivity meter (Oakton, Eutech Instruments). Reverse salt flux was calculated using equation (4-6) [143].

#### 5.2.6.3 Membrane antifouling test

Sodium alginate (SA) and calcium sulfate ( $\text{CaSO}_4$ ) were used as model organic and inorganic foulants, respectively, to investigate the antifouling properties of the FO membranes. The membrane coupon was placed into the FO cell with the active layer facing the feed side. The membrane coupon was immersed in DI water for 24 h before conducting the antifouling test. First, the FO experiment was conducted for 6 h at a flow rate of 0.5 L/min using 1 M NaCl as draw solution and DI water as feed. Then, 1 M NaCl, as draw solution, and DI water with SA (200 mg/L) and  $\text{CaCl}_2$  (1 mM), as feed solution, were used to conduct the antifouling test for 6 h at the same flow rate (0.5 L/min) using a new membrane coupon. In order to investigate antifouling propensity in relation to  $\text{CaSO}_4$ , 1 M NaCl as draw solution and DI water with  $\text{CaSO}_4$  (2000 mg/L) as feed solution, were used to conduct the antifouling test. This experiment was also conducted for 6 h at a flow rate of 0.5 L/min using a new membrane coupon. Weight changes of the feed solution throughout the FO experiments were monitored precisely using a digital weight balance at fifteen-minute intervals. Now, for 2 h, DI water with a flow rate of 1 L/min was applied to physically clean the membrane active surface of the both fouled membranes (fouled by SA and  $\text{CaSO}_4$ ). In the FO experiment, the water flux through the

cleaned membranes was measured using 1 M NaCl and DI water as draw and feed, respectively, in order to investigate flux recovery for these membranes. These experiments were also conducted for 6 h at a flow rate of 0.5 L/min in which the weight changes of the feed solution were monitored using a digital weight balance at fifteen-minute intervals.

### 5.3 Results and discussion

#### 5.3.1 Morphology of the electrospun substrates

The FE-SEM images of pristine N6 and N6/SiO<sub>2</sub> composite electrospun substrates with 20 wt.% SiO<sub>2</sub> content are shown in Figure 5-1. The electrospun N6/SiO<sub>2</sub> composite with 20 wt.% SiO<sub>2</sub> content was the best composite studied in our previous report [178]. Pristine electrospun N6 substrate showed a fibrous morphology in which the diameter of the fibers ranged between 80 to 160 nm (Figure 5-1 A). The spider-web like structure was also obtained in the electrospun N6 substrate due to higher applied voltage (30 kV) during electrospinning of the N6 solution. In fact, the higher applied voltage during the electrospinning caused N6 to ionize in the acid solvent, which resulted the formation of spider-web like structure in the electrospun N6 substrate (Figure 5-1 A) [82,105,178]. As seen in Figure 5-1 B, the diameters of fibers of the electrospun N6 substrate increased with the addition of SiO<sub>2</sub> nanoparticles. The addition of highly surface-active SiO<sub>2</sub> nanoparticles can increase both the viscosity and surface tension of electrospinning solutions, which contribute to increase the diameters of nanofibers of the electrospun N6/SiO<sub>2</sub> composite substrate [106]. Furthermore, the density of the spider-web like structure of electrospun substrates was decreased with the incorporation of SiO<sub>2</sub> nanoparticles (Figure 5-1 A and Figure 5-1 B). The addition of SiO<sub>2</sub> nanoparticles may have decreased the conductivity of the ionic N6 solution, which in turn decreased the ionization of the N6 during the electrospinning process. Hence, the density of the spider-web like structure of electrospun N6/SiO<sub>2</sub> composite substrate was decreased due to a decrease in the conductivity of the ionic N6 [82].

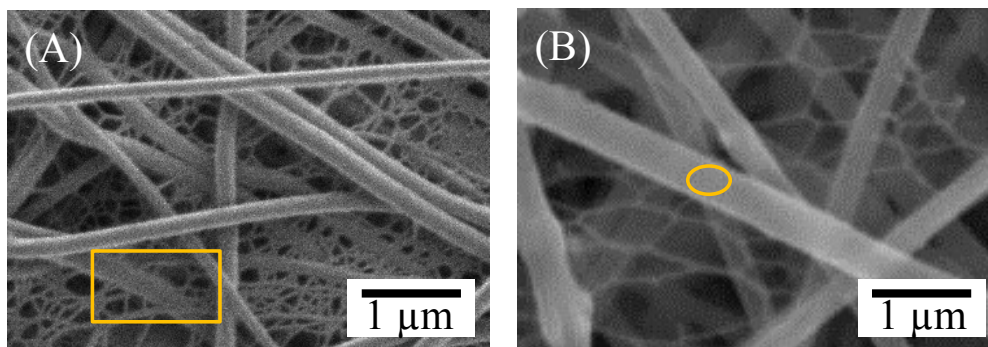


Figure 5-1. FE-SEM images of electrospun substrates of (A) N6 and (B) N6/SiO<sub>2</sub> (20 wt.%) composite. A mixture of 80% formic acid and 20% acetic acid by volume was used as solvent to prepare pristine N6 and N6/SiO<sub>2</sub> blended solutions for electrospinning. The surface of the electrospun substrates was coated with Pt to capture these FE-SEM images. The SEM-EDX spectra of the electrospun substrates were taken from the yellow spotted regions.

The SEM-EDX spectra of the electrospun substrates for the pristine N6 and N6/SiO<sub>2</sub> composite are exhibited in Figure 5-2. The EDX analysis suggests the presence of C, N and O atoms of N6 (Figure 5-2 A). Pt was also obtained in the EDX spectrum due to the Pt coating applied to conduct the SEM analysis for the electrospun N6 substrate. The N6/SiO<sub>2</sub> composite substrate showed a new peak for Si and an O peak with a higher intensity (Figure 5-2 B) than previously observed for N6 alone (Figure 5-2 A). This result confirmed the successful incorporation of SiO<sub>2</sub> nanoparticles into the electrospun N6 substrate.

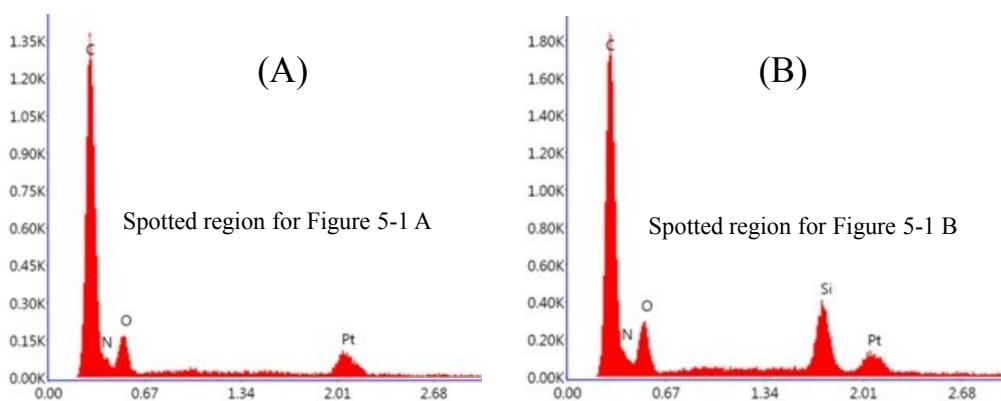


Figure 5-2. SEM-EDX spectra of electrospun substrates of (A) N6 and (B) N6/SiO<sub>2</sub> composites. (The SEM-EDX spectra of the electrospun substrates of pristine N6 and N6/SiO<sub>2</sub> composites were taken from the yellow spotted regions of Figure 5-1).

The TEM images of the electrospun substrates of pristine N6 and N6/SiO<sub>2</sub> composites are exhibited in Figure 5-3 A and Figure 5-3 B, respectively. The SiO<sub>2</sub> nanoparticles were incorporated and well distributed in the N6 nanofibers of the electrospun substrates (Figure 5-3 B). The TEM images also show the size of the SiO<sub>2</sub> nanoparticles, which is about 30 nm, in the nanofibers of the electrospun substrates.

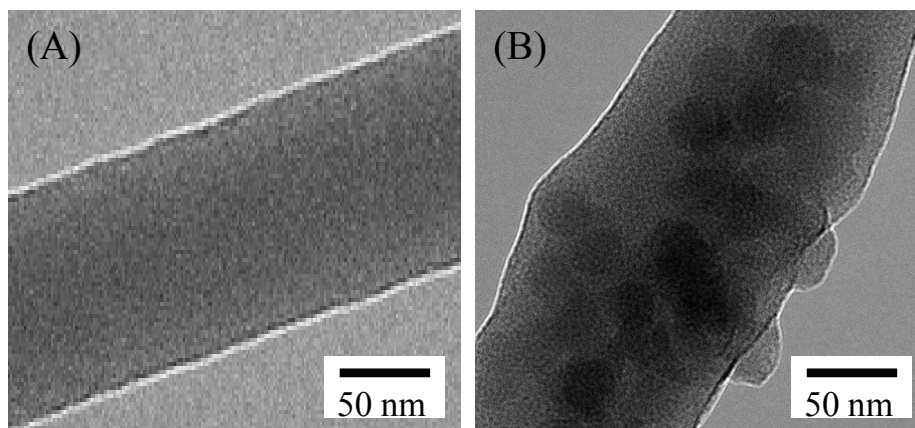


Figure 5-3. TEM images of electrospun substrates of (A) N6 and (B) N6/SiO<sub>2</sub> composites. The Cu grid and Si detector were used when capturing the TEM images of the electrospun substrates.

### 5.3.2 Structural study of the electrospun N6/SiO<sub>2</sub> composite by XRD and FTIR analysis

Figure 5-4 A shows the XRD data for the electrospun substrates of pristine N6 and the N6/SiO<sub>2</sub> composite with 20 wt.% SiO<sub>2</sub> content. The XRD data of the pristine N6 shows a peak at  $2\theta = 21.2^\circ$  indicating the morphology of a semi-crystalline polymer containing crystals of  $\gamma$ -form, which is consistent with the literature [108]. The incorporation of SiO<sub>2</sub> into N6 caused a reduction in the peak intensity and a smaller peak appeared as a result of the crystal structure splitting from  $\gamma$  ( $2\theta = 21.2^\circ$ ) into the  $\alpha$ -form at  $2\theta = 23.5^\circ$  [108].

The FTIR spectra are shown in Figure 5-4 B. The FTIR spectrum of electrospun N6 substrate shows typical peaks at  $1545\text{ cm}^{-1}$  (N-H deformation),  $1637\text{ cm}^{-1}$  (C=O stretching), and  $3294\text{ cm}^{-1}$  (N-H stretching) [106]. These peaks can also be seen in the spectra for 20 wt.% SiO<sub>2</sub> content for the electrospun N6/SiO<sub>2</sub> composite substrate. Two new peaks at  $1100\text{ cm}^{-1}$  and  $800\text{--}700\text{ cm}^{-1}$  were obtained due to incorporation of SiO<sub>2</sub> nanoparticles into the N6 substrate. The peak at  $1100\text{ cm}^{-1}$  was the characteristic signal of a Si-O-Si bond in the N6/SiO<sub>2</sub> composite

[106]. The peak at 800-700  $\text{cm}^{-1}$  was obtained because of  $\nu(\text{Si-OH})$  in the  $\text{N6/SiO}_2$  composite [64]. In fact, hydrogen bonds were formed between the O atom of the hydroxyl group of the  $\text{SiO}_2$  nanoparticles and the H atom of the amide group of N6 (Scheme 5-2).

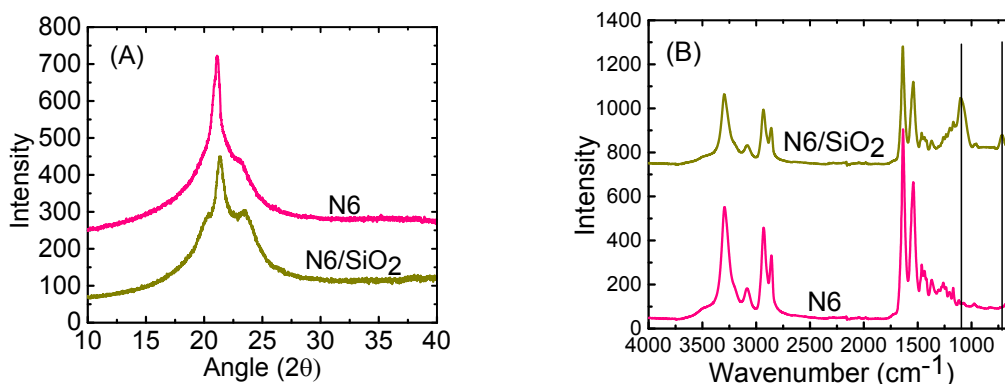


Figure 5-4. (A) XRD and (B) FTIR data for the electrospun N6 and  $\text{N6/SiO}_2$  composite substrates. (The X-ray source is copper and equipped with a Vantec area detector).

### 5.3.3 Wettability and surface roughness of the electrospun substrates

The wettability of the electrospun substrates of pristine N6 and N6 with 20 wt.%  $\text{SiO}_2$  content is shown in Figure 5-5. The water contact angles of the electrospun substrates of N6 and  $\text{N6/SiO}_2$  composite were  $39^\circ$  and  $15^\circ$ , respectively, at the point where the substrate surface was touched by the water droplet (Figure 5-5 A and Figure 5-5 B). The water droplet was quickly absorbed through the electrospun substrates after touching its surface during the contact angle measurement, indicating highly hydrophilic properties of the substrates [110]. The durations of 2.1 sec and 0.75 sec were required by the electrospun N6 and  $\text{N6/SiO}_2$  composite substrates, respectively, to completely absorb the water droplet. Due to incorporation of superhydrophilic  $\text{SiO}_2$  nanoparticles, the electrospun  $\text{N6/SiO}_2$  composite showed greater hydrophilic properties as compared to those of the electrospun N6.

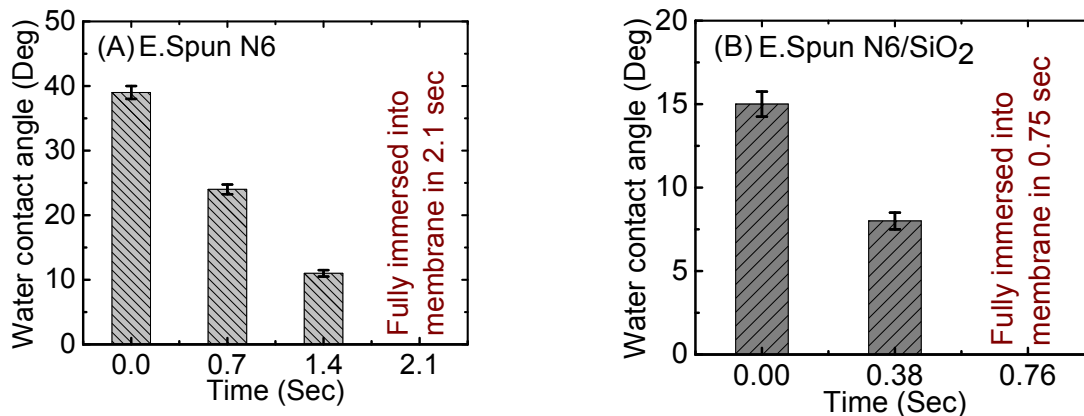


Figure 5-5. Wettability of the electrospun substrates of (A) N6 and (B) N6/SiO<sub>2</sub> composite.

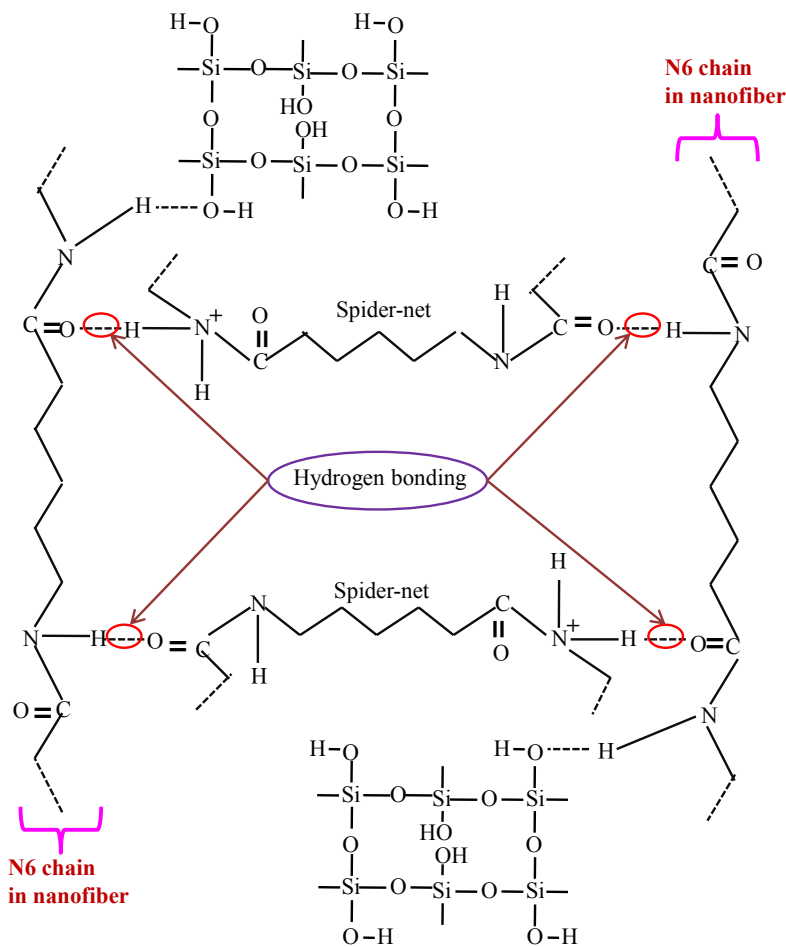
#### 5.3.4 Porosity, pore size and tensile strength of the electrospun substrates

The porosities of the electrospun substrates of pristine N6 and N6/SiO<sub>2</sub> (20 wt.%) composite are shown in Table 5-1. The electrospun N6 substrate with 21 wt% of N6 solution exhibited high porosity (86%) due to the high surface area to volume ratio of the nanofibers of the substrate. However, the incorporation of SiO<sub>2</sub> nanoparticles (20 wt%) increased the porosity of the electrospun N6 substrate by ~ 10% due to the porous structure of the SiO<sub>2</sub> nanoparticles [84]. The average and maximum pore sizes of the electrospun N6 substrate were 406 and 575 nm, respectively, while those values were 478 nm (average) and 661 nm (maximum) for the electrospun N6/SiO<sub>2</sub> composite substrate (Table 5-1). It is assumed that the higher pore sizes are due to higher fiber diameters of the electrospun N6/SiO<sub>2</sub> composite substrate as compared to the electrospun N6 substrate. The tensile strength of the fabricated electrospun substrates is also shown in Table 5-1. The electrospun N6 substrate showed a tensile strength of 19.0 MPa. The high tensile strength of the electrospun N6 substrate was due to the highly interconnected spider-web like structure in the substrate. The ionic species of the N6 solution form stronger hydrogen bonds because of the extra available charge on them in the presence of high applied voltage during the electrospinning process. The protonated amide group of ionic N6 can effectively form hydrogen bonds with oxygen atoms of a N6 molecule in the main fiber and form another hydrogen bond between an oxygen atom between the ionic molecule and a hydrogen atom from the amide group of another main fiber to form the interconnected spider-web like substrate (Scheme 5-2). The incorporation of SiO<sub>2</sub> nanoparticles enhanced the tensile

strength of the electrospun N6 substrate (21.40 MPa), likely due to the integrated network structure of SiO<sub>2</sub> (Scheme 5-2).

Table 5-1. Porosity, pore size, and tensile strength of the electrospun substrates.

Substrate	Porosity (%)	Pore size (nm)		Tensile strength (MPa)
		Average	Maximum	
E.Spun N6	86 ± 1	406 ± 11	575 ± 14	19.0 ± 1
E.Spun N6/SiO <sub>2</sub>	95 ± 0.5	478 ± 13	661 ± 15	21.40 ± 0.85



Scheme 5-2. Schematic representation of the electrospun N6/SiO<sub>2</sub> composite.

### 5.3.5 Characteristics of casted N6 substrate

N6 substrate was prepared by the phase inversion method. The casted N6 substrate was almost nonporous with low wettability (water contact angle  $72^\circ$ ) exhibited in Figure 5- 6. Therefore, the casted N6 substrate cannot be used as an effective substrate for TFC membrane.

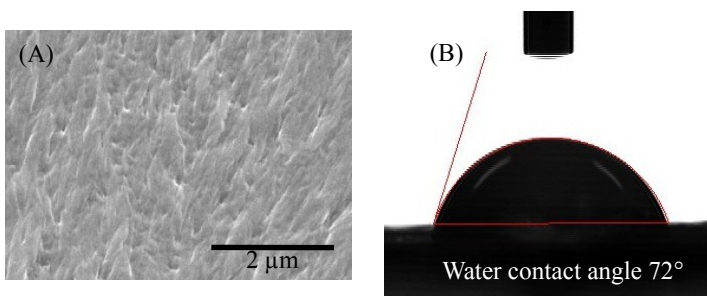
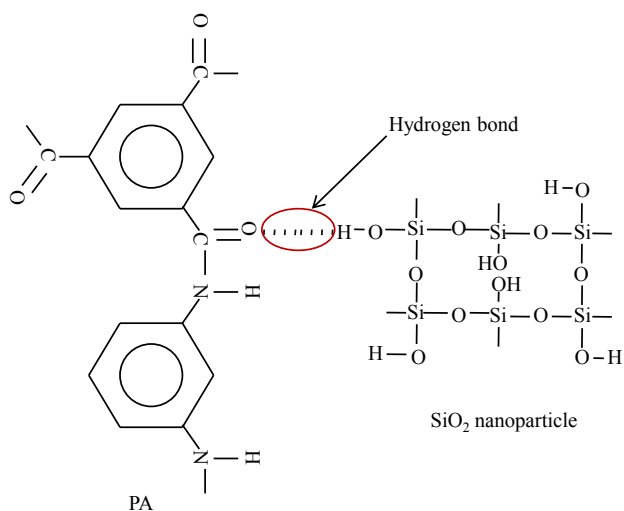


Figure 5-6. (A) FE-SEM image and (B) Water contact angle of casted N6 substrate.

### 5.3.6 Morphology of the TFC membrane

The top surface FE-SEM images of the electrospun N6/SiO<sub>2</sub> composite supported TFC membranes with pristine PA and PA/SiO<sub>2</sub> composite active layers are exhibited in Figure 5-7. The obtained “ridge and valley” structure indicated the successful formation of active layers of pristine PA (Figure 5-7 A) and PA/SiO<sub>2</sub> composite (Figure 5-7 B, Figure 5-7 C, Figure 5-7 D and Figure 5-7 E) on the electrospun N6/SiO<sub>2</sub> composite substrate. Incorporated SiO<sub>2</sub> nanoparticles were clearly observed for the PA/SiO<sub>2</sub> composite active layers (Figure 5-7 B, Figure 5-7 C, Figure 5-7 D and Figure 5-7 E). Some nanoparticles were observed on the surface and some nanoparticles were embedded into the PA active layers. The concentration of the SiO<sub>2</sub> nanoparticles increased as a function of increased incorporated SiO<sub>2</sub> nanoparticles during interfacial polymerization. The sizes of the incorporated SiO<sub>2</sub> nanoparticles were much higher for 6% SiO<sub>2</sub> content (Figure 5-7 E) as compared to the other percentages of SiO<sub>2</sub> content (1, 2 and 4%) (Figure 5-7 B, Figure 5-7 C and Figure 5-7 D). The larger size of particles for 6% SiO<sub>2</sub> content indicated the aggregation of nanoparticles. The highest concentration, with still well dispersed SiO<sub>2</sub> nanoparticles, was observed with a 4% SiO<sub>2</sub> content (Figure 5-7 D) in the active layer. The interaction between PA and SiO<sub>2</sub> nanoparticles in the active layer was obtained due to hydrogen bond formation between the O atom in the hydroxyl group of the SiO<sub>2</sub> nanoparticles and the H atom of the amide group of PA (Scheme 5-3).



Scheme 5-3. A schematic representation of interaction between PA and SiO<sub>2</sub> nanoparticles.

The cross-section of the fabricated electrospun N6/SiO<sub>2</sub> supported TFC membrane with 4% SiO<sub>2</sub> content in the PA active layer is shown in Figure 5-7 F. The thickness of the electrospun substrate was ~85 μm and a very thin PA active layer existed on the surface of the substrate. The PA active layer was strongly attached to the surface of electrospun substrate due to the interaction between the polar amide groups of N6 and the polar amide groups of PA [86]. The top surface FE-SEM images of the electrospun N6 supported TFC membranes with pristine PA and PA/SiO<sub>2</sub> composite (4% SiO<sub>2</sub> content as regards MPD) active layers are also shown in the appendix (Figure C-1, Appendix C).

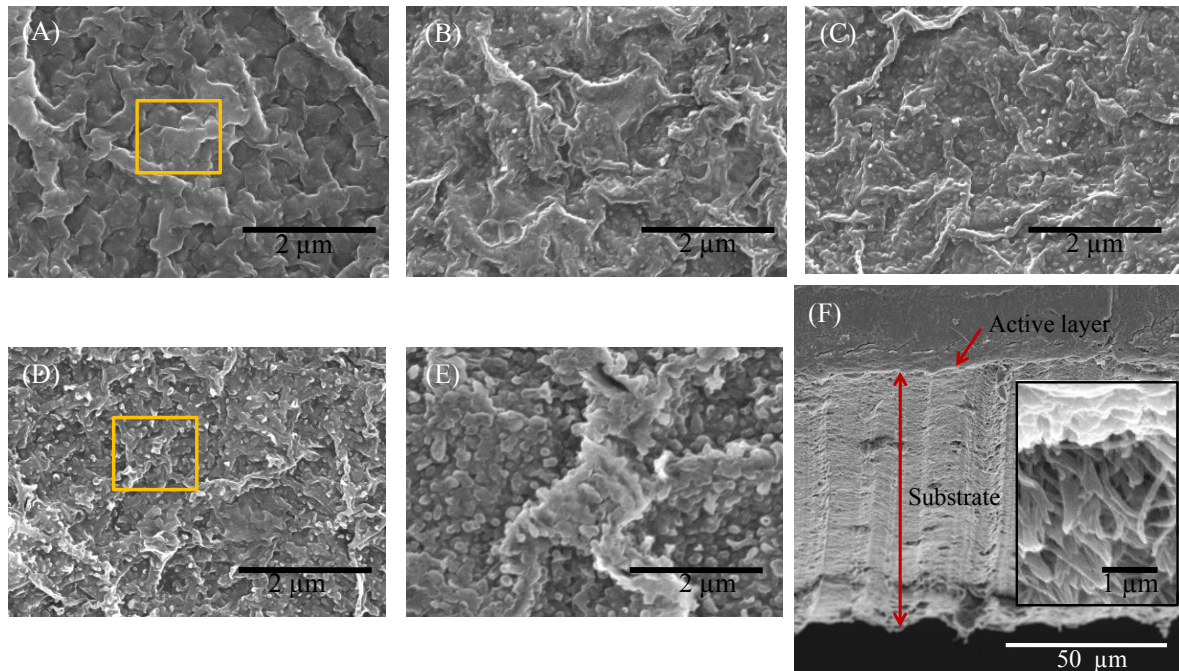


Figure 5-7. FE-SEM images of the top surface of electrospun N6/SiO<sub>2</sub> composite supported TFC membranes with PA/SiO<sub>2</sub> composite active layer with SiO<sub>2</sub> concentrations of (A) 0%, (B) 1%, (C) 2%, (D) 4% and (E) 6%, and (F) Cross-sectional FE-SEM images of the TFC membrane in the case of 4% SiO<sub>2</sub> nanoparticles incorporated in the PA active layer [The percentages of SiO<sub>2</sub> nanoparticles in the active layer were taken with respect to MPD during interfacial polymerization].

The SEM-EDX spectra of the surfaces of the electrospun N6/SiO<sub>2</sub> supported TFC membranes with the pristine PA and the PA/SiO<sub>2</sub> composite active layers are exhibited in Figure 5-8. The EDX analysis suggests the presence of C, N, and O atoms of PA (Figure 5-8 A). Pt was also obtained in the EDX spectrum due to the Pt coating applied to conduct the SEM analysis for the TFC membranes. The PA/SiO<sub>2</sub> composite active layer showed a new peak for Si and an O peak with a higher intensity (Figure 5-8 B) than previously observed for PA alone (Figure 5-8 A). This result confirmed the successful incorporation of SiO<sub>2</sub> nanoparticles into the PA active layer during interfacial polymerization.

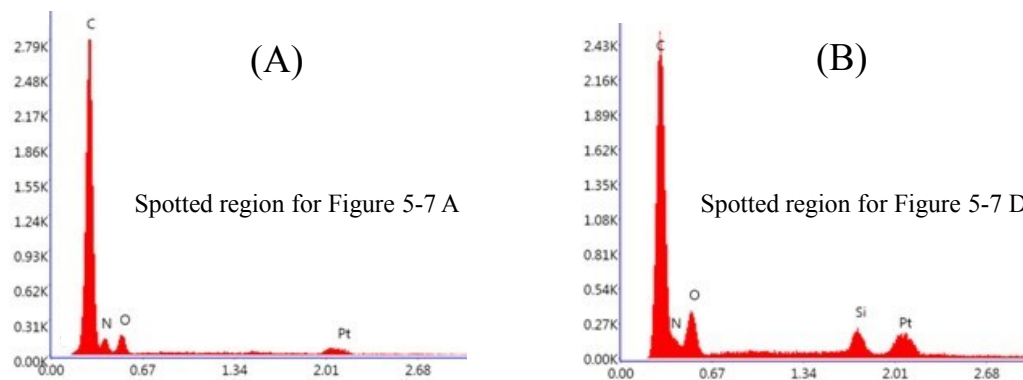


Figure 5-8. SEM-EDX spectra of electrospun N6/SiO<sub>2</sub> composite supported TFC membranes with (A) PA and (B) PA/SiO<sub>2</sub> composite active layers. (The SEM-EDX spectra of the TFC membranes were taken from the yellow spotted regions of Figure 5-7).

The surface roughness of the electrospun N6/SiO<sub>2</sub> supported TFC membranes with the pristine PA and the PA/SiO<sub>2</sub> composite active layers was also investigated through AFM and the result of this investigation is shown in Figure 5-9. The R<sub>a</sub> of the electrospun N6/SiO<sub>2</sub> supported TFC membrane with the pristine PA was 122 nm (Figure 5-9 A). However, the R<sub>a</sub> of the TFC membrane with the active layer of PA/SiO<sub>2</sub> composite increased to 160 nm due to the addition of surface-active SiO<sub>2</sub> nanoparticles (Figure 5-9 B).

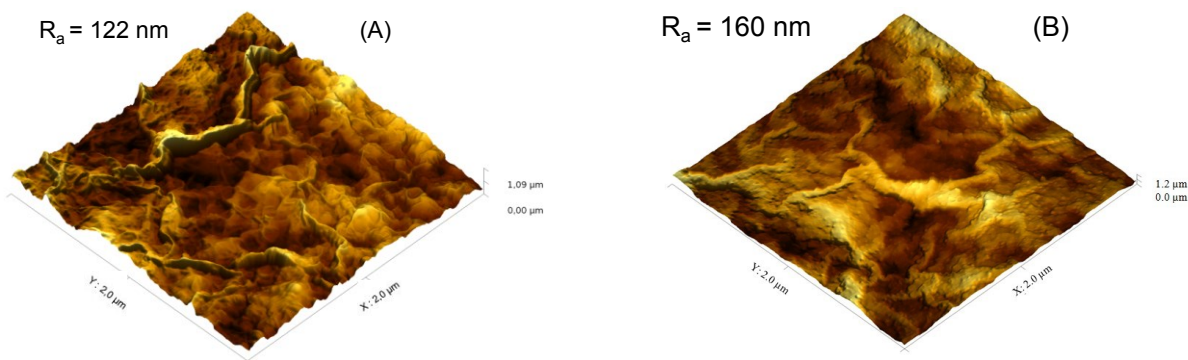


Figure 5-9. AFM images of the TFC membranes of (A) electrospun N6/SiO<sub>2</sub>-PA and (B) electrospun N6/SiO<sub>2</sub>-PA/SiO<sub>2</sub> composites with 4% SiO<sub>2</sub> content in the PA active layer [The percentages of SiO<sub>2</sub> nanoparticles in the active layer were taken into account in regards to MPD during interfacial polymerization].

### 5.3.7 Wettability and tensile strength of the membranes

The wettability of the fabricated and the commercial TFC membranes is exhibited in Table 5-2. The water contact angles of electrospun N6 supported PA TFC membrane (E.Spun N6/PA) and electrospun N6 supported PA/SiO<sub>2</sub> TFC membrane (E.Spun N6-PA/SiO<sub>2</sub>) were 63° and 47°, respectively. The decrease in water contact angle was obtained for the TFC membrane with PA/SiO<sub>2</sub> composite active layer. The water contact angle of the fabricated electrospun N6/SiO<sub>2</sub> supported TFC membrane with PA active layer (E.Spun N6/SiO<sub>2</sub>-PA) was 32°, however the water contact angle reduced to 14° by incorporating 4% SiO<sub>2</sub> nanoparticles (as regards MPD during interfacial polymerization) into the PA active layer. The water contact angle decreased due to superhydrophilic properties of the incorporated SiO<sub>2</sub> nanoparticles into the PA active layer. In Table 5-2, it is also observed that wettability of the fabricated TFC membranes increased with increasing wettability of substrate, while the active layers were identical. In fact, the highly wettable substrate induced the very thin active layer to be more wettable. The water contact angle of the fabricated electrospun N6/SiO<sub>2</sub> supported TFC membrane with PA/SiO<sub>2</sub> active layer was 0.56 times lower as compared to that of the commercial TFC membrane (water contact angle 25°). The obtained water contact angle of the commercial TFC membrane was comparable to the literature value (water contact angle 24°) for the same type of membrane [185].

The tensile strength of the fabricated membranes—as well as commercial TFC membranes—is also exhibited in Table 5-2. The tensile strength of electrospun N6/PA and electrospun N6-PA/SiO<sub>2</sub> TFC membranes were 19.4 and 19.5 MPa, respectively (Table 5-2). The electrospun N6/SiO<sub>2</sub> supported TFC membrane with PA active layer showed a tensile strength of 22 MPa. The tensile strength of the electrospun N6/SiO<sub>2</sub> supported TFC membrane with PA/SiO<sub>2</sub> active layer was almost same as the fabricated TFC membrane with pristine PA active layer (Table 5-2). The very small quantity of incorporated SiO<sub>2</sub> nanoparticles into the PA active layer could not provide any contribution to enhance mechanical strength of the E.Spun N6/SiO<sub>2</sub>-PA/SiO<sub>2</sub> TFC membrane. However, the tensile strength of the electrospun substrates slightly increased after fabricating active layers on it due to fiber binding effect of the active layer (Table 5-1 and Table 5-2). The obtained tensile strength of the commercial TFC membrane was much lower (8.2 MPa) as compared to the fabricated TFC membranes (Table 5-2).

Table 5-2. Water contact angle and tensile strength of the TFC membranes.

Membrane	Water contact angle (°)	Tensile strength (MPa)
E.Spun N6-PA	63 ± 0.9	19.4 ± 0.8
E.Spun N6-PA/SiO <sub>2</sub>	47 ± 1.0	19.5 ± 0.7
E.Spun N6/SiO <sub>2</sub> -PA	32 ± 0.8	22 ± 0.4
E.Spun N6/SiO <sub>2</sub> -PA/SiO <sub>2</sub>	14 ± 0.5	22.3 ± 0.2
Comm. TFC	25 ± 0.7	8.2 ± 0.3

### 5.3.8 Performance of the membranes

#### 5.3.8.1 FO water flux and structural parameter of the membranes

A cross-flow RO cell was used to investigate pure water permeability of the fabricated as well as the commercial TFC membranes, and the obtained water permeability values were 20.1, 23.3, 28.2, 45, and 32.5 LMH/MPa for electrospun N6-PA, electrospun N6-PA/SiO<sub>2</sub>, electrospun N6/SiO<sub>2</sub>-PA, electrospun N6/SiO<sub>2</sub>-PA/SiO<sub>2</sub>, and commercial TFC membranes, respectively. The obtained water permeability value for the commercial TFC membrane is very near to the literature value (31.6 LMH/MPa) for the same type of membrane [54]. The fabricated electrospun N6-PA and electrospun N6-PA/SiO<sub>2</sub> TFC membranes were not considered for further FO performance investigations due to their lower water permeabilities compared to those of the other two fabricated membranes. The structural parameters of the fabricated and the commercial TFC membranes were determined through the investigation of salt rejection and salt permeability coefficient in a cross-flow RO cell (Table 5-3). The salt rejections of the fabricated membranes were 98% for electrospun N6/SiO<sub>2</sub>-PA and 98.5% for electrospun N6/SiO<sub>2</sub>-PA/SiO<sub>2</sub>, whereas it was 97.27% for the commercial TFC membrane. The salt permeability coefficient of the fabricated membranes were 1.04 LMH for electrospun N6/SiO<sub>2</sub>-PA, 1.24 LMH for electrospun N6/SiO<sub>2</sub>-PA/SiO<sub>2</sub>, which were lower than that of the commercial membrane (1.65 LMH). FO water fluxes for the fabricated and the commercial TFC membranes are presented in Table 5-3. In order to obtain water flux, 1 M NaCl and DI water were used as draw solution and feed, respectively, in the FO process. The use of 1 M NaCl as draw solution and DI water as feed is a common practice in FO process [162, 166, 185, 186-195]. The obtained FO water fluxes for the fabricated electrospun N6/SiO<sub>2</sub>-PA/SiO<sub>2</sub> TFC membrane was higher (27.10 LMH) than those of the other fabricated electrospun N6/SiO<sub>2</sub>-PA (17.50 LMH) and the commercial (20.82 LMH) TFC membranes at the same experimental

conditions. Compared to the fabricated electrospun N6/SiO<sub>2</sub>-PA and the commercial TFC membranes, the higher FO water flux was obtained for the fabricated electrospun N6/SiO<sub>2</sub>-PA/SiO<sub>2</sub> TFC membrane due to its higher hydrophilicity with lower structural parameters as presented in Table 5-2 and Table 5-3.

Table 5-3. FO water flux (at 1 M NaCl draw solution against DI water as feed) and structural parameters of the membranes.

Membranes	NaCl solution conc. (mM) in RO test	Osmotic pressure (MPa) of 20 mM NaCl solution	R (%)	B (LMH)	FO water flux (LMH)	S (μm)
E.Spun N6/SiO <sub>2</sub> -PA	20	0.09	98.00	1.04	17.50	554
E.Spun N6/SiO <sub>2</sub> -PA/SiO <sub>2</sub>			98.50	1.24	27.10	365
Comm. TFC			97.27	1.65	20.82	456

\* Applied pressure for rejection test in RO experiment was 1.896 MPa. The pure water permeability of the fabricated electrospun N6/SiO<sub>2</sub>-PA and electrospun N6/SiO<sub>2</sub>-PA/SiO<sub>2</sub> membranes, and the commercial TFC membrane in RO experiments were 28.2, 45, and 32.5 LMH/MPa, respectively. Mutual diffusivity of the NaCl solution was  $1.38 \times 10^{-9}$  m<sup>2</sup>/s. Osmotic pressure of 1 M NaCl solution was 4.6 MPa. Each set of FO experiment was conducted thrice and then the average values of obtained water flux from these three sets of experiments are presented in Table 5-3.

Table 4 presents a comparison between the intrinsic permeation properties of lab-made TFC membranes and the literature TFC flat sheet membranes under both FO and RO conditions.

Table 5-4. Performance comparison of various FO TFC flat-sheet membranes in FO mode.

Membrane	FO performance			RO performance			S ( $\mu\text{m}$ )	Reference
	Feed solution	Draw solution	Water flux (LMH)	A (LMH/MPa)	B (LMH)	R (%)		
E.Spun N6/SiO <sub>2</sub> -PA	DI water	1M NaCl	17.50	28.2	1.04	98	554	This work
E.Spun N6/SiO <sub>2</sub> -PA/SiO <sub>2</sub>			27.10	45	1.24	98.5	365	
Commercial TFC			20.82	32.5	1.65	97.27	456	
TFC1, PA/PES			11.0	6.6	0.35	97.8	460	[185]
TFC2, PA/PES			17.0	18	1.00	97.5	458	
TFC3, PA/PES			26.5	57.8	4.96	93.4	436	
PA/PSf			15.8	11.6	0.47	97.4	492	[166]
PA/PSf			25.0	19.0	0.33	98.6	312	[186]
PA/PES-co-sPPSU			20.0	7.3	0.25	91.0	324	[187]
PA/PES			47.0	17.0	-	97.0	80	[188]
PA/PES-SPSF			32.0	7.7	0.11	93.5	238	[162]
PA/CAP			10.0	18.2	0.19	89.2	789	[189]
PA/PSf-SPEK			23.0	7.5	0.07	89.5	107	[190]
PA/PVDF			28.0	31.5	2.33	84.4	325	[191]
PA/PK			27.0	25.0	0.18	-	280	[192]
Zeolite NaY-PA/PSf			11.0	25.7	1.57	77.6	782	[193]
PA/PVDF			22.0	12.8	0.28	-	193	[194]
PA/PSf-LDHs			18.1	6.1	0.27	-	148	[195]

### 5.3.8.2 Reverse salt flux and specific reverse salt flux of the membranes in FO process

The reverse salt flux and specific reverse salt flux of the TFC membranes used in FO processes are shown in Figure 5-10. The reverse salt fluxes of the fabricated TFC membranes ( $0.148 \text{ mol.m}^{-2}.\text{h}^{-1}$  for electrospun N6/SiO<sub>2</sub>-PA and  $0.16 \text{ mol.m}^{-2}.\text{h}^{-1}$  for electrospun N6/SiO<sub>2</sub>-PA/SiO<sub>2</sub>) were lower as compared to that of the commercial TFC membrane ( $0.191 \text{ mol.m}^{-2}.\text{h}^{-1}$ ) (Figure 5-10 A). Due to incorporation of SiO<sub>2</sub> nanoparticles into the active layer, a little higher reverse salt flux was obtained for the fabricated electrospun N6/SiO<sub>2</sub>-PA/SiO<sub>2</sub> TFC membrane as compared to the other fabricated membrane (electrospun N6/SiO<sub>2</sub>-PA). Higher salt permeability in RO test (Table 5-3) also supports the higher reverse salt flux for the fabricated electrospun N6/SiO<sub>2</sub>-PA/SiO<sub>2</sub> TFC membrane as compared to that of the fabricated electrospun N6/SiO<sub>2</sub>-PA TFC membrane. However, the specific reverse salt flux of the fabricated electrospun N6/SiO<sub>2</sub>-PA/SiO<sub>2</sub> TFC membrane (specific reverse salt flux  $5.9 \times 10^{-3} \text{ mol.L}^{-1}$ ) was much lower, as compared to those of the fabricated electrospun N6/SiO<sub>2</sub>-PA (specific reverse salt flux  $8.46 \times 10^{-3} \text{ mol.L}^{-1}$ ) and the commercial (specific reverse salt flux  $9.17 \times 10^{-3} \text{ mol.L}^{-1}$ ) TFC membranes (Figure 5-10 B). Higher water flux was responsible for obtaining lower specific reverse salt flux for the fabricated electrospun N6/SiO<sub>2</sub>-PA/SiO<sub>2</sub> membrane as compared to the other two membranes.

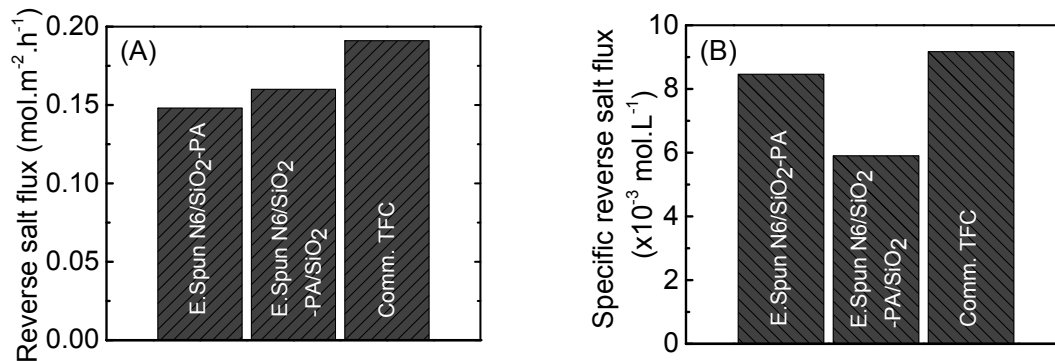


Figure 5-10. (A) Reverse salt flux and (B) Specific reverse salt flux of the membranes. Each set of FO experiments was conducted thrice and then the average values of obtained reverse salt flux and specific reverse salt flux from these three sets of experiments are presented in Figure 5-10.

### 5.3.8.3 Antifouling propensity of membrane in the FO process

The antifouling propensity of the fabricated membrane, as well as commercial TFC membrane, was studied in the presence of two separate foulants, namely SA (model organic foulant) with calcium ions (as bridging agent) and  $\text{CaSO}_4$  (model inorganic foulant). The fouling behavior of the TFC membranes with these two foulants is illustrated in Figure 5-11. The decline in water flux due to reverse salt flux in 6 h were 5, 8, and 13% for the fabricated electrospun N6/SiO<sub>2</sub>-PA, electrospun N6/SiO<sub>2</sub>-PA/SiO<sub>2</sub>, and the commercial TFC membranes, respectively, when using 1 M NaCl as draw solution and DI water as feed solution (Figure 5-11 A). However, 17, 12, and 21.5% declines of water flux were obtained for the fabricated electrospun N6/SiO<sub>2</sub>-PA, electrospun N6/SiO<sub>2</sub>-PA/SiO<sub>2</sub>, and the commercial TFC membranes, respectively, when SA with calcium ions was used as the foulant (Figure 5-11 B). In Figure 5-11 B, 12, 4 and 8.5% declines of water flux were observed for the fabricated electrospun N6/SiO<sub>2</sub>-PA, electrospun N6/SiO<sub>2</sub>-PA/SiO<sub>2</sub>, and the commercial TFC membranes, respectively, due to fouling caused by SA. A higher antifouling propensity was obtained due to higher hydrophilicity of the fabricated electrospun N6/SiO<sub>2</sub>-PA/SiO<sub>2</sub> membrane as compared to the two other types of membranes. The membranes were physically cleaned after conducting the fouling experiments with SA. The water flux of the cleaned membranes was determined in the use of 1 M NaCl as a draw solution and DI water as feed in order to investigate water flux recovery of the membranes. The initial water flux recovery of 87, 98, and 90% with water flux decline of 9, 10, and 16% after 6 h was obtained for the fabricated electrospun N6/SiO<sub>2</sub>-PA, electrospun N6/SiO<sub>2</sub>-PA/SiO<sub>2</sub>, and the commercial TFC membranes, respectively (Figure 5-1 C). The decline in water flux for the electrospun N6/SiO<sub>2</sub>-PA, electrospun N6/SiO<sub>2</sub>-PA/SiO<sub>2</sub>, and the commercial TFC membranes were 18%, 13%, and 23%, respectively, when  $\text{CaSO}_4$  was used as the foulant (Figure 5-1 D). Water flux declines of 13, 5 and 10% were observed for the fabricated electrospun N6/SiO<sub>2</sub>-PA, electrospun N6/SiO<sub>2</sub>-PA/SiO<sub>2</sub>, and the commercial TFC membranes, respectively, due to fouling caused by  $\text{CaSO}_4$  (Figure 5-1 D). The membranes were also cleaned physically after conducting the fouling experiments with  $\text{CaSO}_4$  and the water flux of the cleaned membranes was determined in order to investigate water flux recovery of the membranes. An initial water flux recovery of 82, 94, and 87% with water flux decline of 11, 12, and 18% after 6 h was obtained for electrospun N6/SiO<sub>2</sub>-PA, electrospun N6/SiO<sub>2</sub>-PA/SiO<sub>2</sub>, and the commercial TFC membranes, respectively (Figure 5-11 E). The fabricated electrospun N6/SiO<sub>2</sub>-PA/SiO<sub>2</sub> TFC

membrane exhibited the best antifouling performance for both foulants (SA and CaSO<sub>4</sub>) due to incorporation of superhydrophilic SiO<sub>2</sub> nanoparticles into the PA active layer [196].

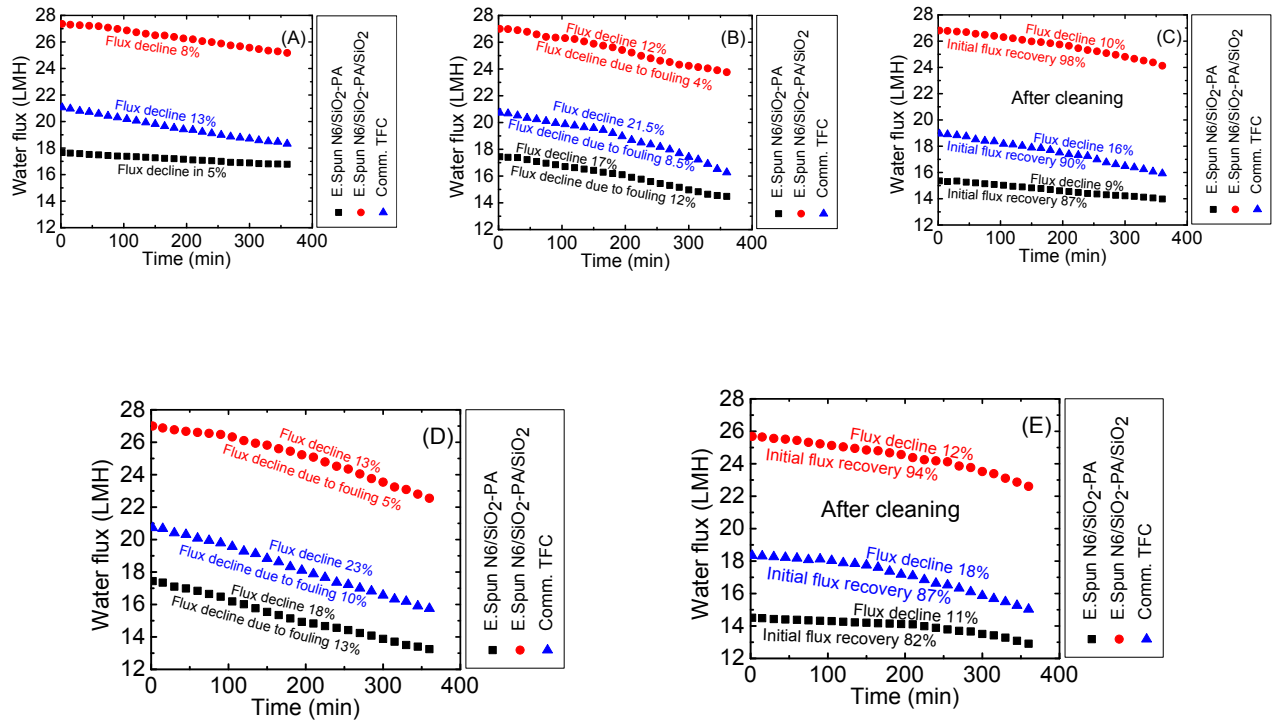


Figure 5-11. (A) Decline of water flux when 1 M NaCl was used as draw solution against DI water as feed, (B) Fouling behavior of the membrane when 1 M NaCl was used as draw solution against DI water with foulant, SA, as feed solution, (C) Decline of water flux after cleaning of the membrane fouled by SA (Draw solution: 1 M NaCl, Feed solution: DI water), (D) Fouling behavior of membrane when 1 M NaCl was used as draw solution against DI water with foulant, CaSO<sub>4</sub>, as feed solution and (E) Decline of water flux after cleaning of the membrane fouled by CaSO<sub>4</sub> (Draw solution: 1 M NaCl, Feed solution: DI water). [Each set of FO experiments was conducted thrice and then the average values of obtained water flux from these three sets of experiments are presented in Figure 5-11].

#### 5.4 Conclusions

A thin-film composite forward osmosis membrane containing SiO<sub>2</sub> nanoparticles with high water flux and antifouling properties was successfully prepared using a facile electrospinning technique combined with interfacial polymerization on surface of electrospun nanofiber mat. The successful fabrication of the TFC membrane was confirmed via FE-SEM, TEM, XRD, FTIR, and AFM analyses. The fabricated membrane was highly hydrophilic (water contact angle 14°) with high mechanical strength (tensile strength 22.3 MPa). The fabricated membrane also showed a high water flux of 27.10 LMH with a low specific reverse salt flux ( $5.9 \times 10^{-3}$  mol.L<sup>-1</sup>) in the FO process. The initial water flux recovery of 98% for SA foulant and 94% for CaSO<sub>4</sub> foulant indicated a high antifouling propensity for the fabricated TFC membrane when used in the FO process. The membrane was also stable due to a beneficial interaction between the electrospun substrate and the active layer. Depending on the obtained performance of the membrane, it can be concluded that the novel fabricated TFC membrane has a huge potential in the FO process.

#### Acknowledgements

Md. Saifur Rahaman gratefully acknowledges the FRQNT for providing the funding support for this project. Md. Shahidul Islam acknowledges the support of a doctoral-level scholarship from the FRQNT. The authors also acknowledge supports from the NSERC and Concordia University, Canada.

## **Chapter 6: Performance of Combined MF-FO-MD Processes for Fracking Wastewater Treatment**

### **Abstract**

The discharge of highly saline fracking wastewater produced by hydraulic fracturing is of great concern due to both human health and environmental effects. Microfiltration as a pre-treatment process and the emerging forward osmosis—coupled with membrane distillation (a downstream separator)—as post-treatment processes were successfully applied for the first time to treat fracking wastewater. Microfiltration as a pre-treatment removed ~52% of TOC and ~98.5% of turbidity. High average water fluxes (19.98 LMH for NaCl and 30.97 LMH for NaP draw solutions) with high solute rejection were obtained via the FO process using a nanocomposite membrane. This research also demonstrated that 98.5% of initial water flux can be recovered with the nanocomposite membrane after desalination of the fracking wastewater. Membrane distillation can be used as a downstream separator in order to recycle FO draw solutions, along with the production of pure water.

**Keywords:** Performance; Combined MF-FO-MD processes; Fracking wastewater treatment

## 6.1 Introduction

A massive source of natural gas exists in pockets of underground porous rocks, also described as “shale gas” [4]. The hydraulic fracturing technique has opened the underground porous rocks as viable natural gas zones [117]. The process in which drilling and injecting fluid into the ground at high pressure in order to crack shale rocks, releasing the natural gas inside is termed as “hydraulic fracturing” or “fracking” for short [121]. In this process, a sand/water suspension and proppants (chemicals) are pumped, at high pressure, into the shale layer after drilling [121]. Consequently, natural gas is released and flows back up with the drilling fluids. Currently shale gas is being produced in many regions of the United States [118]. In the United States, the production of shale gas through hydraulic fracturing has been criticized due to the negative environmental impacts and management implications of hydraulic fracturing fluids, also known as “fracking wastewater” [17]. The management of fracking wastewater is crucial to both maintain the appreciative economics of shale gas development and defend both the environment and human health [20,25]. A possible solution to these issues is to treat fracking wastewater before discharge/reuse. High-salinity is the main characteristic of fracking wastewater, which contains different types of inorganic salts obtained from underground brines [21]. Shale gas wastewater also contains dissolved organic compounds, oil, and sand [22-24]. The treatment of highly saline fracking wastewater is both challenging and energy intensive. Various technologies, such as mechanical vapor compression, reverse osmosis, membrane distillation, and forward osmosis, can be used to desalinate fracking wastewater [24]. Mechanical vapor compression and reverse osmosis are energy-intensive processes and the composition of fracking wastewater can create distinctive challenges in the membrane distillation process [24]. However, forward osmosis (FO) process can desalinate fracking wastewater using fairly straightforward and economic, low-pressure equipment in which wastewater is treated by osmotic pressure rather than hydraulic pressure [24]. The primary principle behind this process is osmosis, the natural diffusion of water (water flux) through a semi-permeable membrane from a low salinity feed solution into a high salinity draw solution [122-123]. To make the FO process commercially viable, the engineered draw solution also needs to be reused. Membrane distillation (MD) can be used as a separator downstream of the FO process to recycle the FO draw solutions [57]. Membrane distillation is an emerging technology that utilizes low-grade heat or industrial waste-heat at a temperature of ~50°C to

drive separation [24]. MD is a thermally driven process in which water vapor transport occurs across a non-wetted microporous hydrophobic membrane. The driving force behind the MD process is the vapor pressure gradient, which is generated by a temperature difference across the membrane. Pre-treatment of fracking wastewater is required to increase the efficiency and life expectancy of the membrane by minimizing fouling of the membrane used in FO process. Pre-treatment can remove sand particles and oil from fracking wastewater to make the wastewater more suitable for FO. Ultrafiltration and microfiltration (MF) processes are commonly used for the separation of oil from water [59-62,178]. These pre-treatment processes can also remove sand particles from water. Depending on the non-dissolved contaminants—such as sand and oil in fracking wastewater—ultrafiltration or microfiltration can be used as pre-treatment technology. However, microfiltration is more convenient than ultrafiltration, which needs higher pressure but provides lower permeability than microfiltration.

In this research, a combined process, comprised of microfiltration, forward osmosis and membrane distillation was applied for the first time for the treatment of fracking waster. After applying this combined process, fresh water was obtained from fracking wastewater.

## 6.2 Materials and methods

### 6.2.1 Materials

Sodium chloride (NaCl) and sodium propionate (NaP) were purchased from Sigma-Aldrich, USA. Nanocomposite microfiltration membranes were produced by our laboratory and polysulfone (PSf) microfiltration membranes were purchased from Pall Corporation, USA. The flat-sheet thin-film composite (TFC) FO membranes were obtained from our laboratory [nanocomposite membrane] and Hydration Technology Innovations (HTI, Albany, OR, USA) [polyamide (PA) membrane]. Millipore, USA, provided poly(vinylidene fluoride) (PVDF) membrane (Durapore<sup>R</sup>) (mean pore size 0.22  $\mu\text{m}$ , porosity 75%) for membrane distillation. Sample fracking wastewater was obtained from Canbriam Energy Inc., Calgary, Alberta, Canada. The composition of dissolved inorganic solids in this wastewater is provided in Table 4-2. De-ionized (DI) water was supplied from a Millipore Integral 10 water system (Millipore, Billerica, MA).

## 6.2.2 Methods

### 6.2.2.1 Physicochemical characterization of membranes

The thicknesses of all membranes were measured using a TMI instrument (Testing Machines, Inc.) [178]. The wettability and tensile strength of the membranes were investigated using a VCA optima instrument (AST Products, Inc.) and Instron (Mini 44), USA, respectively. Field emission-scanning electron microscopy (FE-SEM) (QUANTA FEG 450) with a platinum coating on the sample surface was performed to examine the morphology of the FO membranes.

### 6.2.2.2 Porosity and pore sizes of MF membranes

The gravimetric method was used to investigate porosity of the MF membranes using the following equation (3-1) [95-99].

The mean pore size of the MF membranes was determined via the filtration velocity method. The volume of permeate water was obtained using a dead-end stirred cell filtration device (Millipore stirred ultra-filtration cells, 8010, USA, effective area of 0.0003 m<sup>2</sup>) connected to a nitrogen gas cylinder. The mean pore size ( $r_m$ ) was calculated using the Guerout-Elford-Ferry equation (3-2) [96-99].

### 6.2.2.3 Pure water permeability of the membranes

Pure water flux for the MF membranes was measured using a dead-end stirred cell filtration device (Millipore stirred ultra-filtration cells, 8010, USA, effective area of 0.0003 m<sup>2</sup>) connected to a nitrogen gas cylinder. The membrane was pre-compacted at an applied pressure of 0.28 bar until a constant water flux was achieved. Pure water flux at a temperature of 25 °C was measured at the applied pressures of 0.28, 0.55, 0.83, 1.1 and 1.38 bar. The equations (3-4) and (3-5) were used to calculate pure water permeability for the MF membranes [95,100].

The water permeability for the FO membranes were investigated using a flat-sheet bench-scale cross-flow RO test system. A piece of the membrane with an effective surface area of 19.94 cm<sup>2</sup> was placed in a stainless steel test cell with the active surface of the membrane facing the feed stream. Using a high-pressure positive displacement pump (Hydra-cell pump), the feed solution was re-circulated at 1.0 L/min. DI water was used as the feed stream to investigate water permeability for the FO membranes. Water permeability for the membrane were calculated using the equations (4-1) and (4-2) [95,137,139-140].

The pressure was increased in 3.45 bar increments from 3.45 to 10.34 bar in order to investigate A of the FO membranes. Constant pressure was applied at each increment for 8 h. The water flux through the membrane was obtained from a liquid flow sensor (Sensirion, The Sensor Company) that was directly connected to a computer.

#### 6.2.2.4 Treatment of fracking wastewater

The treatment of fracking wastewater involved three steps: microfiltration, then forward osmosis and finally recovery of draw solution and pure water production by membrane distillation. The fracking wastewater treatment process is shown schematically in Figure 1-4.

##### 6.2.2.4.1 Pre-treatment of the fracking wastewater

Microfiltration for fracking wastewater water was conducted using both nanocomposite and PSf membranes in a dead-end stirred cell filtration device (Millipore stirred ultra-filtration cells, 8010, USA, effective area of 0.0003 m<sup>2</sup>) connected to a nitrogen gas cylinder. The membranes were pre-compacted using DI water at an applied pressure of 0.28 bar until a constant water flux was achieved. Then, microfiltration using the fracking wastewater as a feed was conducted for 12 h at a stirring rate of 500 rpm and an applied pressure of 0.28 bar. Turbidity, total organic carbon (TOC), conductivity and pH of the fracking wastewater after sample collection and after microfiltration were investigated using a MicroTPW Turbidimeter (HF, Scientific, Inc., USA), a TOC analyzer (TOC V<sub>CPH/CPN</sub>, Shimadzu Corp., Japan), a calibrated conductivity meter (Oakton, Eutech Instruments) and a calibrated pH meter (Oakton, Eutech Instruments), respectively.

The osmotic pressure of the fracking wastewaters after microfiltration was also investigated in the following way.

The van Laar equation (4-8) was used to calculate the osmotic pressure of the fracking wastewater [144-145]. The water activity was calculated by using the equation (4-9) [144,146-147]. The vapor pressures of the fracking wastewater and DI water were investigated using a U-Tube Manometer (Tenaquip, Canada).

Water flux recovery for the MF membranes after pre-treatment of fracking wastewater was also investigated. After filtering the fracking wastewater, the membranes were cleaned by rinsing of DI water for 30 min, and the pure water flux was then measured again using the equation (3-4) at the same applied pressure (0.28 bar). The water flux recovery was calculated according to the equation (3-8) [62,96, 98, 102-103].

#### 6.2.2.4.2 Treatment of the pre-treated fracking wastewater by FO

A bench-scale FO experimental setup (Figure 2-6) was used to desalinate fracking wastewater using the nanocomposites as well as the PA membranes. A piece of the membrane with an effective surface area of  $19.94 \text{ cm}^2$  was placed in an acrylic cross-flow cell with the active layer of the membrane facing the feed solution. The fracking wastewater was used as feed, and NaCl (4.0 M) and NaP (4.6 M) were used as draw solutions to investigate desalination of the fracking wastewater via FO. The osmotic pressures of these two draw solutions (NaCl 4.0 M and NaP 4.6 M) were determined using the OLI Stream Analyzer™ (OLI Systems, Inc.). On both sides of the membrane, the cross-flow cell had symmetric channels, which allowed for both the feed solution and the draw solution to flow tangentially to the membrane. Re-circulation of the feed solution and the draw solution on the opposite sides of the membrane was executed using two variable-speed gear pumps (Gear Pump Drive, Cole-Parmer Instrument Company). The flow rate of each solution was maintained at a constant 0.5 L/min. The feed solution temperature and the draw solution temperature were held constant at  $24^\circ\text{C}$  and monitored with a thermometer. The feed solution and the draw solution were placed in two separate 4.0 L reservoirs to conduct the experiment. The feed solution container was placed on a digital analytical balance. Each experiment was conducted for six hours and the concentration of the draw solution was adjusted by adding concentrated draw solution in every 15 min. The water flux for the FO membranes was obtained from the digital analytical balance by using the equation (4-1). Samples of the feed and draw solutions before and after the FO experiment were collected in order to investigate TDS and TOC. The gravimetric method was used to determine TDS while a TOC analyzer (TOC V<sub>CPH/CPN</sub>, Shimadzu Corp., Japan) was used to examine TOC of the feed and draw solutions [148-149].

#### 6.2.2.4.3 Water flux recovery for the FO membranes fouled by fracking wastewater

To investigate water flux recovery for the FO membranes fouled by pre-treated fracking wastewater, the weight changes of feed solution throughout the FO experiments was monitored closely (30 minute interval) using a digital weight balance. After FO, DI water (in the both feed and draw side) was applied for 2 h with a flow rate of 1 L/min to physically clean the active surface of the fouled membranes. The water flux through the cleaned membranes was finally measured using 4.6 M NaP and pre-treated fracking wastewater as draw and feed solutions, respectively, in the same FO experiment set-up in order to investigate water flux recovery for

these membranes. These experiments were conducted for 6 h at the flow rate of 0.5 L/min in which the weight changes of feed solution were monitored using a digital weight balance at thirty minute intervals. The same experiment was also conducted for NaCl draw solution (4.0 M).

#### 6.2.2.4.4 Recycle of draw solutions in FO

Membrane distillation was used as a downstream separator to recycle the FO draw solutions. A Sterlitech membrane testcell system with a membrane active area of 34 cm<sup>2</sup> was used to conduct the membrane distillation experiment. In this experiment, the draw solutions NaCl (4.0 M) and NaP (4.6 M) (used for pre-treated fracking wastewater using nanocomposite FO membrane) were used as feed solutions and DI water (conductivity < 15 µS) was used as the coolant in the permeate side. To conduct the experiment, the feed solution and the permeate were placed in two separate 2.0 L reservoirs. The permeate container was placed on a digital analytical balance. Each experiment was conducted for 3 h, maintaining the feed and permeate temperatures of 50°C and 20°C, respectively. Weight changes and conductivity of the permeate were monitored using the digital weight balance and a calibrated conductivity meter (Oakton, Eutech Instruments), respectively, at 30 min intervals. Initial conductivity of the feed solution was also measured using the calibrated conductivity meter (Oakton, Eutech Instruments). Concentration of the feed solution was determined using the gravimetric method at 60 min intervals during the MD experiment. Permeate flux and solute rejection (in terms of conductivity) were calculated using the following equations [197-199]:

$$J_1 = \frac{V_1}{A_{m2} \Delta t_2} \quad (6-1)$$

$$R_1(\%) = \frac{C_{f1} - C_{p1}}{C_{f1}} \times 100 \quad (6-2)$$

where  $J_1$ ,  $V_1$ ,  $A_{m2}$ ,  $\Delta t_2$ ,  $R_1$ ,  $C_{f1}$ , and  $C_{p1}$  are the permeate flux, permeated water volume, membrane effective area, measurement time, solute rejection, feed concentration and permeate concentration, respectively.

### 6.3 Results and discussion

#### 6.3.1 Characteristics of the membranes used for treatment of fracking wastewater

The characteristics of the MF membranes used for pre-treatment of fracking wastewater are exhibited in Table 6-1. The thicknesses of the nanocomposite and PSf membranes were almost identical (thickness 155 µm for nanocomposite membrane and 160 µm for PSf membrane). The

porosities of the nanocomposite and PSf membranes were also almost identical (porosity 78% for nanocomposite membrane and 75% for PSf membrane). However, the mean pore size of the nanocomposite membrane was 1.18 times lower as compared to that of the PSf membrane (mean pore size 170 nm for nanocomposite membrane and 200 nm for PSf membrane). The water contact angle of the nanocomposite membrane was 21°, while it was 2.14 times higher for the PSf membrane (water contact angle of 45°). Due to higher hydrophilicity, a much higher water permeability was obtained for the nanocomposite membrane (water permeability 4814 LMH/bar) as compared to the PSf membrane (water permeability 2728 LMH/bar).

The characteristics of the FO membranes used for desalination of fracking wastewater are also exhibited in Table 6-1. The thicknesses of the nanocomposite and the PA membranes were similar (thickness 85 μm for nanocomposite membrane and 82 μm for PA membrane). The water contact angle of the nanocomposite membrane was 14°, while it was 1.79 times higher for the PA membrane (water contact angle of 25°). Due to higher hydrophilicity, higher water permeability was obtained for the nanocomposite membrane (water permeability 4.5 LMH/bar) as compared to the PA membrane (water permeability 3.25 LMH/bar).

A MD process was used downstream to recover and recycle the draw solution in the FO process. The characteristics of the membrane used in the MD process are also provided in Table 6-1. Hydrophobic (water contact angle of 123°) and microporous (mean pore size 220 nm) PVDF membrane was used in the MD process. The thickness, porosity and tensile strength of this membrane were 158 μm, 75% and 6.5 MPa, respectively.

Table 6-1. Characteristics of the membranes in terms of thickness, porosity, mean pore size, water contact angle and water permeability.

Membrane		Thickness (μm)	Porosity (%)	Mean pore size (nm)	Water contact angle (°)	Pure water permeability (LMH/bar)
MF	Nanocomposite	155	78 ± 1.5	170	21 ± 1	4814
	PSf	160	75 ± 1	200	45 ± 2	2728
FO	Nanocomposite	85	-	-	14 ± 0.5	4.5
	PA	82	-	-	25 ± 1	3.25
MD	PVDF	158	75	220	123 ± 3	-

\* Porosity and mean pore size of PVDF membrane were obtained from product specification.

### 6.3.2 Pre-treatment of fracking wastewater by microfiltration

The pure water permeability values of the nanocomposite and PSf membranes are presented in Figure 6-1 A. It was observed that the water flux increased linearly with an increase in applied pressure from 0.28 bar to 1.38 bar. This increase was gradually attained in 0.28 bar increments. It was also observed that the value of the water permeability at each applied pressure was constant for the two types of membranes (4814 and 2728 LMH/bar for the nanocomposite and PSf membranes, respectively) (Figure 6-1 A), which indicates that no structural deformation of the membranes occurred when increasing the applied pressure. The water permeability of the nanocomposite membrane was much higher than that of the PSf membrane due to its higher hydrophilicity (Table 6-1).

Water permeability as a function of time in pre-treatment of fracking wastewater by microfiltration is presented in Figure 6-1 B and Figure 6-1 C. The initial water permeabilities were 4780 and 2710 LMH/bar for the nanocomposite and the PSf membranes, respectively (Figure 6-1 B and Figure 6-1 C). These water permeabilities decreased to 3647 LMH/bar (for the nanocomposite membrane) and 1757 LMH/bar (for the PSf membrane) at the end of the pore clogging stage. In this stage, suspended/colloidal particles block some of the pores of the membrane. During the pore clogging stage, the fouling rate largely depends on the pore size and porosity of the membrane, which cannot fully reflect the fouling properties of the membranes [101,116,178]. The fouling rate in the cake filtration stage is closely related to the structure of the cake layer formed during wastewater filtration [101,116,178]. In the fouling stage, the formation rate of the cake layer on the membrane surface is closely interrelated with the fouling rate of the membrane [101,116,178]. In this stage (fouling stage), a 29% decline in water permeability was obtained for the nanocomposite membrane while that declined was 1.59 times higher (46%) for the PSf membrane in pre-treatment of the fracking wastewater (Figure 6-1 B and Figure 6-1 C). The lower decline in water permeability in the fouling stage was seen due to higher hydrophilicity for the nanocomposite membrane as compared to the PSf membrane.

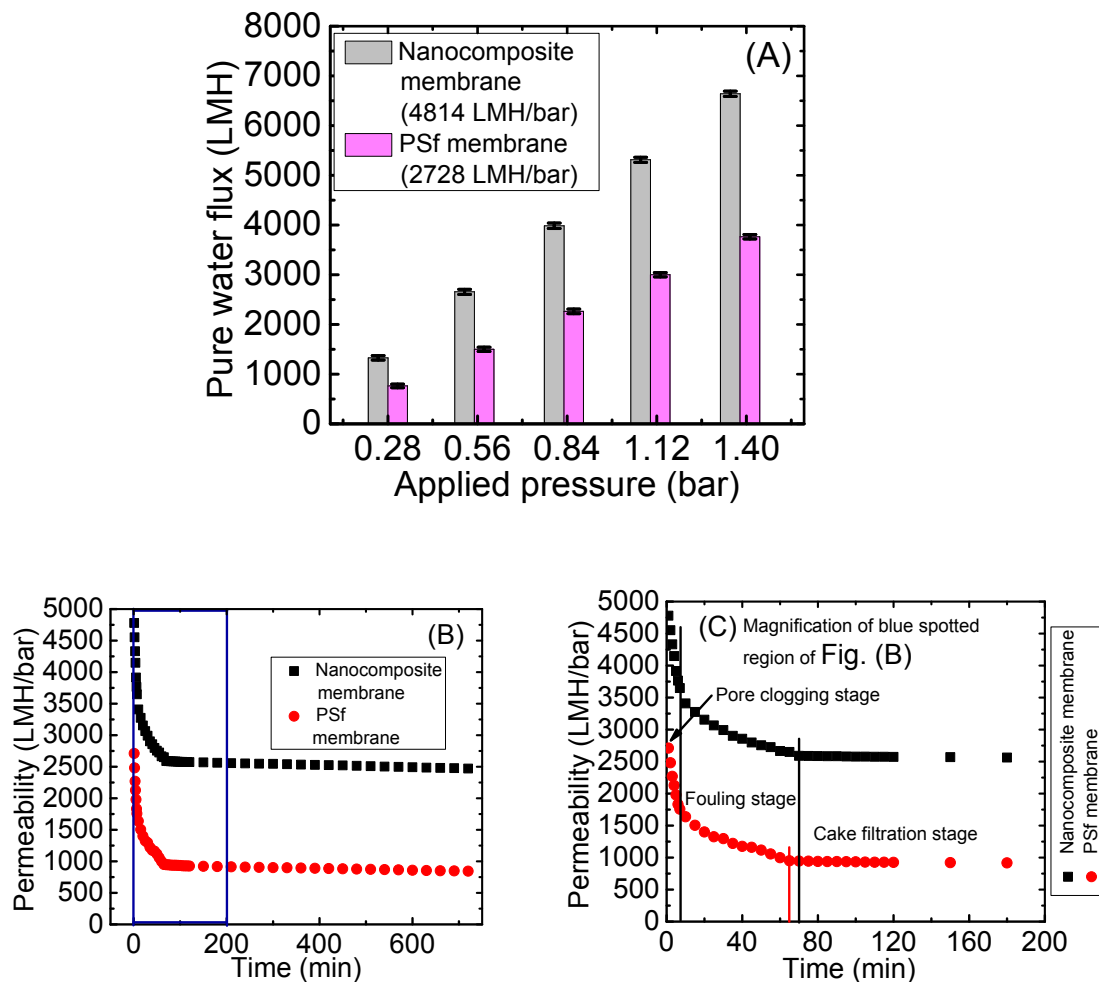


Figure 6-1. Pure water permeability for (A) nanocomposite and PSf MF membranes, and (B) permeability as a function of time for fracking wastewater using two different MF membranes (nanocomposite and polysulfone) and (C) magnification of blue spotted region of Fig. (B). [Each set of experiments was conducted three times. The average values are presented in Figure 6-1 B and Figure 6-1 C].

The  $dt/dV$  versus  $V$  filtration curves for the fouling stage in the microfiltration of fracking wastewater are showed in Figure 6-2. The specific cake resistance ( $K$ ) for the fouling stage in the microfiltration of fracking wastewater was calculated from the fitted line curves of this figure.

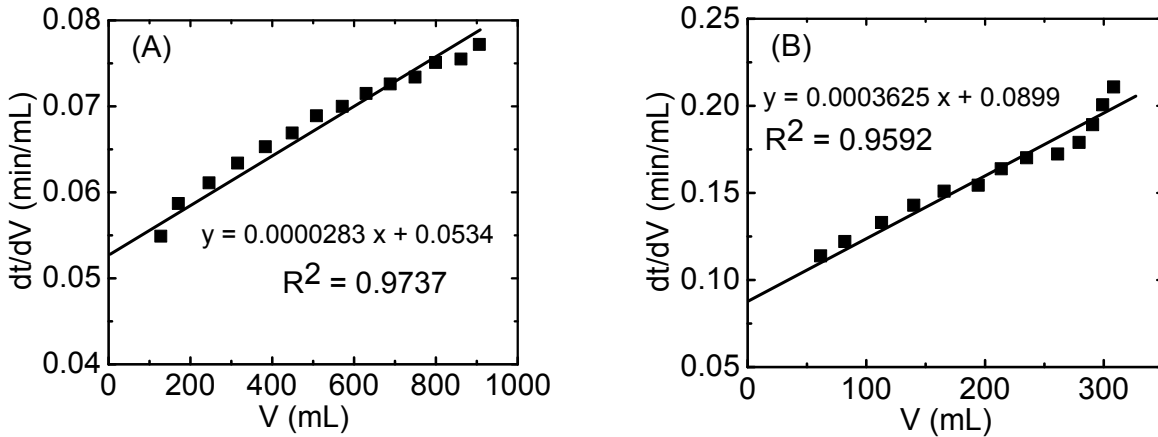


Figure 6-2. The  $dt/dV$  versus  $V$  filtration curves for fouling stage of the (A) Nanocomposite, (B) PSf membranes in the microfiltration of fracking wastewater. [After data calculation, the  $dt/dV$  versus  $V$  filtration curve was plotted and fitted with the linear regression method. The specific cake resistance was determined from the equation  $\frac{dt}{dV} = \frac{1}{q} + \frac{K}{2} V$  [101,178] where  $dV$  is the permeate volume in the time of  $dt$  and  $q$  is a constant]. [Each set of experiments was conducted three times. The average values are presented in Figure 6-2].

The specific cake resistances for the fouling stage for the nanocomposite and the PSf membranes in microfiltration of fracking wastewater are shown in Fig. 6-3 A. The specific cake resistances for the nanocomposite and the PSf membranes were  $0.57 \times 10^{-4}$  and  $7.25 \times 10^{-4}$ , respectively, in the microfiltration of the fracking wastewater (Figure 6-3 A). The membrane with a lower specific cake resistance or with higher hydrophilic properties shows better antifouling performance during the filtration of wastewater [101,178]. Due to higher hydrophilic properties, the nanocomposite membrane demonstrated lower values of specific cake resistances as compared to the PSf membrane.

The antifouling properties, in terms of water flux recovery, of the nanocomposite and the PSf membranes in microfiltration of fracking wastewater are exhibited in Figure 6-3 B and in the appendix (Table D-1, Appendix D). The increase in water flux recovery means increased antifouling propensity of a membrane. The obtained water flux recovery of the nanocomposite and PSf membranes in microfiltration of fracking wastewater were 89% and 76%, respectively (Figure 6-3 B). The higher water flux recovery of the nanocomposite membrane was achieved

due to its higher hydrophilic nature (Table 6-1) with very low values of specific cake resistance (Figure 6-3 A). The high water-flux recovery of the MF membranes demonstrated their antifouling propensity [99-101,178].

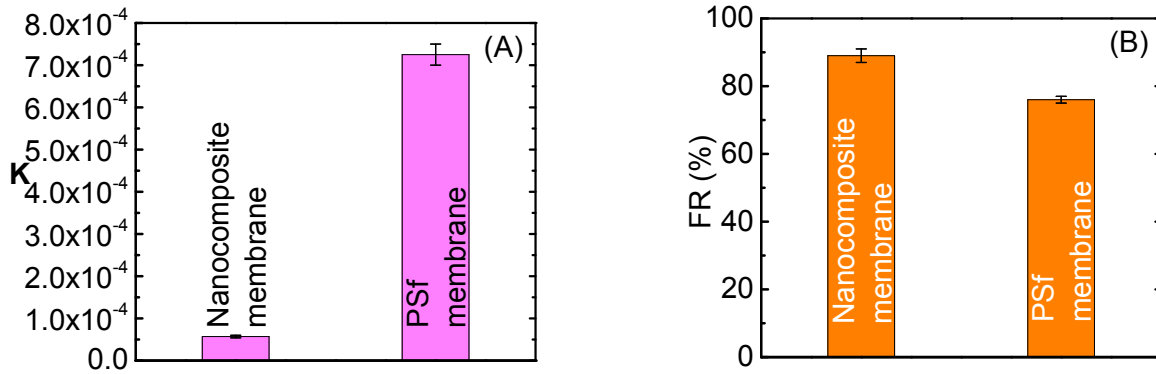


Figure 6-3. (A) Specific cake resistance for the fouling stage and (B) Flux recovery for MF membranes in the microfiltration of fracking wastewater.

The turbidity, TOC, conductivity, and pH of the fracking wastewater were 106 NTU, 853 mg/L, ~ 67 mS, and ~ 5.0, respectively, after collection of the sample (Table 6-2). The turbidity and TOC were found due to the presence of oil and dissolved organic compounds in the fracking wastewater. The turbidity was reduced to 1.6 NTU and 2 NTU by the nanocomposite and PSf membranes, respectively, after conducting microfiltration. The TOC decreased to 409 mg/L and 413 mg/L after conducting microfiltration by the nanocomposite and PSf membranes, respectively. The decrease in turbidity and TOC occurred due to the removal of oil from the fracking wastewater by microfiltration. The TOC values of 409 mg/L (for nanocomposite membrane) and 413 mg/L (for PSf membrane) after microfiltration were due to the presence of dissolved organic compounds in the wastewater. Both of the membranes (nanocomposite and PSf) removed ~52 % TOC and ~98% turbidity from the fracking wastewater by microfiltration process. The osmotic pressure of the fracking wastewater before and after microfiltration was measured and the value of this parameter was ~128.3 bar (Table 6-2).

Table 6-2. Characteristics of fracking wastewaters before and after pre-treatment by microfiltration.

Wastewater	Condition		Turbidity (NTU)	Turbidity removal (%)	TOC (mg/L)	TOC removal (%)	Conductivity (mS)	pH	Osmotic pressure (bar)
Fracking wastewater	After collection		106	-	853	-	67.3	5.0	128.4
	After MF	Using Nanocomposite membrane	1.6	98.49	409	52.05	67	4.9	128.3
		Using PSf membrane	2	98.11	413	51.58	66.9	4.8	128.3

### 6.3.3 FO performance in desalination of fracking wastewater

#### 6.3.3.1 Water flux and compositions of feed and draw solutions

Water flux through the nanocomposite and PA membrane as a function of time for the raw fracking wastewater used as feed in FO process is shown in Figure 6-4 A and Figure 6-4 B. Initial water fluxes were 18.6 and 28.3 LMH for NaCl and NaP draw solutions, respectively, when the nanocomposite membrane was used in the FO process (Figure 6-4 A). In Figure 6-4 A, declines of 55% for NaCl and 38% for NaP in terms of water flux were observed, likely due to the combined effect of membrane fouling and draw solution reverse salt flux during desalination of fracking wastewater. Compared to the nanocomposite membrane, lower initial water fluxes (13.35 LMH for NaCl and 22.2 LMH for NaP) with higher declines in water flux (69% for NaCl and 57% for NaP) were obtained for the PA membrane (Figure 6-4 B). Higher initial water fluxes with lower declines of water flux were obtained due to higher hydrophilic properties for the nanocomposite membranes as compared to the PA membrane. For both membrane, higher initial water fluxes with lower declines of water fluxes were achieved for the NaP draw solution compared to NaCl (Figure 6-4 A and Figure 6-4 B). This is likely due to higher diffusivity with lower reverse salt flux for the NaP draw solution during FO.

Water flux through the nanocomposite and PA membrane, as a function of time for the pre-treated fracking wastewater used as feed in FO process is exhibited in Figure 6-4 C and Figure 6-4 D. Slightly higher initial water fluxes were achieved (for both the FO membranes and draw solutions) for the pre-treated fracking wastewater as compared to the raw fracking wastewater used as feed in FO (Figure 6-4 A, Figure 6-4 B, Figure 6-4 C and Figure 6-4 D). The FO membranes may have fouled instantly with the raw fracking wastewater, something which did not occur for the pre-treated fracking wastewater. Thus, slightly higher initial water fluxes were obtained for the pre-treated fracking wastewater. In Figure 6-4 C and Figure 6-4 D, declines in water flux of 14% for NaCl and 4.5% for NaP were obtained for the nanocomposite membrane, while declines of 24% for NaCl and 9% for NaP were achieved for the PA membrane. Likely due to lower membrane fouling, lower declines of water fluxes were achieved for the pre-treated fracking wastewater as compared to the raw fracking wastewater used as feed in the FO experiment. The average water fluxes obtained were 19.98 LMH (for NaCl), 30.97 LMH (for NaP) and 14.39 LMH (for NaCl), 23.79 LMH (for NaP) for the nanocomposite and the PA membranes, respectively.

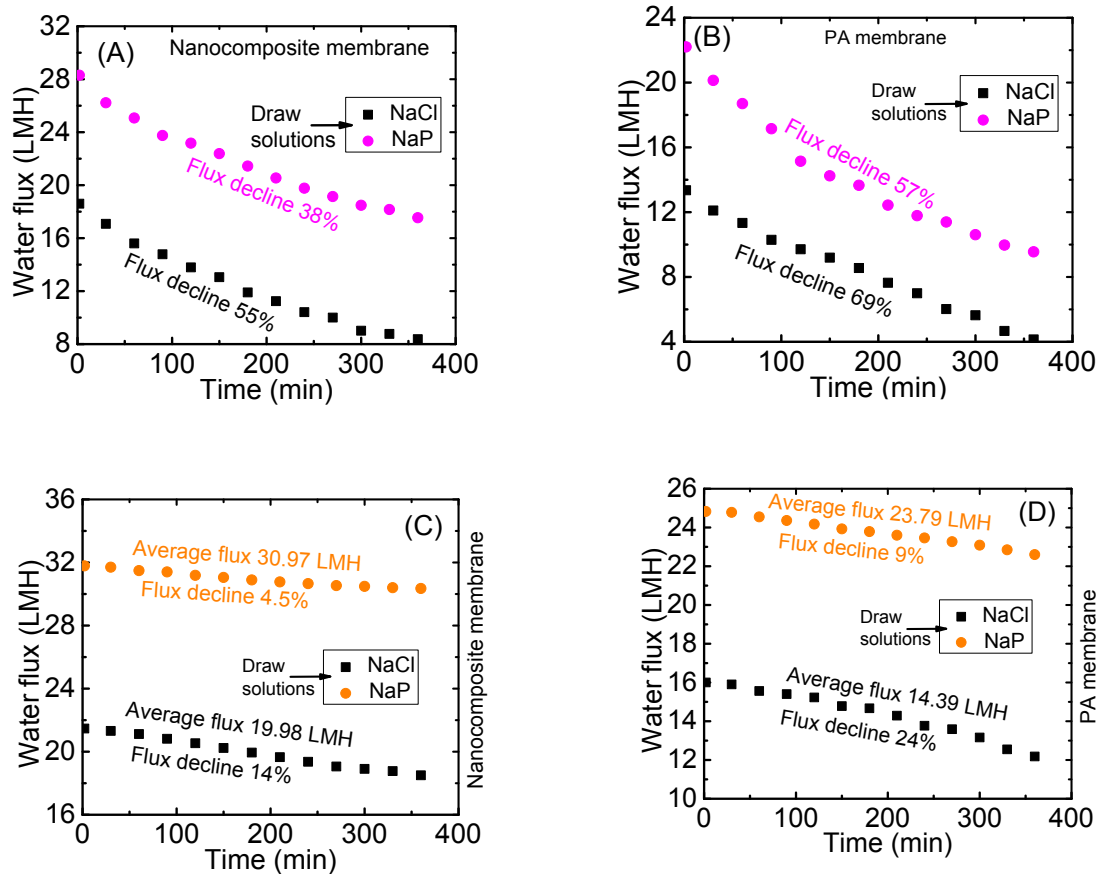


Figure 6-4. Water flux as a function of time for raw (A, B) and pre-treated (C, D) fracking wastewaters using two different FO membranes (Nanocomposite and PA). [Each set of experiments was conducted three times and the average values obtained are reported in Figure 6-4].

The composition of fracking wastewater and draw solutions in terms of TDS and TOC were investigated before and after desalination (Table 6-3). The TDS values of feed solutions were slightly higher before desalination as compared to those values after desalination when NaP was used as draw solution. The TDS values of NaP draw solution were also slightly higher after desalination as compared to those values before desalination. These observations indicate that very small quantities of solute (NaP) might pass through the membrane from feed to draw side during desalination by FO. On the other hand, TDS values of feed solutions slightly lower before desalination as compared to those values after desalination when NaCl was used as a draw solution. TDS values of the NaCl draw solution were little bit lower after desalination as

compared to those values of before desalination. These scenarios might be due to higher reverse salt flux for this draw solution as compared to the organic draw solutions. The TOC values of feed solutions were slightly higher after desalination as compared to those values before desalination for NaP draw solution. The higher TOC values obtained were likely due to reverse salt flux of the organic draw solutions during FO process. However, TOC values were almost identical before and after desalination for the NaCl draw solution, indicating greater than 99% rejection of dissolved organic compounds in fracking wastewaters during FO.

Table 6-3. TDS and TOC in the feed and draw solutions at the beginning and end of the FO experiment.

Membrane	Feed solution	Draw solution	TDS (mg/L) in feed solution		TOC (mg/L) in feed solution		TDS (mg/L) in draw solution		TOC (mg/L) in draw solution	
			Starting of FO test	End of FO test	Starting of FO test	End of FO test	Starting of FO test	End of FO test	Starting of FO test	End of FO test
Nanocomposite	Pre-treated fracking wastewater	NaCl	177952	178085	409	408	233983	233839	0	0.4
		NaP		176899		493	441848	442708	165600	165520
PA		NaCl		178116		410	233983	233796	0	0.5
NaP		176845		511		441848	442692	165600	165502	

### 6.3.3.2 Investigation of fouling behaviour for FO membranes

Fouling behaviours of the membranes after FO were investigated through FE-SEM. FE-SEM images of virgin and fouled membranes (when fracking wastewater and NaP solution were used as feed and draw, respectively) are exhibited in Figure 6-5. The surfaces of the nanocomposite and PA membranes did not contain any foulant before conducting FO desalination, however, deposition of foulants was observed after conducting the FO experiment with fracking wastewater as feed (Figure 6-5). The content of foulants on the membrane surfaces was higher due to higher concentration of foulants in the raw fracking wastewater as compared to that for the pre-treated fracking wastewater (Figure 6-5 B and Figure 6-5 C). It was also observed that fouling propensity for the nanocomposite membrane was lower than that for the PA membrane. The lower fouling tendency for the nanocomposite membrane was likely due to its higher hydrophilicity as compared to the PA membrane. While NaCl was used as draw solution, the FE-SEM images of the fouled membranes are provided in the appendix (Figure D-1, Appendix D). The FE-SEM images demonstrate that membrane fouling trends were identical for both draw solutions (NaP and NaCl).

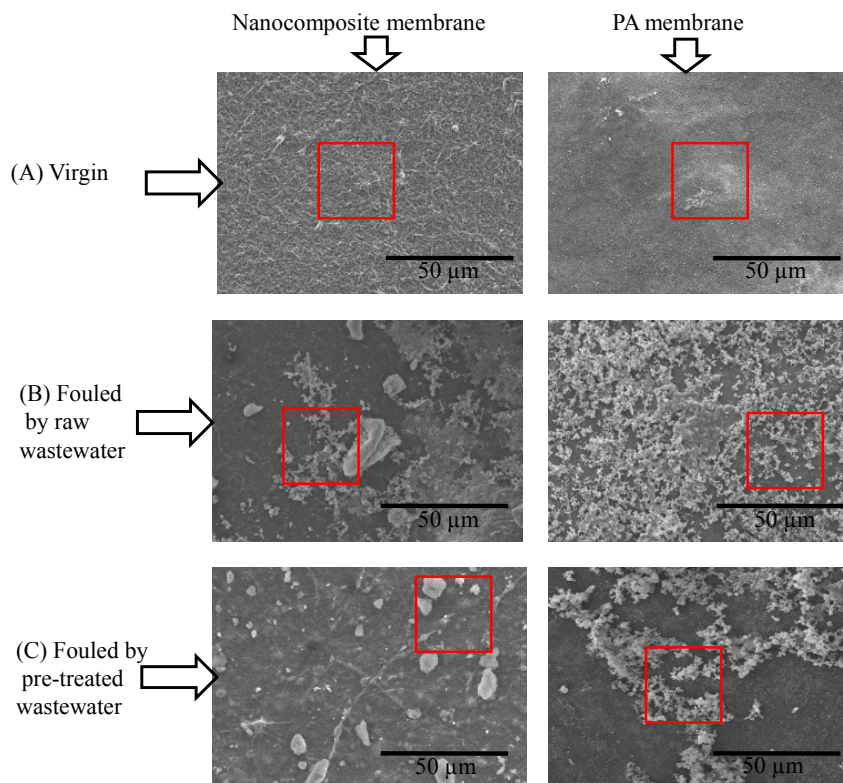


Figure 6-5. FE-SEM images for (A) virgin membranes, and fouled membranes when (B) raw and (C) pre-treated fracking wastewaters were employed as feed while NaP was used as draw solution.

Fouling behaviours of the membranes were further investigated by SEM-EDX (shown in Figure 6-6). The EDX analysis suggests the presence of C, N, O and Si atoms in the virgin nanocomposite membrane while the virgin PA membrane contained C, N and O atoms (Figure 6-6 A and Figure 6-6 B). Pt was also obtained in the EDX spectra due to the Pt coating applied to conduct the SEM analysis on the membranes. Both membranes showed new peaks for Na, Ca, Mg, K, Fe and Cl after the membrane was fouled by raw fracking wastewater (Figure 6-6 C and Figure 6-6 D). A new peak for Si, which was not seen on the virgin PA membrane, was also obtained for the PA membrane fouled by the raw fracking wastewater (Figure 6-6 D). These observations indicate that the membranes were likely fouled probably due to sand particles in wastewater, and  $\text{CaCO}_3$  and  $\text{MgCO}_3$  scale formation during desalination experiments. The peaks for Na, K, Fe and Cl were likely obtained due to crystallization of NaCl, KCl and  $\text{FeCl}_2/\text{FeCl}_3$  while the membranes were dried after fouling. The membranes might also have been fouled by organic compounds (in wastewater), which EDX cannot explain because the membranes themselves were composed of organic compounds. The peaks for Si were not observed for the PA membrane when pre-treated wastewater was used as feed (Figure 6-6 F). The sand particles were removed completely by pre-treatment, therefore, the Si-peak was not exhibited in the EDX spectrum (Figure 6-6 F). However, a Si-peak was observed for the nanocomposite membrane when pre-treated wastewater was used as feed (Figure 6-6 E). The Si-peak for this membrane was obtained due to its constituent  $\text{SiO}_2$  nanoparticles.

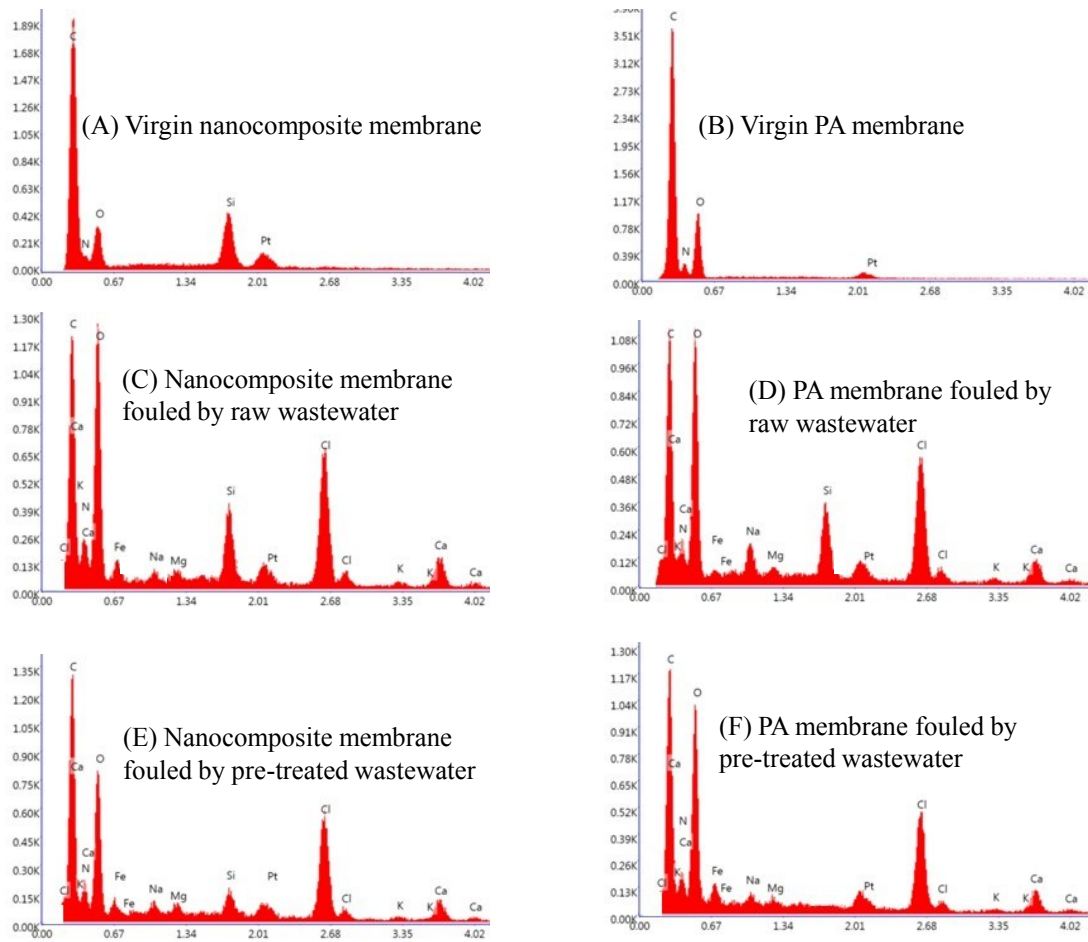


Figure 6-6. SEM-EDX spectra of (A, B) virgin membranes, and fouled membranes when (C, D) raw and (E, F) pre-treated fracking wastewaters were employed as feed while NaP was used as draw solution. (The SEM-EDX spectra were taken from the red spotted regions of Figure 6-5).

### 6.3.3.3 FO water flux recovery for pre-treated fracking wastewater as foulant

Post-desalination water flux recovery of the nanocomposite and the PA membranes was studied after treatment by FO. Water flux declined 4.5% and 9% over 6 h (with initial water fluxes of 31.78 LMH for the nanocomposite and 24.83 LMH for the PA membranes) for the nanocomposite and the PA membranes, respectively, when 4.6 M NaP was used as draw solution against pre-treated fracking wastewater (Figure 6-7 A). These declines in water flux were mostly due to membrane fouling along with draw solution reverse salt flux. The membranes were physically cleaned after conducting the desalination of fracking wastewaters

by FO. The FO water flux of the cleaned membranes was determined in order to investigate water flux recovery of the membranes. The initial water flux recovery of 98.5% (31.32 LMH) and 97% (24.08 LMH) with water flux declines of 7% and 13% over 6 h were obtained for the cleaned nanocomposite and the cleaned PA membranes, respectively (Figure 6-7 B and Figure 6-7 C). In fact, mostly inorganic fouling (scaling by  $\text{CaCO}_3$  and  $\text{MgCO}_3$ ) with only some organic fouling occurred on the membrane surface during FO desalination. FO water flux recovery data of the nanocomposite and the PA membranes, when NaCl was used as draw solution against pre-treated fracking wastewater, are exhibited in the appendix (Figure D-2, Appendix D).

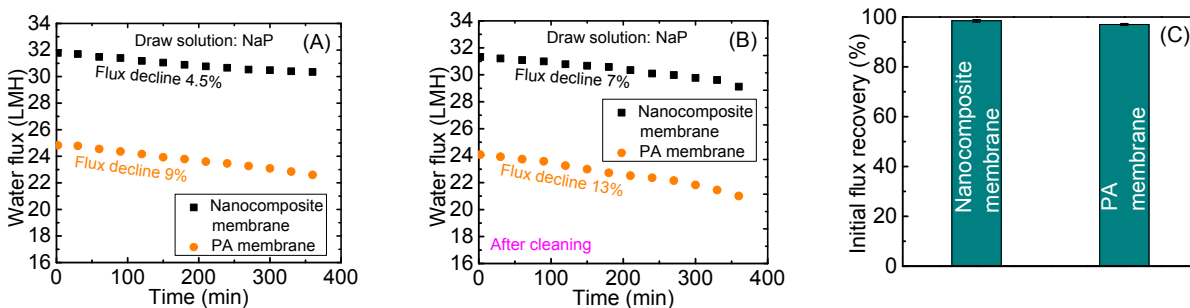


Figure 6-7. (A) Decline of water flux for the pristine membrane when 4.6 M NaP is used as draw solution against pre-treated fracking wastewater, (B) Decline of water flux after cleaning the membrane fouled by the pre-treated fracking wastewater (Draw solution: 4.6 M NaP, Feed: Pre-treated fracking wastewater), and (C) Initial FO water flux recovery after cleaning of the membrane fouled by the pre-treated fracking wastewater. [Each set of experiments was conducted three times and the average values are reported in Figure 6-7 A and Figure 6-7 B].

#### 6.3.4 Recycling draw solution in the FO using MD

The draw solutions (obtained from FO) were used as feed solutions in the MD process, by which the separation of these draw solutions was conducted in order to recycle draw solute for reuse in further FO process. In the MD process, the permeate fluxes were approximately 10.40 LMH for NaCl and 13.82 LMH for NaP where a  $\sim 99.99\%$  solute rejection rate (TDS of permeated water 23 mg/L for NaCl and 44 mg/L for NaP) was obtained for both the draw solutions (Figure 6-8 A and Figure 6-8 B). Likely, the higher permeate flux for NaP was obtained due to its lower interaction with water molecules as compared to the NaCl draw

solution. The concentrations of the draw solutions increased over time in the MD process as demonstrated in Figure 6-8 C. Since water passed from feed to permeate side, the concentration of feed solution increased as a function of time in the MD process. These concentrated feed solutions can be recycled as draw solutions in the FO process.

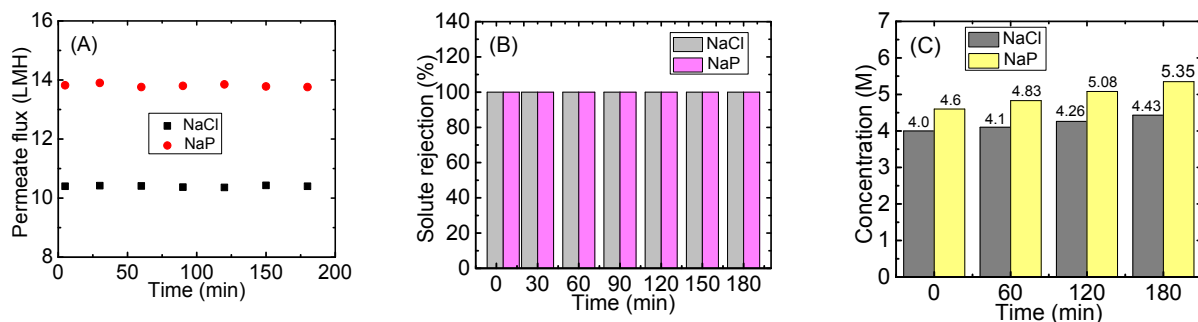


Figure 6-8. Permeate flux, (B) Permeate quality and (C) Feed concentration as a function of time in MD process in which the pre-treated fracking wastewater was used as feed with nanocomposite membrane. [Feed: Draw solutions NaCl (4.0 M) and NaP (4.6 M) obtained at the end of FO experiment used for pre-treated fracking wastewater using nanocomposite FO membrane; Feed temperature: 50 °C; Permeate temperature: 20 °C; Membrane effective area: 34 cm<sup>2</sup>]. [Each set of experiments was conducted three times with average values obtained reported in Figure 6-8].

#### 6.4. Conclusions

A combined system composed of microfiltration, forward osmosis, and membrane distillation was successfully applied for the treatment of fracking wastewater. In fact, both insoluble and soluble contaminants were removed by microfiltration and forward osmosis, respectively. Membrane distillation was used as a downstream separator to recycle FO draw solutions as well as to produce pure water. Via the pre-treatment process, about 52% of TOC and 98.5% of turbidity were removed from the fracking wastewater, which was used as the feed solution in FO process. Average FO water fluxes of 19.98 LMH for NaCl and 30.97 LMH for NaP draw solutions against pre-treated fracking wastewater as feed solution were obtained when using a nanocomposite membrane, while these water fluxes were 14.39 LMH for NaCl and 23.79 LMH for NaP draw solutions when using a PA membrane. High solute rejection was obtained by both membranes (nanocomposite and PA) in the FO treatment of pre-treated fracking

wastewater. This research also demonstrated that 98.5% and 97% of initial water flux can be recovered by the nanocomposite and PA membranes, respectively, after desalination of fracking wastewater. In membrane distillation, permeate fluxes were about 10.40 LMH for NaCl and about 13.82 LMH for NaP with approximately 99.99% solute rejection, producing treated water with TDS 23-44 mg/L. This result indicates a successful implementation of membrane distillation as a downstream separator in the FO process. Therefore, the combined MF-FO-MD process has major potential to be used for the treatment of high salinity waste streams such as fracking wastewater.

#### Acknowledgements

Md. Saifur Rahaman gratefully acknowledges the FRQNT for providing the funding support for this project. Md. Shahidul Islam acknowledges the support of a doctoral-level scholarship from the FRQNT. The authors also acknowledge supports from the NSERC and Concordia University, Canada.

## **Chapter 7: Contributions, Conclusions and Recommendations for Future Work**

### 7.1 Contributions

In this study, two novel, highly-effective membrane materials were synthesized, characterized and evaluated for their performance in practical applications: PVAc-coated electrospun nylon 6/SiO<sub>2</sub> composite MF membrane and electrospun nylon 6/SiO<sub>2</sub> composite supported TFC FO membrane with a polyamide/SiO<sub>2</sub> composite active layer. A comprehensive study into the selection of novel, highly-effective organic draw solutions for the desalination of fracking wastewater by FO process was also conducted for the first time. Finally, MF was tested for the first time as a pre-treatment process, using the fabricated MF membrane, along with FO, using the fabricated TFC membrane, as a post-treatment process for the desalination of highly saline fracking wastewaters. The identified organic draw solutions were used in the FO process for desalination of the fracking wastewaters. In the pre-treatment stage, ~ 98.5% turbidity and ~ 52% TOC were removed from the fracking wastewater by the MF process. Finally, treated water with TDS 23-44 mg/L was obtained from the pre-treated fracking wastewater by the combined process consisted of FO and MD.

From this work, four journal articles are expected with one already having been published in a well reputed journal in our field of research. The list of the articles (published, submitted, and in preparation) are provided below:

1. M. S. Islam, J. R. McCutcheon, M. S. Rahaman, A high flux polyvinyl acetate-coated electrospun nylon 6/SiO<sub>2</sub> composite microfiltration membrane for the separation of oil-in-water emulsion with improved antifouling performance, *J. Membr. Sci.* 537 (2017) 297–309 (Published).
2. M. S. Islam, M. S. Rahaman, Forward Osmosis Treatment of Fracking Wastewaters: Evaluation of Suitable Organic Draw Solutions (Submitted).
3. M. S. Islam, J. R. McCutcheon, M. S. Rahaman, Silica Nanoparticle Containing Novel Thin-Film Composite Forward Osmosis Membrane with High Flux and Antifouling Properties (In Preparation).
4. M. S. Islam, M. S. Rahaman, Performance of Combined MF-FO-MD processes for Fracking Wastewater Treatment (In Preparation).

Presentation has been made at scientific conferences to present the research work which was conducted during my Ph.D. studies. The list of all conferences is provided below:

1. M. S. Islam, S. Sultana, M. S. Rahaman, “Renewable Energy Generation through Osmotic Heat Engine”, 12<sup>th</sup> International Conference on Mechanical Engineering, ICME 2017, December 20-22, 2017, BUET, Dhaka, Bangladesh.
2. M. S. Islam, S. Sultana, M. S. Rahaman, “Highly Effective Microfiltration Membrane Based on Electrospun Nylon 6/SiO<sub>2</sub> Composite”, Gordon Research Conference, July 31 - August 5, 2016, New London, NH, USA.
3. M. S. Islam, M. S. Rahaman, “Electrospun Nylon 6 Microfiltration Membrane for Treatment of Brewery Wastewater”, 11<sup>th</sup> International Conference on Mechanical Engineering, ICME 2015, December 18-20, 2015, BUET, Dhaka, Bangladesh.
4. M. S. Islam, M. Lemieux, M. S. Rahaman, “Effective organic draw solutes for engineered osmosis processes”, 250<sup>th</sup> ACS National Meeting and Exposition, August 16-20, 2015, Boston, Massachusetts, USA.
5. M. S. Islam, M. S. Rahaman, “Highly porous superhydrophilic ultra-filtration membrane based on electrospun Nylon 6/SiO<sub>2</sub> composite”, North American Membrane Society (NAMS) annual conference, May 30-June 03, 2015, Boston, Massachusetts, USA.
6. M. S. Islam, M. S. Rahaman, “Preparation & characterization of polymer/CNT composite nanoparticles and nanofibers through electrospinning”. CSCE-2014 Annual Conference, Halifax, Nova Scotia.
7. A. Meikleham, M. S. Islam, M. S. Rahaman, Electorowicz, M., “Removal of Emerging Contaminants from Wastewater Effluents Using Nano-Composite Electrochemical Filters”. CSCE-2014 Annual Conference, Halifax, Nova Scotia.

## 7.2 Conclusions

Today, a huge quantity of highly saline wastewater (about 37 billion cubic feet/day) is released during the hydraulic fracturing process, a technology growing in use in a rapidly growing shale gas industry. The management of the released fracking wastewater is a serious challenge because of its harmful consequences to public health and to the environment at large. This highly saline fracking waster also contains sand and oil as suspended solids. In order to re-cycle the fracking wastewater, these suspended and dissolved solids can be removed by pre- and post-treatment of the fracking wastewater. Sand particles and oil can be removed from the fracking wastewater by microfiltration as a pre-treatment step. As a post-treatment process, FO, coupled with membrane distillation as downstream separator for draw solution recovery, can be

used to desalinate the highly saline pre-treated fracking wastewater. Identification of effective draw solutions, the fabrication of a novel MF membrane with high water flux, high rejection and antifouling properties, and the fabrication of a novel FO membrane with high water flux, high rejection and antifouling properties were performed in order to optimize the FO process for successful treatment of fracking wastewater. In this research, seven potentially effective draw solutions were preselected for FO, with four of them demonstrated to be effective in treating the highly saline fracking wastewater. A high water flux polyvinyl acetate-coated electrospun nylon 6/SiO<sub>2</sub> composite MF membrane was fabricated and its performance has been tested in regards to water flux, oil rejection, and antifouling properties. This membrane exhibited better results than those seen with the commercially available MF membranes currently used for the same application. In the next step of this research, a high water-flux membrane with high rejection and antifouling properties was fabricated and characterized for use in FO. Finally, the fracking wastewaters were pre-treated using MF and then post-treated using FO coupled with membrane distillation using the membranes fabricated. This combined MF-FO-MD process yielded water with TDS 23-44 mg/L from the highly saline fracking wastewater. Literature demonstrates that the standard TDS values are 0 - 1000 mg/L for fresh water, 1000 - 10,000 mg/L for brackish water and > 10,000 mg/L for saline water [201-202]. As it is demonstrated that TDS contents after treatment of fracking wastewaters by the combined MF/FO/MO process were in between 23 - 44 mg/L. This result revealed fresh water was obtained after treatment of highly saline fracking wastewaters. Most water used in hydraulic fracturing comes from surface water sources like lakes, rivers, aquifers, and municipal supplies [203]. Therefore, treated water coming from fracking wastewater can be reused for hydraulic fracturing as well as in utility sector. This treated water can also be reused for agricultural purpose in the areas very close to hydraulic fracturing industry.

The concentrated feed solution obtained from FO unit used in the combined MF/FO/MO process could be managed by disposing to evaporation pond. A geomembrane liner would be required to hinder seepage into ground in the pond. The area and depth of the pond should be designed by considering evaporation rate as compared to the volume of concentrated feed solution discharge. The salt residue after evaporation of water can be removed at regular time period to enlarge the pond's life. The residue is mainly NaCl, which can be used as raw materials in chlor-alkali industry and soda-ash industry.

### 7.3 Recommendations for future work

In this thesis, the following research was conducted:

(a) Fabrication of A High Flux Polyvinyl Acetate-coated Electrospun Nylon 6/SiO<sub>2</sub> Composite Microfiltration Membrane for the Separation of Oil-in-Water Emulsion with Improved Antifouling Performance, (b) Evaluation of Suitable Organic Draw Solutions for Forward Osmosis Treatment of Fracking Wastewaters, (c) Fabrication of Silica Nanoparticle Containing Novel Thin-Film Composite Forward Osmosis Membrane with High Flux and Antifouling Properties, and (d) Performance of Combined MF-FO-MD processes for Fracking Wastewater Treatment.

The following research can be conducted in the future:

(a) Various pre-treatment methods for FO treatment of fracking wastewater

In this thesis, the only pre-treatment method used was microfiltration. In the future, various pre-treatment methods, such as ultrafiltration, coagulation, flocculation, electrocoagulation, and electrooxidation should be evaluated for use with fracking wastewater with performance between these methods and microfiltration then compared.

(b) Treatment of other saline wastewaters

In this thesis, the combined MF-FO-MD process was applied only to treat highly saline fracking wastewater. Treated water with TDS 23-44 mg/L was obtained by this combined process. Saline wastewaters are produced by a number of industries, such as food, leather, and petroleum production [200]. In future work, the combined MF-FO-MD process should be applied to treat the saline wastewaters released from these industries in order to compare the removal capacity for a wider variety of compounds.

(c) Fabrication of a highly effective membrane for the membrane distillation process

In this thesis, membrane distillation was used as a downstream separator in order to recover the draw solutions used in the FO process. Membrane distillation is a thermally driven process in which water vapor passes through a non-wetted microporous hydrophobic membrane. The driving force behind this process is the vapor pressure gradient, which is generated by a temperature difference across the membrane. However, fouling and wetting are major concerns for the membrane currently used for this process. In fact, fouling and wetting decrease permeate flux and permeate quality, respectively. Therefore, a novel, highly-effective membrane for membrane distillation process should be fabricated and evaluated in future work.

A highly effective membrane for this process could be fabricated via electrospinning using polymers such as polyvinylidene fluoride, pentafluorostyrene, polystyrene, or poly( $\epsilon$ -caprolactone) with fluoroalkylsilanes, and nanoparticles such as hydrophobic silica, cerium(IV) dioxide, or graphene.

(d) Synthesis of magnetic nanoparticles as draw solutions for FO process

As discussed earlier, membrane distillation was used as a downstream separator to recycle draw solutions used in the FO process. However, fouling and wetting are two key concerns identified with the membranes used in membrane distillation. Therefore, the researchers are searching for a feasible alternative downstream separation technique. Magnetic separation can be used as a feasible downstream technique, however, this can only be used for magnetic draw solutions. Effective magnetic draw solutions for FO process should be synthesized for evaluation in future research. It is necessary to note that the synthesized draw solutions must also be suitable for FO treatment of highly saline fracking wastewater.

(e) Scale up of the combined MF/FO/MD process

A new combined MF/FO/MD process has been applied for treatment of fracking wastewater in this research. Each step of the combined process was used separately for treatment of the fracking wastewaters in this study. In future research, a continuous process composed of MF, FO MD can be studied to scale up this combined process.

## References

- [1] <http://www.bbc.com/news/uk-14432401>, 16 December 2015, UK.
- [2] <https://www.lenntech.com/microfiltration-and-ultrafiltration.htm>.
- [3] <https://www.bing.com/images/search?q=Microfiltration+process+image&id>.
- [4] Z. Caineng, *Shale gas unconventional petroleum geology*, London: Elsevier (2013) 149–190.
- [5] L. Jeffrey, H. Garvin, M. Jordan, P. Elizabeth, B. William, C. Ken, *Natural gas and the transformation of the U.S. energy sector: electricity*, Golden, CO: NREL/TP-6A50-55538 (2012).
- [6] D. John, *The good news about gas: the natural gas revolution and its consequences*, *Foreign Aff.* (2011) 82–93.
- [7] U.S. EIA. *Annual energy outlook*, Washington, DC: U.S. Department of Energy (2013).
- [8] International Energy Agency, *Golden rules for a golden age of gas*, Paris: OECD (2012).
- [9] U.S. EIA. *World shale gas resources: an initial assessment of 14 regions outside the United States*, Washington, DC: U.S. Department of Energy (2011).
- [10] B. Chuck, C. Bill, J. Valerie, L. Rick, M. Camron K., *Shale gas: a global resource oil field review*, 23 (3) (2011) 28–39.
- [11] E. Diamanti-Kandarakis, J. P. Bourguignon, L. C. Giudice, *Endocrine disrupting chemicals: an Endocrine Society scientific statement*, *Endocr. Rev.* 30 (4) (2009) 293–342.
- [12] M. Chris, *Energy: the truth about fracking*, *Sci. Am.* (2011) 80–85.
- [13] United States Energy Information Administration, *Annual Energy Outlook*; United States Department of Energy: Washington, DC (2012).
- [14] Independent Statistics & Analysis, U. S. Energy Information Administration, [https://www.eia.gov/dnav/ng/ng\\_prod\\_shalegas\\_s1\\_a.htm](https://www.eia.gov/dnav/ng/ng_prod_shalegas_s1_a.htm).
- [15] S. L. Susan, *The global shale gas initiative*, *Houst J. Int. Law* 33 (2011) 369–417.
- [16] [https://www.earthworksaction.org/issues/detail/hydraulic\\_fracturing\\_101#.Wdjwn1tSzIU](https://www.earthworksaction.org/issues/detail/hydraulic_fracturing_101#.Wdjwn1tSzIU).
- [17] S. M. Olmstead, L. A. Muehlenbachs, J.-S. Shih, Z. Chu, A. J. Krupnick, *Shale gas development impacts on surface water quality in Pennsylvania*, *Proc. Natl. Acad. Sci. U.S.A.* 110 (13) (2013) 4962–4967.

- [18] Ground Water Protection Council, ALL Consulting. Modern Shale Gas Development in the United States: A Primer; United States Department of Energy, Office of Fossil Energy: Washington, D.C. (2009) 96.
- [19] K. B. Gregory, R. D. Vidic, D. A. Dzombak, Water Management Challenges Associated with the Production of Shale Gas by Hydraulic Fracturing, *Elements* 7 (3) (2011) 181–186.
- [20] R. D. Vidic, S. L. Brantley, J. M. Vandebosche, D. Yoxtheimer, J. D. Abad, Impact of Shale Gas Development on Regional Water Quality, *Sci.* 340 (6134) (2013) 826–835.
- [21] A. K. Richard, Natural gas from shale bursts onto the scene, *Sci.* 328 (2010) 1624–1626.
- [22] B. K. Sovacool, Cornucopia or curse? Reviewing the costs and benefits of shale gas hydraulic fracturing (fracking), *Renewable Sustainable Ener. Rev.* 37 (2014) 249–264.
- [23] Sun, T. Paul, C. L. Meyer, C. Kuijvenhoven, S. Padmasiri, V. Fedotov, “Treatment of water from fracturing operation for unconventional gas production,” in *Contemporary Technologies for Shale-Gas Water and Environmental Management*, Ronald D. Neufeld, editor. Alexandria, Va.: Water Environment Federation, (2012) 61–81.
- [24] D. L. Shaffer, L. H. A. Chavez, M. Ben-Sasson, S. R.-V. Castrillon, N. Y. Yip, M. Elimelech, Desalination and reuse of high-salinity shale gas produced water: Drivers, Technologies, and Future Directions, *Environ. Sci. Technol.* 47 (2013) 9569–9583.
- [25] G. B. Kelvin, V. D. Radisav, D. A. David, Water management challenges associated with the production of shale gas by hydraulic fracturing, *Elements* 7 (2011) 181–186.
- [26] <http://www.npr.org/2013/07/11/200515289/wastewater-wells-geothermal-power-triggering-earthquakes>.
- [27] A. Koren, N. Nadav, Mechanical vapour compression to treat oil field produced water, *Desalination* 98 (1–3) (1994) 41–48.
- [28] J. M. Veza, Mechanical Vapor Compression Desalination Plants- a Case-Study, *Desalination* 101 (1) (1995) 1–10.
- [29] Z. Zimerman, Development of Large-Capacity High-Efficiency Mechanical Vapor Compression (MVC) Units, *Desalination* 96 (1–3) (1994) 51–58.
- [30] L. R. Evans, J. E. Miller, Sweeping gas membrane desalination using commercial hydrophobic hollow fiber membranes, SAND report, SAND 2002- 0138, Unlimited Release, Printed January, 2002.

- [31] F. Lokiec, A. Ophir, The Mechanical Vapor Compression: 38 Years of Experience. IDA World Congress, Maspalomas, Gran Canaria, Spain, October 21–26, 2007.
- [32] F. Al-Juwayhel, H. El-Dessouky, H. Ettouney, Analysis of single-effect evaporator desalination systems combined with vapor compression heat pumps, *Desalination* 114 (3) (1997) 253–275.
- [33] J. Crittenden, R. Trussell, D. Hand, K. Howe, G. Tchobanoglous, *Water Treatment Principles and Design* (2005), Edition 2, John Wiley and Sons, New Jersey.
- [34] <https://socratic.org/questions/what-is-the-difference-between-osmosis-and-reverse-osmosis>.
- [35] M. Elimelech, W.A. Phillip, The future of seawater desalination: energy, technology, and the environment, *Science* 333 (2011) 712–717.
- [36] B. Jiao, A. Cassano, E. Drioli, Recent advances on membrane processes for the concentration of fruit juices: a review, *J. Food Eng.* 63 (2004) 303-324.
- [37] K.-V. Peinemann, S. P. Nunes, L. Giorno, (Eds.). *Membrane Technology: Volume 3: Membranes for Food Applications*, Wiley-VCH Verlag GmbH & Co. KGaA, Germany (2010).
- [38] K. W. Lawson, D. R. Lloyd, Membrane distillation, *J. Membr. Sci.* 124 (1) (1997) 1–25.
- [39] M. S. El-Bourawi, Z. Ding, R. Ma, M. Khayet, A framework for better understanding membrane distillation separation process, *J. Membr. Sci.* 285 (1–2) (2006) 4–29.
- [40] M. Khayet, T. Matsuura, *Membrane distillation: principles and applications*; Elsevier: Oxford, 2011.
- [41] M. R. Qtaishat, F. Banat, Desalination by solar powered membrane distillation systems, *Desalination* 308 (2013) 186–197.
- [42] T. Ruprakobkit, L. Ruprakobkit, C. Ratanatamskul, Carboxylic acid concentration by forward osmosis processes: Dynamic modeling, experimental validation and simulation, *Chem. Eng. J.* 306 (2016) 538-549.
- [43] J. C. Ortega-Bravo, G. Ruiz-Filippi, A. Donoso-Bravo, I. E. Reyes-Caniupán, D. Jeison, Forward osmosis: Evaluation thin-film-composite membrane for municipal sewage concentration, *Chem. Eng. J.* 306 (2016) 531-537.
- [44] S. Lee, C. Boo, M. Elimelech, S. Hong, Comparison of fouling behavior in forward osmosis (FO) and reverse osmosis (RO), *J. Membr. Sci.* 365 (1–2) (2010) 34–39.

- [45] B. X. Mi, M. Elimelech, Organic fouling of forward osmosis membranes: Fouling reversibility and cleaning without chemical reagents, *J. Membr. Sci.* 348 (1–2) (2010) 337–345.
- [46] A. Tiraferri, Y. Kang, E. P. Giannelis, M. Elimelech, Superhydrophilic Thin-Film Composite Forward Osmosis Membranes for Organic Fouling Control: Fouling Behavior and Antifouling Mechanisms, *Environ. Sci. Technol.* 46 (20) (2012) 11135–11144.
- [47] S. Loeb, The Loeb-Sourirajan Membrane: How It Came About, *American Chemical Society*, 153 (0) (1981) 1-9.
- [48] J. R. McCutcheon, M. Elimelech, Influence of membrane support layer hydrophobicity on water flux in osmotically driven membrane processes, *J. Membr. Sci.* 318 (1-2) (2008) 458-466.
- [49] J. R. McCutcheon, R. L. McGinnis, M. Elimelech, A novel ammonia-carbon dioxide forward (direct) osmosis desalination process, *Desalination* 174 (1) (2005) 1-11.
- [50] B. Mi, M. Elimelech, Chemical and physical aspects of organic fouling of forward osmosis membranes, *J. Membr. Sci.* 320 (1-2) (2008) 292-302.
- [51] C. Klaysom, T. Y. Cath, T. Depuydt, I. F. J. Vankelecom, Forward and pressure retarded osmosis: potential solutions for global challenges in energy and water supply, *Chem. Soc. Rev.* 42 (16) (2013) 6959-6989.
- [52] N. Lior, G. Amy, A. Z. Barak, A. Chakraborty, A. E. Nashar, Y. El-Sayed, M. D. Kennedy, A. Kumano, S. Lattemann, *Advances in Water Desalination*, vol. 1. (2013) John Wiley & Sons Inc., Hoboken, New Jersey.
- [53] M. Mulder, *Basic Principles of Membrane Technology*, 1996, second ed. Kluwer Academic Publishers.
- [54] C. Boo, Y. F. Khalil, M. Elimelech, Performance evaluation of trimethylamine-carbon dioxide thermolytic draw solution for engineered osmosis, *J. Membr. Sci.* 473 (2015) 302–309.
- [55] A. Achilli, T. Y. Cath, A. E. Childress, Selection of inorganic-based draw solutions for forward osmosis applications, *J. Membr. Sci.* 364 (2010) 233–241.
- [56] R. L. McGinnis, J. R. McCutcheon, M. Elimelech, A novel ammonia-carbon dioxide osmotic heat engine for power generation, *J. Membr. Sci.* 305 (2007) 13–19.

- [57] K. L. Hickenbottom, J. Vanneste, T. Y. Cath, Assessment of alternative draw solutions for optimized performance of a closed-loop osmotic heat engine, *J. Membr. Sci.* 504 (2016) 162–175.
- [58] America's Authority in Membrane Treatment, Pre-treatment for Membrane Processes, American Membrane Technology Association (AMTA), F-12, February 2007.
- [59] H. Shi, Y. He, Y. Pan, H. Di, G. Zeng, L. Zhang, C. Zhang, A modified mussel-inspired method to fabricate TiO<sub>2</sub> decorated superhydrophilic PVDF membrane for oil/water separation, *J. Membr. Sci.* 506 (2016) 60–70.
- [60] D. Liu, J. Zhu, M. Qiu, C. He, Antifouling performance of poly(lysine methacrylamide)-grafted PVDF microfiltration membrane for solute separation, *Separ. Purif. Technol.* 171 (2016) 1–10.
- [61] J.A. Prince, S. Bhuvana, V. Anbharasi, N. Ayyanar, K.V.K. Boodhoo, G. Singh, Ultra-wetting graphene-based PES ultrafiltration membrane – A novel approach for successful oil-water separation, *Water research* 103 (2016) 311-318.
- [62] S. Kumar, A. Mandal, C. Guria, Synthesis, characterization and performance studies of polysulfone and polysulfone/polymer-grafted bentonite based ultrafiltration membranes for the efficient separation of oil field oily wastewater, *Process Safety Environ. Protection* 102 (2016) 214-228.
- [63] <https://filtisol.com/main/index.php/technical-info/ccdb-filtration-technique>.
- [64] M. S. Islam, M. S. Rahaman, J. H. Yeum, Phosphine-functionalized electrospun poly(vinyl alcohol)/silica nanofibers as highly effective adsorbent for removal of aqueous manganese and nickel ions, *J. Colloid Sur. A: Physicochem. Eng. Asp.* 484 (5) (2015) 9-18.
- [65] M. S. Islam, M. S. Rahaman, J. H. Yeum, Electrospun novel super-absorbent based on polysaccharide–polyvinyl alcohol–montmorillonite clay nanocomposites, *Carbohydrate Polym.* 115 (2015) 69-77.
- [66] M. Li, D. Wang, R. Xiao, G. Sun, Q. Zhao, H. Li, A novel high flux poly (trimethylene terephthalate) nanofiber membrane for microfiltration media, *Sep. Purif. Technol.* 116 (2013) 199–205.
- [67] B. Ramalingam, S. Subramanian, R. Seeram, Recent trends in nanofibrous membranes and their suitability for air and water filtrations, *Membr.* 1 (2011) 232–248.

- [68] R. Wang, Y. Liu, B. Li, B. S. Hsiao, Electrospun nanofibrous membranes for high flux microfiltration, *J. Membr. Sci.* 392–393 (2012) 167–174.
- [69] M. Zhua, G. Xua, M. Yua, Y. Liua, R. Xiaoa, Preparation, properties, and application of polypropylene micro/nanofiber membranes, *Polym. Adv. Technol.* 23 (2012) 247–254.
- [70] L. Li, L. Ding, Z. Tu, Y. Wan, D. Clause, J. Lanoisellé, Recovery of linseed oil dispersed within an oil-in-water emulsion using hydrophilic membrane by rotating disk filtration system, *J. Membr. Sci.* 342 (2009) 70–79.
- [71] K. Bensadok, M. Belkacem, G. Nezzal, Treatment of cutting oil/water emulsion by coupling coagulation and dissolved air flotation, *Desalination* 206 (2007) 440–448.
- [72] J. Zhong, X. Sun, C. Wang, Treatment of oily wastewater produced from refinery processes using flocculation and ceramic membrane filtration, *Sep. Purif. Technol.* 32 (2003) 93–98.
- [73] E. R. Binner, J. P. Robinson, S. W. Kingman, E. H. Lester, B. J. Azzopardi, G. Dimitrakis, J. Briggs, Separation of oil/water emulsions in continuous flow using microwave heating, *Energy Fuels* 27 (2013) 3173–3178.
- [74] Z. L. Kiss, L. Kocsis, G. K. Szabó, C. Hodúr, Z. László, Treatment of oily wastewater by combining ozonation and microfiltration, *Desalin. Water Treat.* 6 (2014) 1–8.
- [75] L. J. Stacka, P. A. Carney, H. B. Malone, T. K. Wessels, Factors influencing the ultrasonic separation of oil-in-water emulsions, *Ultrason. Sonochem.* 12 (2005) 153–160.
- [76] T. Darvishzadeh, V. V. Tarabara, N. V. Priezjev, Oil droplet behavior at a pore entrance in the presence of crossflow: implications for microfiltration of oil- water dispersions, *J. Membr. Sci.* 447 (2013) 442–451.
- [77] M. Hemmati, F. Rekabdar, A. Gheshlaghi, A. Salahi, T. Mohammadi, Effects of air sparging, cross flow velocity and pressure on permeation flux enhancement in industrial oily wastewater treatment using microfiltration, *Desalin. Water Treat.* 39 (2012) 33–40.
- [78] A. K. Gautam, C. La, H. Fong, T. J. Menkhaus, Electrospun polyimide nanofiber membranes for high flux and low fouling microfiltration applications, *J. Membr. Sci.* 466 (2014) 142–150.
- [79] Y. Liu, R. Wang, H. Ma, B. S. Hsiao, B. Chu, High-flux microfiltration filters based on electrospun polyvinyl alcohol nanofibrous membranes, *Polym.* 54 (2013) 548–556.

- [80] F. E. Ahmed, B. S. Lalia, R. Hashaikeh, A review on electrospinning for membrane fabrication: Challenges and applications, *Desalination* 356 (2015) 15–30.
- [81] G.-B. Yin, Analysis of Electrospun Nylon 6 Nanofibrous Membrane as Filters, *J. Fiber Bioeng. Informat.*, 3 (2010) 137-141.
- [82] H. R. Pant, M. P. Bajgai, C. Yi, R. Nirmala, K. T. Nam, W. Baek, H. Y. Kim, Effect of successive electrospinning and the strength of hydrogen bond on the morphology of electrospun nylon-6 nanofibers, *Colloid Surf. A: Physicochem. Eng. Asp.* 370 (2010) 87-94.
- [83] H. Dong, P. Ye, M. Zhong, J. Pietrasik, R. Drumright, K. Matyjaszewski, Superhydrophilic surfaces vis polymer-SiO<sub>2</sub> nanocomposites, *Langmuir* 26 (2010) 15567-15573.
- [84] B. G. Trewyn, J. A. Nieweg, Y. Zhao, Lin, V. S.-Y. Lin, Biocompatible mesoporous silica nanoparticles with different morphologies for animal cell membrane penetration, *Chem. Eng. J.* 137 (2007) 23–29.
- [85] J. Yang, J. Zhao, Preparation and mechanical properties of silica nanoparticles reinforced composite hydrogels, *Mater. Lett.* 120 (2014) 36-38.
- [86] J. Ahmad, M.-B. Hagg, Preparation and characterization of polyvinyl acetate/zeolite 4A mixed matrix membrane for gas separation, *J. Membr. Sci.* 427 (2013) 73-84.
- [87] B. D. Freeman, H. B. Park, B. D. McCloskey, Water purification membranes with improved fouling resistance, *US8017050 B2*, Sep 13, 2011.
- [88] M. Liu, J. Li, Z. Guo, Polyaniline coated membranes for effective separation of oil-in-water emulsions *J. Colloid Interface Sci.* 467 (2016) 261-270.
- [89] M. Zare, F. Z. Ashtiani, A. Fouladitajar, CFD modeling and simulation of concentration polarization in microfiltration of oil–water emulsions; Application of an Eulerian multiphase model, *Desalination* 324 (2013) 37–47.
- [90] H. Lotfiyan, F. Z. Ashtiani, A. Fouladitajar, S. B. Armand, Computational fluid dynamics modeling and experimental studies of oil-in-water emulsion microfiltration in a flat sheet membrane using Eulerian approach, *J. Membr. Sci.* 472 (2014) 1–9.
- [91] A. Fouladitajar, F. Z. Ashtiani, A. Okhovat, B. Dabir, Membrane fouling in microfiltration of oil-in-water emulsions; a comparison between constant pressure blocking laws and genetic programming (GP) model, *Desalination* 329 (2013) 41–49.

- [92] J. D. Schiffman, M. A. Kiechel, A. E. Donius, U. G. Wegst, C. L. Schauer, Crosslinked poly(allylamine) fibers electrospun from basic and acidic solutions, *J. Mater. Sci.* 48 (22) (2013) 7856-7862.
- [93] U. Zulfikar, S. Z. Hussain, M. Awais, M. M. J. Khan, I. Hussain, S. W. Husain, T. Subhani, In-situ synthesis of bi-modal hydrophobic silica nanoparticles for oil-water separation, *Colloids Surfaces A: Physicochem. Eng. Aspects* 508 (2016) 301–308.
- [94] X. Hu, Y. Yu, J. Zhou, Y. Wang, J. Liang, X. Zhang, Q. Chang, L. Song, The improved oil/water separation performance of grapheme oxide modified Al<sub>2</sub>O<sub>3</sub> microfiltration membrane, *J. Membr. Sci.* 476 (2015) 200–204.
- [95] D. Emadzadeh, W.J. Lau, T. Matsuura, M. Rahbari-Sisakht, A.F. Ismail, A novel thin film composite forward osmosis membrane prepared from PSf–TiO<sub>2</sub> nanocomposite substrate for water desalination, *Chem. Eng. J.* 237 (2014) 70-80.
- [96] J.-F. Li, Z-L. Xu, H. Yang, L-Y. Yu, M. Liu, Effect of TiO<sub>2</sub> nanoparticles on the surface morphology and performance of microporous PES membrane, *Appl. Surf. Sci.* 255 (2009) 4725-4732.
- [97] C. Liao, J. Zhao, P. Yu, H. Tong, Y. Luo, Synthesis and characterization of low content of different SiO<sub>2</sub> materials composite poly (vinylidene fluoride) ultrafiltration membranes, *Desalination* 285 (2012) 117–122.
- [98] H. Li, W. Shi, Y. Zhang, R. Zhou, H. Zhang, Preparation of hydrophilic PVDF/PPTA blend membranes by in situ polycondensation and its application in the treatment of landfill leachate, *Appl. Surf. Sci.* 346 (2015) 134–146.
- [99] J. Yin, J. Zhou, Novel polyethersulfone hybrid ultrafiltration membrane prepared with SiO<sub>2</sub>-g-(PDMAEMA-co-PDMAPS) and its antifouling performances in oil-in-water emulsion application, *Desalination* 365 (2015) 46-56.
- [100] J. Ju, C. Wang, T. Wang, Q. Wang, Preparation and characterization of pH-sensitive and antifouling poly(vinylidene fluoride) microfiltration membranes blended with poly(methyl methacrylate-2-hydroxyethyl methacrylate-acrylic acid), *J. Colloid Interf. Sci.* 434 (2014) 175-180.
- [101] C. Zhao, X. Xu, J. Chen, F. Yang, Optimization of preparation conditions of poly(vinylidene fluoride)/graphene oxide microfiltration membranes by the Taguchi experimental design, *Desalination* 334 (2014) 17–22.

- [102] T. Rajasekhar, M. Trinadh, P. V. Babu, A. V. S. Sainath, A.V.R. Reddy, Oil–water emulsion separation using ultrafiltration membranes based on novel blends of poly(vinylidene fluoride) and amphiphilic tri-block copolymer containing carboxylic acid functional group, *J. Membr. Sci.* 481 (2015) 82–93.
- [103] B. Deng, M. Yu, X. Yang, B. Zhang, L. Li, L. Xie, J. Li, X. Lu, Antifouling microfiltration membranes prepared from acrylic acid or methacrylic acid grafted poly(vinylidene fluoride) powder synthesized via pre-irradiation induced graft polymerization, *J. Membr. Sci.* 350 (2010) 252–258.
- [104] L. Huang, N.-N. Bui, S. S. Manickam, J. R. McCutcheon, Controlling electrospun nanofiber morphology and mechanical properties using humidity, *J. Polym. Sci. Part B: Polym. Phys.* 49 (24) (2011) 1734-1744.
- [105] R. Nirmala, K.T. Nam, S.J. Park, Y.S. Shin, R. Navamathavan, H.Y. Kim, Formation of high aspect ratio polyamide-6 nanofibers via electrically induced double layer during electrospinning, *Appl. Surf. Sci.* 256 (2010) 6318–6323.
- [106] Q. Shi, N. Vitchuli, L. Ji, J. Nowak, M. McCord, M. Bourham, X. Zhang, A Facile Approach to Fabricate Porous Nylon 6 Nanofibers Using Silica Nanotemplate, *J. Appl. Polym. Sci.* 120 (2011) 425–433.
- [107] X. Fan, Y. Su, X. Zhao, Y. Li, R. Zhang, J. Zhao, Z. Jiang, J. Zhu, Y. Ma, Y. Liu, Fabrication of polyvinyl chloride ultrafiltration membranes with stable antifouling property by exploring the pore formation and surface modification capabilities of polyvinyl formal, *J. Membr. Sci.* 464 (2014)100–109.
- [108] T. M. Ting, M. M. Nasef, K. Hashim, Modification of nylon-6 fibres by radiation-induced graft polymerisation of vinylbenzyl chloride, *Radia. Phys. Chem.* 109 (2015) 54-62.
- [109] A. M. Pinto, J. Martins, J. A. Moreira, A. M. Mendes, F. D. Magalhaes, Dispersion of graphene nanoplatelets in poly(vinyl acetate) latex and effect on adhesive bond strength, *Polym. Int.* 62 (2013) 928–935.
- [110] S. Liang, Y. Kang, A. Tiraferri, E. P. Giannelis, X. Huang, M. Elimelech, Highly Hydrophilic Polyvinylidene Fluoride (PVDF) Ultrafiltration Membranes via Post fabrication Grafting of Surface-Tailored Silica Nanoparticles, *ACS Appl. Mater. Interf.* 5 (2013) 6694-6703.

- [111] R. V. Kumar, A. K. Ghoshal, G. Pugazhenti, Elaboration of novel tubular ceramic membrane from inexpensive raw materials by extrusion method and its performance in microfiltration of synthetic oily wastewater treatment, *J. Membr. Sci.* 490 (2015) 92-102.
- [112] P.-F. Ren, Y. Fang, L.-S. Wan, X.-Y. Ye, Z.-K. Xu, Surface modification of polypropylene microfiltration membrane by grafting poly(sulfobetaine methacrylate) and poly(ethylene glycol): Oxidative stability and antifouling capability, *J. Membr. Sci.* 492 (2015) 249–256.
- [113] M.-X. Hua, J.-N. Li, S.-L. Zhang, L. Li, Z.-K. Xu, Hydrophilic modification of PVDF microfiltration membranes by adsorption of facial amphiphile cholic acid, *Colloids Surf. B: Biointerfa.* 123 (2014) 809–813.
- [114] T. G. Vladkova, P. Dineff, R. Stojcheva, B. Tomerova, Ion-plasma modification of polyvinylchloride microfiltration membranes, *J. Appl. Polym. Sci.* 90 (2003) 2433–2440.
- [114] J. Han, S. Meng, Y. Dong, J. Hu, W. Gao, Capturing hormones and bisphenol A from water via sustained hydrogen bond driven sorption in polyamide microfiltration membranes, *Wat. Res.* 47 (2013) 197-208.
- [116] W. Guo, H.-H. Ngo, J. Li, A mini-review on membrane fouling, *Bioresour. Technol.* 122 (2012) 27–34.
- [117] C. Boyer, B. Clark, V. Jochen, R. L. C. K. Shale gas: A global resource, 23 (3) (2011) 28–39.
- [118] U. S. Energy Information Administration, Annual Energy Outlook, Washington, DC (2012).
- [119] U. S. Energy Information Administration, International Energy Outlook (2017).
- [120] U. S. Energy Information Administration, Annual Energy Outlook (2017).
- [121] I. C. Scotchman, Shale gas and fracking: exploration for unconventional hydrocarbons, *Proceedings of the Geologists' Association*, Accepted 1 Sep 2016.
- [122] A. Achilli, T. Y. Cath, A. E. Childress, Power generation with pressure-retarded osmosis: an experimental and theoretical investigation, *J. Membr. Sci.* 343 (2009) 42-52.
- [123] Y. C. Kim, M. Elimelech, Potential of osmotic power generation by pressure retarded osmosis using seawater as feed solution: analysis and experiments, *J. Membr. Sci.* 429 (2013) 330-337.

- [124] T. Y. Cath, M. Elimelech, J. R. McCutcheon, R. L. McGinnis, A. Achilli, D. Anastasio, A. R. Brady, A. E. Childress, I. V. Farr, N. T. Hancock, J. Lampi, L. D. Nghiem, M. Xie, N. Y. Yip, Standard Methodology for Evaluating Membrane Performance in Osmotically Driven Membrane Processes, *Desalination* 312 (2013) 31–38.
- [125] D. L. Shaffer, J. R. Werber, H. Jaramillo, S. Lin, M. Elimelech, Forward osmosis: Where are we now?, *Desalination* 356 (2015) 271-284.
- [126] W.A. Phillip, J. S. Yong, M. Elimelech, Reverse draw solute permeation in forward osmosis: modeling and experiments, *Environ. Sci. Technol.* 44 (2010) 5170–5176.
- [127] C.Y. Tang, Q. She, W.C.L. Lay, R. Wang, A.G. Fane, Coupled effects of internal concentration polarization and fouling on flux behavior of forward osmosis membranes during humic acid filtration, *J. Membr. Sci.* 354 (2010) 123–133.
- [128] A. Tiraferri, N.Y. Yip, A.P. Straub, S. Romero-Vargas Castrillon, M. Elimelech, A method for the simultaneous determination of transport and structural parameters of forward osmosis membranes, *J. Membr. Sci.* 444 (2013) 523–538.
- [129] R. L. McGinnis, J. R. McCutcheon, M. Elimelech, A novel ammonia–carbon dioxide osmotic engine for power generation, *J. Membr. Sci.* 305 (2007)13–19.
- [130] K. L. Hickenbottom, J. Vanneste, T. Y. Cath, Assessment of alternative draw solutions for optimized performance of a closed-loop osmotic heat engine, *J. Membr. Sci.* 504 (2016) 162–175.
- [131] Q. Ge, M. Ling, T.-S. Chung, Draw solutions for forward osmosis processes: Developments, challenges, and prospects for the future, *J. Membr. Sci.* 442 (2013) 225–237.
- [132] A. Achilli, T. Y. Cath, A. E. Childress, Selection of inorganic-based draw solutions for forward osmosis applications, *J. Membr. Sci.* 364 (2010) 233–241.
- [133] M. L. Stone, A. D. Wilson, M. K. Harrup, F. F. Stewart, An initial study of hexavalent phosphazene salts as draw solutes in forward osmosis, *Desalination* 312 (2013) 130–136.
- [134] S. K. Yen, F. M. Haja N., M. Su, K. Y. Wang, T.-S. Chung, Study of draw solutes using 2-methylimidazole-based compounds in forward osmosis, *J. Membr. Sci.* 364 (2010) 242–252.
- [135] K. S. Bowden, A. Achilli, A. E. Childress, Organic ionic salt draw solutions for osmotic membrane bioreactors, *Bioreso. Technol.* 122 (2012) 207–216.

- [136] B. Corzo, T. Torre, C. Sans, E. Ferrero, J. J. Malfeito, Evaluation of draw solutions and commercially available forward osmosis membrane modules for wastewater reclamation at pilot scale, *Chem. Eng. J.* 326 (2017) 1–8.
- [137] G. Han, Q. Ge, T.-S. Chung, Conceptual demonstration of novel closed-loop pressure retarded osmosis process for sustainable osmotic energy generation, *Appl. Energy* 132 (2014) 383–393.
- [138] D. Emadzadeh, W. J. Lau, T. Matsuura, M. Rahbari-Sisakht, A. F. Ismail, A novel thin film composite forward osmosis membrane prepared from PSf–TiO<sub>2</sub> nanocomposite substrate for water desalination, *Chem. Eng. J.* 237 (2014) 70–80.
- [139] L. Shen, S. Xiong, Y. Wang, Graphene oxide incorporated thin-film composite membranes for forward osmosis applications, *Chem. Eng. Sci.* 143 (2016) 194–205.
- [140] X. Li, T.-S. Chung, Thin-film composite P84 co-polyimide hollow fiber membranes for osmotic power generation, *Appl. Energy* 114 (2014) 600–610.
- [141] G. D. Mehta, S. Loeb, Internal polarization in the porous substructure of a semipermeable membrane under pressure-retarded osmosis, *J. Membr. Sci.* 4 (1978) 261–265.
- [142] S. Loeb, L. Titelman, E. Korngold, J. Freiman, Effect of porous support fabric on osmosis through a Loeb-Sourirajan type asymmetric membrane, *J. Membr. Sci.* 129 (1997) 243–249.
- [143] S.-F. Pan, Y. Dong, Y.-M. Zheng, L.-B. Zhong, Z.-H. Yuan, Self-sustained hydrophilic nanofiber thin film composite forward osmosis membranes: Preparation, characterization and application for simulated antibiotic wastewater treatment, *J. Membr. Sci.* 523 (2017) 205–215.
- [144] M. Hamdan, A. O. Sharif, G. Derwish, S. Al-Aibi, A. Altaee, Draw solutions for Forward Osmosis process: Osmotic pressure of binary and ternary aqueous solutions of magnesium chloride, sodium chloride, sucrose and maltose, *J. Food Eng.* 155 (2015) 10–15.
- [145] V. T. Granik, B. Smith, S. C. Lee, M. Ferrari, Osmotic pressures of binary solutions of non-electrolytes, *Biomed. Microdevices* 4 (2002) 309–321.
- [146] K. S. Pitzer, *Thermodynamics*, McGraw-Hill Inc., New York 1995.
- [147] M. J. Blandamer, J. B. Engberts, P. T. Gleeson, J. C. Reis, Activity of water in aqueous systems; A frequently neglected property, *Chem. Soc. Rev.* 34 (2005) 440–458.
- [148] M. Qasim, F. Mohammed, A. Aidan, N. A. Darwish, Forward osmosis desalination using ferric sulfate draw solute, *Desalination* 423 (2017) 12–20.

- [149] K. L. Hickenbottom, N. T. Hancock, N. R. Hutchings, E. W. Appleton, E. G. Beaudry, P. Xu, T. Y. Cath, Forward osmosis treatment of drilling mud and fracturing wastewater from oil and gas operations, *Desalination* 312 (2013) 60–66.
- [150] C. Boo, Y. F. Khalil, M. Elimelech, Performance evaluation of trimethylamine–carbon dioxide thermolytic draw solution for engineered osmosis, *J. Membr. Sci.* 473 (2015) 302–309.
- [151] M. Xie, W. E. Price, L. D. Nghiem, M. Elimelech, Effects of feed and draw solution temperature and transmembrane temperature difference on the rejection of trace organic contaminants by forward osmosis, *J. Membr. Sci.* 438 (2013) 57–64.
- [152] G. H. Coleman, A. M. Alvarado, Acetamide, *Org. Synth.* 3 (1923) 3.
- [153] M. Lorin, Preparation of formamide by means of formiates and oxalates. *Chem. News J. Phy. Sci.* IX (1864) 291.
- [154] B. D. Coday, N. Almaraz, T. Y. Cath, Forward osmosis desalination of oil and gas wastewater: Impacts of membrane selection and operating conditions on process performance, *J. Membr. Sci.* 488 (2015) 40–55.
- [155] E. A. Bell, T. E. Poynor, K. B. Newhart, J. Regnery, B. D. Coday, T. Y. Cath, Produced water treatment using forward osmosis membranes: Evaluation of extended-time performance and fouling, *J. Membr. Sci.* 525 (2017) 77–88.
- [156] S. Lee, Y. C. Kim, Calcium carbonate scaling by reverse draw solute diffusion in a forward osmosis membrane for shale gas wastewater treatment, *J. Membr. Sci.* 522 (2017) 257–266.
- [157] M. Bystrianský, O. Nir, M. Šír, Z. Honzajková, R. Vurm, P. Hrychová, A. Bervic, B. Bruggen, The presence of ferric iron promotes calcium sulphate scaling in reverse osmosis processes, *Desalination* 393 (2016) 115–119.
- [158] T.Y. Cath, A.E. Childress, M. Elimelech, Forward osmosis: principles, applications, and recent developments, *J. Membr. Sci.* 281 (2006) 70–87.
- [159] S. Zhao, L. Zou, C.Y. Tang, D. Mulcahy, Recent developments in forward osmosis: opportunities and challenges, *J. Membr. Sci.* 396 (2012) 1–21.
- [160] K. Lutcmiah, A.R.D. Verliefde, K. Roest, L.C. Rietveld, E.R. Cornelissen, Forward osmosis for application in wastewater treatment: a review, *Water Res.* 58(2014) 179–197.

- [161] T.S. Chung, X. Li, R.C. Ong, Q. Ge, H. Wang, G. Han, Emerging forward osmosis (FO) technologies and challenges ahead for clean water and clean energy applications, *Curr. Opin. Chem. Eng.* 1 (2012) 246–257.
- [162] K.Y. Wang, T.S. Chung, G. Amy, Developing thin-film-composite forward osmosis membranes on the PES/SPSf substrate through interfacial polymerization, *AIChE J.* 58 (2012) 770–781.
- [163] I. Pinnau, B.D. Freeman, Formation and modification of polymeric membranes: overview, in: I. Pinnau, B.D. Freeman (Eds.), *Membrane Formation and Modification*, American Chemical Society, Washington, DC, 1999, pp. 1–22.
- [164] J.T. Arena, B. McCloskey, B.D. Freeman, J.R. McCutcheon, Surface modification of thin film composite membrane support layers with polydopamine: enabling use of reverse osmosis membranes in pressure retarded osmosis, *J. Membr. Sci.* 375 (2011) 55–62.
- [165] C.H. Tan, H.Y. Ng, A novel hybrid forward osmosis – nanofiltration (FO–NF) process for seawater desalination: draw solution selection and system configuration, *Desalin. Water Treat.* 13 (2010) 356–361.
- [166] N. Y. Yip, A. Tiraferri, W. A. Phillip, J. D. Schiffman, M. Elimelech, High performance thin-film composite forward osmosis membrane, *Environ. Sci. Technol.* 44 (2010) 3812–3818.
- [167] J. Ren, J.R. McCutcheon, A new commercial thin film composite membrane for forward osmosis, *Desalination* 343 (2014) 187–193.
- [168] J. Ren, B. O'Grady, G. deJesus, J. R. McCutcheon, Sulfonated polysulfone supported high performance thin film composite membranes for forward osmosis, *Polymer* 103 (2016) 486–497.
- [169] W.J. Lau, A.F. Ismail, N. Misdan, M.A. Kassim, A recent progress in thin film composite membrane: a review, *Desalination* 287 (2012) 190–199.
- [170] B. Khorshidi, T. Thundat, B. Fleck, M. Sadrzadeh, Thin film composite polyamide membranes: parametric study on the influence of synthesis conditions, *RSC Adv.* 5 (2015) 54985–54997.
- [171] R.J. Petersen, Composite reverse osmosis and nanofiltration membranes, *J. Membr. Sci.* 83 (1993) 81–150.

- [172] M. Sadrzadeh, S. Bhattacharjee, Rational design of phase inversion membranes by tailoring thermodynamics and kinetics of casting solution using polymer additives, *J. Membr. Sci.* 441 (2013) 31–44.
- [173] L. Huang, J. R. McCutcheon, Hydrophilic nylon 6,6 nanofibers supported thin film composite membranes for engineered osmosis, *J. Membr. Sci.* 457 (2014)162–169.
- [174] J. Wei, C. Qiu, C.Y. Tang, R. Wang, A.G. Fane, Synthesis and characterization of flat-sheet thin film composite forward osmosis membranes, *J. Membr. Sci.* 372 (2011) 292–302.
- [175] D. Rana, T. Matsuura, Surface modifications for antifouling membranes, *Chem. Rev.* 110 (2010) 2448–2471.
- [176] S. Xiong, J. Zuo, Y. G. Ma, L. Liu, H. Wu, Y. Wang, Novel thin film composite forward osmosis membrane of enhanced water flux and anti-fouling property with N-[3-(trimethoxysilyl) propyl] ethylenediamine incorporated, *J. Membr. Sci.* 520 (2016) 400–414.
- [177] N. M. Mazlan, P. Marchetti, H.A. Maples, B. Gu, S. Karan, A. Bismarck, A. G. Livingston, Organic fouling behaviour of structurally and chemically different forward osmosis membranes – A study of cellulose triacetate and thin film composite membranes, *J. Membr. Sci.* 520 (2016) 247–261.
- [178] M. S. Islam, J. R. McCutcheon, M. S. Rahaman, A high flux polyvinyl acetate-coated electrospun nylon 6/SiO<sub>2</sub> composite microfiltration membrane for the separation of oil-in-water emulsion with improved antifouling performance, *J. Membr. Sci.* 537 (2017) 297–309.
- [179] G-B. Yin, Analysis of Electrospun Nylon 6 Nanofibrous Membrane as Filters, *J. Fiber Bioeng. Informat.*, 3 (2010) 137-141.
- [180] J. W. Krumpfer, T. Schuster, M. Klapper, K. Müllen, Make it nano – keep it nano, *Nano Today* 8 (2013) 417–438.
- [181] M. M. Pendergast, E.M.V. Hoek, A review of water treatment membrane nanotechnologies, *Energy Environ. Sci.* 4 (2011) 1946–1971.
- [182] T. D. Naylor, *Polymer Membranes- Materials, Structures and Separation Performance*; Dolbey, R. T. L., Ed.; Rapra Technology Limited: Billingham, UK, 1996.
- [183] R. J. Peterson, J. E. Cadotte, Thin Film Composite Reverse Osmosis Membrane. In *Handbook of Industrial Membrane Technology*, Porter, M.C., Ed.; Noyes Publications: Westwood, NJ, 1990.

- [184] N.-N. Bui, J. R. McCutcheon, Nanofiber Supported Thin-Film Composite Membrane for Pressure-Retarded Osmosis, *Environ. Sci. Technol.* 48 (2014) 4129–4136.
- [185] B. Khorshidi, A. Bhinder, T. Thundat, D. Pernitsky, M. Sadrzadeh, Developing high throughput thin film composite polyamide membranes for forward osmosis treatment of SAGD produced water, *J. Membr. Sci.* 511 (2016) 29–39.
- [186] A. Tiraferri, N.Y. Yip, W. a Phillip, J.D. Schiffman, M. Elimelech, Relating performance of thin-film composite forward osmosis membranes to support layer formation and structure, *J. Membr. Sci.* 367 (2011) 340–352.
- [187] N. Widjojo, T.S. Chung, M. Weber, C. Maletzko, V. Warzelhan, The role of sulphonated polymer and macrovoid-free structure in the support layer for thin-film composite (TFC) forward osmosis (FO) membranes, *J. Membr. Sci.* 383 (2011) 214–223.
- [188] X. Song, Z. Liu, D. D. Sun, Nano gives the answer: breaking the bottleneck of internal concentration polarization with a nanofiber composite forward osmosis membrane for a high water production rate, *Adv. Mater.* 23 (2011) 3256–3260.
- [189] X. Li, K.Y. Wang, B. Helmer, T.S. Chung, Thin-film composite membranes and formation mechanism of thin-film layers on hydrophilic cellulose acetate propionate substrates for forward osmosis processes, *Ind. Eng. Chem. Res.* 51(2012) 10039–10050.
- [190] G. Han, T.S. Chung, M. Toriida, S. Tamai, Thin-film composite forward osmosis membranes with novel hydrophilic supports for desalination, *J. Membr. Sci.* 423–424 (2012) 543–555.
- [191] M. Tian, C. Qiu, Y. Liao, S. Chou, R. Wang, Preparation of polyamide thin film composite forward osmosis membranes using electrospun polyvinylidene fluoride (PVDF) nanofibers as substrates, *Sep. Purif. Technol.* 118 (2013) 727–736.
- [192] M. Yasukawa, S. Mishima, M. Shibuya, D. Saeki, T. Takahashi, T. Miyoshi, T. Miyoshi, H. Matsuyama, Preparation of a forward osmosis membrane using a highly porous polyketone microfiltration membrane as a novel support, *J. Membr. Sci.* 487 (2015) 51–59.
- [193] N. Ma, J. Wei, R. Liao, C.Y. Tang, Zeolite-polyamide thin film nanocomposite membranes: towards enhanced performance for forward osmosis, *J. Membr. Sci.* 405–406 (2012) 149–157.
- [194] L. Huang, J. T. Arena, J.R. McCutcheon, Surface modified PVDF nanofiber supported thin film composite membranes for forward osmosis, *J. Membr. Sci.* 499 (2016) 352–360.

- [195] P. Lu, S. Liang, L. Qiu, Y. Gao, Q. Wang, Thin film nanocomposite forward osmosis membranes based on layered double hydroxide nanoparticles blended substrates, *J. Membr. Sci.* 504 (2015) 196–205.
- [196] C.S. Ong, P.S. Goh, W.J. Lau, N. Misdan, A.F. Ismail, Nanomaterials for biofouling and scaling mitigation of thin film composite membrane: A review, *Desalination* 393 (2016) 2–15.
- [197] Y. Yang, Q. Liu, H. Wang, F. Ding, G. Jin, C. Li, H. Meng, Superhydrophobic modification of ceramic membranes for vacuum membrane distillation, *Chinese J. Chem. Eng.* 25 (2017) 1395–1401.
- [198] W. Cao, I.M. Mujtaba, Simulation of vacuum membrane distillation process for desalination with Aspen Plus, *Ind. Eng. Chem. Res.* 54 (2) (2015) 672–680.
- [199] Le Han, Tong Xiao, Yong Zen Tan, Anthony G. Fane, Jia Wei Chew, Contaminant rejection in the presence of humic acid by membrane distillation for surface water treatment, *J. Membr. Sci.* 541 (2017) 291–299.
- [200] Olivier Lefebvre, Rene' Moletta, Treatment of organic pollution in industrial saline wastewater: A literature review, *Water Research* 40 (2006) 3671– 3682.
- [201] K. J. Sylus, H. Ramesh, The Study of Sea Water Intrusion in Coastal Aquifer by Electrical Conductivity and Total Dissolved Solid Method in Gurpur and Netravathi River Basin, *Aquatic Procedia* 4 ( 2015 ) 57 – 64.
- [202] S. K. Sharma, Influence of Sea water ingress: a case study from east coast aquifer in India, 20th salt water intrusion meeting, 2008.
- [203] P. Lord, M. Weston, L. K. Fontenelle, J. Haggstrom, Recycling Water: Case Studies in Designing Fracturing Fluids Using Flowback, Produced, and Nontraditional Water Sources. Presented at the SPE Latin-American and Caribbean Health, Safety, Environment and Social Responsibility Conference, Lima, Peru, 26-27 June, 2013, SPE-165641-MS.
- [204] J. Pelipenko, J. Kristl, B. Jankovic, S. Baumgartner, P. Kocbek, The impact of relative humidity during electrospinning on the morphology and mechanical properties of nanofibers, *Internat. J. Pharmaceut.* 456 (2013) 125-134.

## Appendices

Appendices include supporting data and information for Chapters 3, 4, 5 and 6. Each of the aforementioned Chapters has a separate appendix section titled as Appendix A, B, C and D corresponding to Chapter 3, 4, 5 and 6, respectively.

### Appendix A

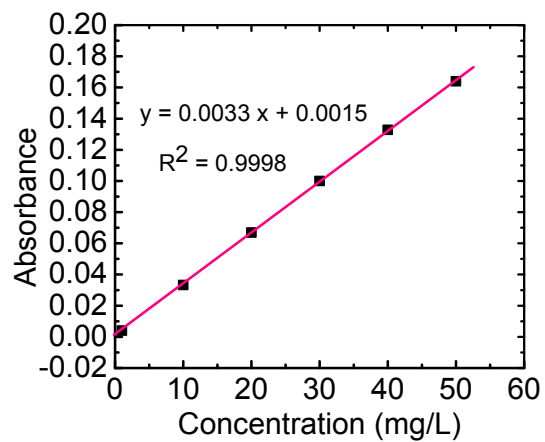


Figure A-1. UV-calibration curve for oil content determination in O/W emulsions.

Table A-1. Oil content determination (at different applied pressures) in O/W emulsions separated by PVAc-coated N6/SiO<sub>2</sub> (20 wt.%) membrane using UV-calibration curve.

Applied pressure (psi)	Before filtration	After filtration		Oil rejection (%)
	Oil conc. (mg/L)	Absorbance	Oil conc. (mg/L)	
4	250	0.0114	3.00	98.80
	500	0.0180	5.00	99.00
	1000	0.0279	8.00	99.20
8	250	0.0197	5.50	97.80
	500	0.0230	6.50	98.70
	1000	0.0345	10.00	99.00
12	250	0.0362	10.50	95.80
	500	0.0287	8.25	98.35
	1000	0.0385	11.20	98.88
16	250	0.0444	13.00	94.80
	500	0.0312	9.00	98.20
	1000	0.0444	13.00	98.70
20	250	0.0568	16.75	93.30
	500	0.0320	9.25	98.15
	1000	0.0510	15.00	98.50

Table A-2. Oil content determination (at different applied pressures) in O/W emulsions separated by commercial PSf membrane using UV-calibration curve.

Applied pressure (psi)	Before filtration	After filtration		Oil rejection (%)
	Oil conc. (mg/L)	Absorbance	Oil conc. (mg/L)	
4	250	0.0176	4.88	98.05
	500	0.0197	5.50	98.90
	1000	0.0312	9.00	99.10
8	250	0.0281	8.05	96.78
	500	0.0246	7.00	98.60
	1000	0.0378	11.00	98.90
12	250	0.0363	10.55	95.78
	500	0.0263	7.50	98.50
	1000	0.0385	11.20	98.88
16	250	0.0477	14.00	94.40
	500	0.0329	9.50	98.10
	1000	0.0477	14.00	98.60
20	250	0.0609	18.00	92.80
	500	0.0345	10.00	98.00
	1000	0.0510	15.00	98.50

Table A-3. Oil content determination (at different applied pressures) in O/W emulsions separated by commercial PVDF membrane using UV-calibration curve.

Applied pressure (psi)	Before filtration	After filtration		Oil rejection (%)
	Oil conc. (mg/L)	Absorbance	Oil conc. (mg/L)	
4	250	0.0370	10.75	95.70
	500	0.0200	5.60	98.88
	1000	0.0345	10.00	99.00
8	250	0.0485	14.25	94.30
	500	0.0256	7.30	98.54
	1000	0.0401	11.70	98.83
12	250	0.0577	17.03	93.19
	500	0.0263	7.50	98.50
	1000	0.0418	12.20	98.78
16	250	0.0740	21.98	91.21
	500	0.0345	10.00	98.00
	1000	0.0497	14.60	98.54
20	250	0.0827	24.60	90.16
	500	0.0350	10.15	97.97
	1000	0.0560	16.50	98.35

### Effect of RH on electrospun N6 nanofibers

Figure A-2 shows the FE-SEM images of electrospun N6 nanofibers as a function of RH (30, 40, 50 and 60%). The RH has a significant effect on diameter and shape of nanofibers during electrospinning of polymeric solutions [204]. In fact, the viscosity of solution and how fast the solvent evaporates upon the formation of the fiber can be changed by changing the relative humidity. The larger diameter of nanofibers was obtained at 30% RH because the solution viscosity was higher at this RH (30%) (Figure A-2 A). Higher viscosity of the solution was responsible to obtain the nanofibers with higher diameter [105]. Compared to the nanofibers at 30% RH, relatively lower diameter nanofibers (80-160 nm) were obtained at the relative humidity of 40% (Figure A-2 B). The nanofiber diameters were decreasing more consecutively with bead formation at the relative humidity of 50% and 60% (Figure A-2 C and Figure A-2 D). At the higher relative humidity, the solution viscosity became lower and it was also difficult to evaporate the solvent to form fiber when the liquid jets moved from the nozzle tip to collector during electrospinning. Therefore, 40% of relative humidity was the optimum condition for N6 solution to produce the best electrospun nanofibers (Figure A-2 B).

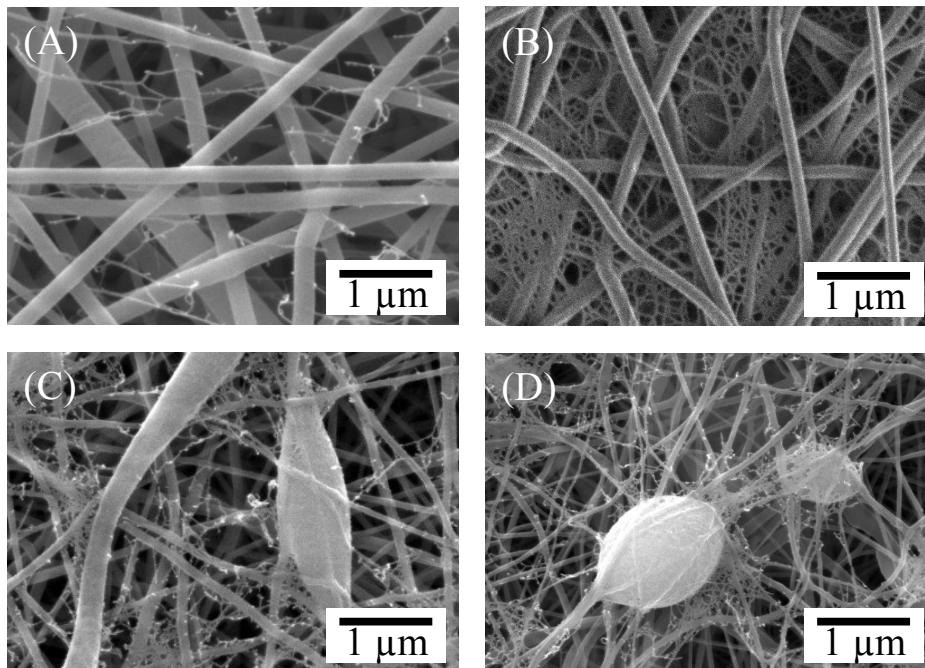


Figure A-2. FE-SEM images of electrospun pristine N6 nanofibers at the relative humidity of (A) 30%, (B) 40%, (C) 50%, and (D) 60%.

Dynamic water contact angle of the E.Spun N6 nanofiber mat

The volume changing method using the VCA optima instrument (AST Products, Inc.) was used to investigate the dynamic water contact angle of the E.Spun N6 nanofiber mat. First, a small water droplet was formed and placed on the surface of the nanofiber mat. The needle was then brought near the surface and the volume of the droplet was gradually increased while simultaneously recording. This provided a measurement of the advancing water contact angle. The receding water contact angle was measured the same way however the volume of the water droplet was gradually decreased this time.

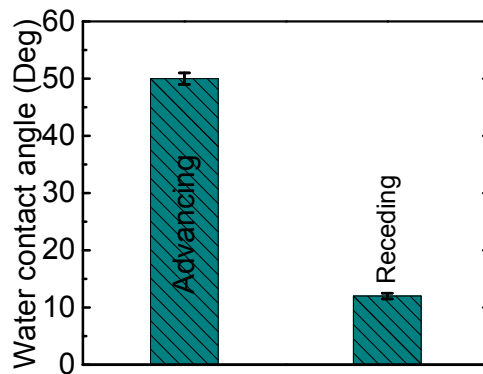


Figure A-3. Dynamic water contact angle of the E. Spun N6 nanofiber mat while advancing and receding.

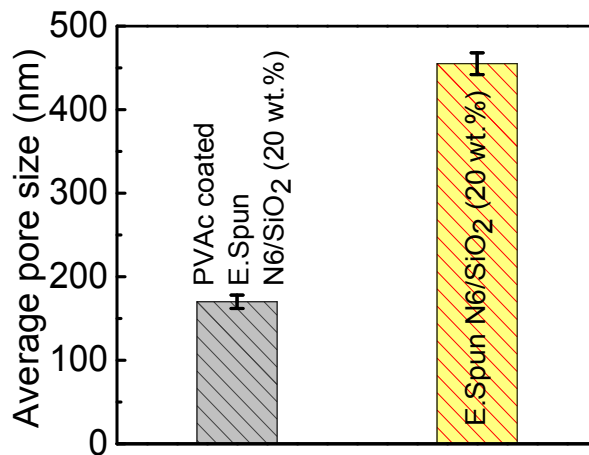


Figure A-4. Average pore sizes of the electrospun N6/SiO<sub>2</sub> (20 wt.%) composite nanofiber mat and PVAc-coated electrospun N6/SiO<sub>2</sub> (20 wt.%) composite membrane.

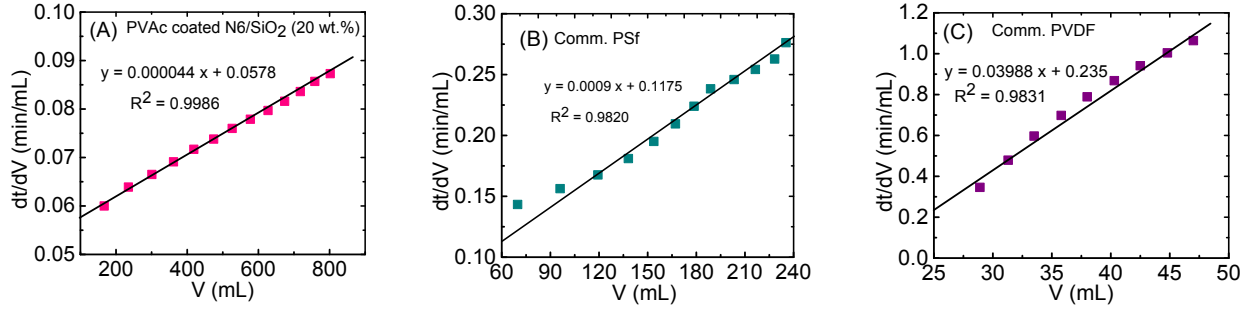


Figure A-5. The dt/dV versus V filtration curves of the (A) fabricated membrane, (B) commercial PSf membrane and (C) commercial PVDF membrane for microfiltration of O/W emulsion.

Table A-4. Antifouling test results

Membrane	Pure water flux (LMH) at 0.28 bar		Flux recovery, FR (%)
	Before fouling	After fouling	
Fabricated	1348	1146	85
Comm. PSf	764	565	74
Comm. PVDF	284	65	23

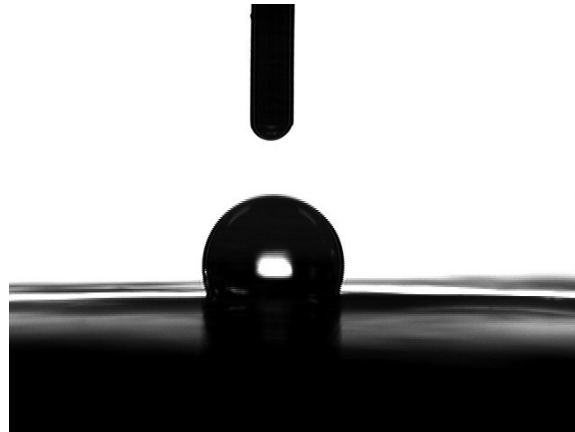


Figure A-6. Oil contact angle under water of the fabricated MF membrane.

Appendix B

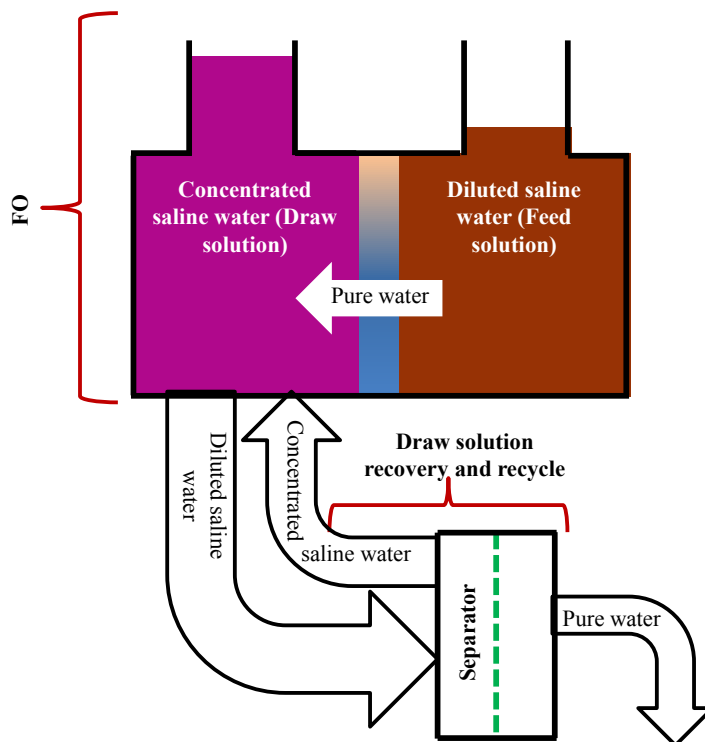


Figure B-1. A schematic representation of FO process.

Table B-1. Properties of  $\text{NH}_4\text{HCO}_3$  draw solution at a temperature of 24 °C.

Draw solution	D ( $\times 10^{-9} \text{ m}^2/\text{s}$ )	Solubility (g/L)	Conc. (M) at solubility	Osmotic pressure (MPa) at solubility
$\text{NH}_4\text{HCO}_3$	1.42	220	2.78	11.50

Table B-2. A list of the distillable organic draw solutes with osmolality and osmotic pressure.

Draw solute	Conc. (M)	Pristine		Residue	
		Osmolality (osm/kg)	Osmotic pressure (MPa)	Osmolality (osm/kg)	Osmotic pressure (MPa)
KAc	0.66	2.266	2.80	2.266	2.80
KF	0.68	2.266	2.80	2.258	2.79
NaGly	0.73	2.266	2.80	2.266	2.80
NaP	0.69	2.266	2.80	2.258	2.79

## Appendix C

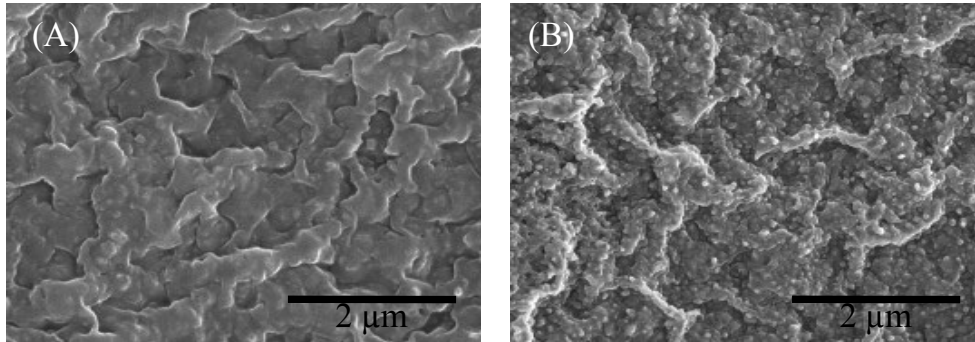


Figure C-1. FE-SEM images of the top surface of electrospun N6 supported TFC membranes with PA/SiO<sub>2</sub> composite active layer with SiO<sub>2</sub> concentrations of (A) 0% and (B) 4%.

## Appendix D

Table D-1. Results from flux recovery test.

Wastewater	MF membrane	Pure water flux (LMH) at 0.28 bar		FR (%)
		Before filtration of fracking wastewater	After filtration of fracking wastewater	
Fracking wastewater	Nanocomposite	1348	1200	89
	PSf	764	581	76

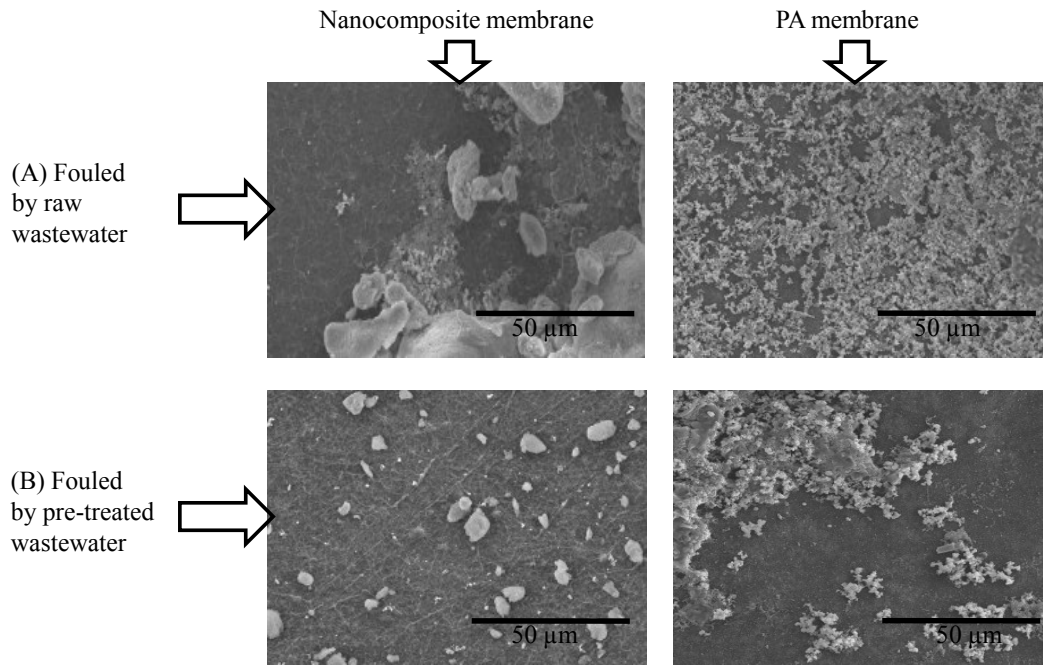


Figure D-1. FE-SEM images of fouled FO membranes (nanocomposite and PA) when (A) raw and (B) pre-treated fracking wastewaters were employed as feed solution, while NaCl was used as draw solution.

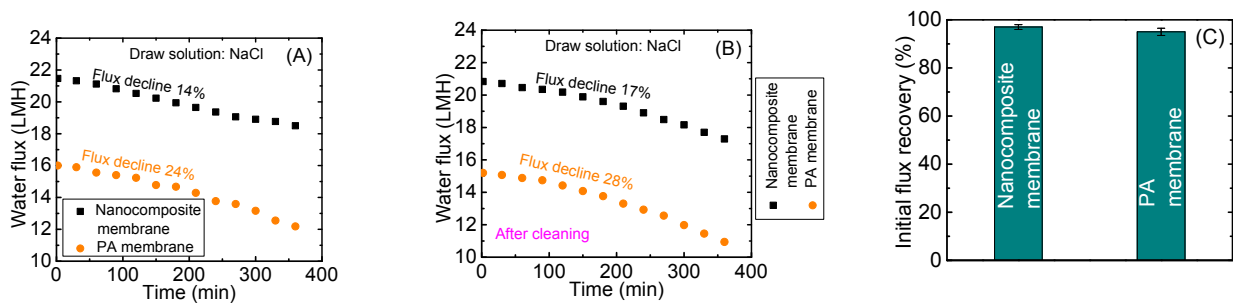


Figure D-2. (A) Decline of water flux for the pristine membrane when pre-treated fracking wastewater was used as feed and 4.0 M NaCl was used as draw solution, (B) Decline of water flux after cleaning of the membrane fouled by the pre-treated fracking wastewater (Feed: Pre-treated fracking wastewater, Draw solution: 4.0 M NaCl), and (C) Initial FO water flux recovery after cleaning of the membrane fouled by the pre-treated fracking wastewater. [Each set of experiments was conducted three times and the average values of the data obtained from these experiments are reported in Figure D-2 A and Figure D-2 B].